
# Master Thesis

## Multiple-bands structures in the $^{223}_{90}$Th133 nucleus. Quadrupole-Octupole collectivity in the A$\sim$220 mass region of the nuclear map.

Author: Fitzgerald Ramírez Moreno
framirezmo@unal.edu.co

Advisor: Prof. Diego Alejandro Torres Galindo
datorresg@unal.edu.co

Master in Sciences Physics-Investigation
Program of Sciences Faculty
Universidad Nacional de Colombia

This work is being developed in collaboration with the
*Research in Nuclear Chemistry* group of Washington University in St. Louis, U.S.A.

http://www.gfnun.unal.edu.co/
June, 2018

*This work is Dedicated to God.*

*For by him were all things created, that are in heaven, and that are in earth, visible and invisible, whether they be thrones, or dominions, or principalities, or powers: all things were created by him, and for him:*

*And he is before all things, and by him all things consist.*

*Colossians 1:17.*

# Acknowledgements

*Thank you Father God for your provisions and wisdom and always meeting me at every point of my need.*

*I want to express my gratitude to my family, in particular to my parents, they have been held in my professional career.*

*Thanks to Professor Diego Torres for his enthusiasm, experience and knowledge. His effort and dedication have been important for making this work possible.*

*Thank the GFNUN. Their suggestions were very much appreciated.*

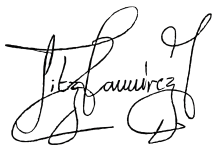

Fitzgerald Ramírez Moreno.

June 2018

# Contributions

Preliminary results of this work were presented in the following international scientific events:

- The *HI Accelerator Symposium, Canberra*, September 2015 by Walter Reviol (Washington University, St. Louis, USA).
- The *X Latin American Symposium on Nuclear Physics and Applications*, December 2015 by Fitzgerald Ramírez (Universidad Nacional de Colombia) Talk: Multiple octupole-type band structures in the 223-Th nucleus

As part of the training on nuclear reactions and analysis of $\gamma$ ray spectroscopy, along of the formation process of the Master program the following activities were developed:

1. One experiment performed in the Cyclotron at the Lawrence Berkeley National Laboratory, USA (2015) to measure lifetimes and nuclear magnetic moments of stable ($^{106}$Cd) and radioactive ($^{110}$Sn) isotopes. The experiment implied the understanding of $\gamma$ ray spectroscopy and coincidence technique.
2. Discussion and results about this training were presented in the following international events:

   (a) International Scientific Meeting on Nuclear Physics.
   *Magnetic Moment Measurements Using Alpha Transfer Reactions-Challenges and Perspectives*.
   Universidad de Andalucía, La Rábida, Spain.

   (b) II Andean School on Nuclear Physics.
   *The use of alpha transfer reactions to study g-factor of radioactive nuclei.*
   Universidad Nacional de Colombia - Sede Bogotá.

   (c) III Uniandes Particle Detector School.
   *Hyper-pure Germanium Detection System to Measure Nuclear Magnetic Moments.*
   Universidad de los Andes, Bogotá-Colombia

(d) Gordon Research Conference on Nuclear Chemistry: The Evolution of Nuclear Structure and Reaction Studies in the Era of Rare Isotope Beams
*Using the alpha-transfer reaction to populate new radioactive isotopes.*
New London - College in New London NH United States.

(e) Gordon Research Seminar on Nuclear Chemistry: New Directions of Growth in Nuclear Science Through Structure and Reactions.
*Using the alpha-transfer reaction to populate new radioactive isotopes.*
New London - College in New London NH United States

(f) XII Latin American Symposium on Nuclear Physics and Applications
*Alpha-transfer Reaction in Combination with Transient Field Technique and DSAM to Measure Magnetic Moments and Life-Times in $^{110}$Sn and $^{106}$Cd.*
La Havana, Cuba.

3. Publications:

(a) *Populating Low-spin States in Radioactive Nuclei to Measure Magnetic Moments Using the Transient Field Technique*.
Acta Physica Polonica B Proceedings Supplement,2016. DOI: 10.5506/APhysPolB.47.405

(b) *Magnetic Moment Measurements Using Alpha Transfer Reactions-Challenges and Perspectives*.
Springer Proceedings In Physics,2016. DOI: 10.1007/978-3-319-21191-6-12

(c) $Z = 50$ core stability in $^{110}$Sn from magnetic-moment and lifetime measurements.
Physical Review C,2016. DOI: 10.1103/PhysRevC.93.044316

(d) *Magnetic moment and lifetime measurements of Coulomb-excited states in $^{106}$Cd*. Physical Rreview C, 2016. DOI: 10.1103/PhysRevC.94.034303

4. Participation on the Research Project:

*Exploración del surgimiento de la colectividad nuclear en las capas de protones $1f_{7/2}$, $1p_{3/2}$, $1p_{1/2}$, $1f_{5/2}$ y de nuetrones $0f_{5/2}$, $1p_{3/2}$, $1p_{1/2}$, $0g_{9/2}$, $1d_{5/2}$ por medio de la medición de momentos magnéticos y eléctricos en estados nucleares excitados*.

# Abstract

Excited states in the $^{223}_{90}$Th nucleus have been studied. The nucleus presents one of the best examples for parity-doublet structures. The nucleus has been revisited in an experiment using the 80 MeV $^{18}$O + $^{208}$Pb $\rightarrow$ $^{223}$Th + 3n reaction, the GAMMASPHERE $\gamma$-ray and the HERCULES evaporation-residue detector arrays. This work presents a description on the experiment, a status report on the analysis and a discussion of the results. The study of the $^{223}$Th involved the delineation of the high-spin behavior of the yrast structure, i.e. parity splitting as a function of spin where three strict parity doublets have been identified, and also, a tentative fourth parity level on the new structures. A pursuit for a $K < 5/2$ structure was made by the analysis of the parity splitting. The level scheme for $^{223}$Th was constructed with 26 new $\gamma$-ray transitions and 17 new energy levels, but there is not evidence of non-yrast structures due the lack of $E2$-type transitions. New transitions were found for the $^{220}_{88}$Ra and $^{224}_{90}$Th, one for each one.

# Contents

## CONTENTS

# List of Figures

# List of Tables

# List of symbols

| | |
|---|---|
| $E1$ | Transition energy of dipole multipolarity. The spin states in nuclei with octupole deformation, with an spin difference of $\Delta I = 1$ and with opposite parity are linked by strong $E1$ transitions. |
| $E2$ | Transition energy from rotational excited states of quadrupole multipolarity. |
| $E_r$ | Relative energy: $E_{I,s=+i} - E_{I,s=-i}$. |
| $I$ | Total nuclear angular momentum. It satisfies the rule of classical angular momentum. The total angular momentum of a subatomic particle is the sum of the orbital angular momentum plus its spin value. Superscript indicates the parity of the spin state. |
| $K$ | Projection of the total nuclear spin, $I$, over the symmetry axis. |
| $\hat{P}$ | Parity Operator. It inverts the spacial coordinates $(x, y, z)$ by $(-x, -y, -z)$. Eigenvalue of the $P$ operator can be $\pm 1$. |
| $\hat{S}$ | Simplex operator. It rotates the system around an axis out off the principal symmetry plane. |
| $\hbar$ | Planck's constant 6.58211899(16)x$10^{-22}$ MeV·s. |
| $\mu_N$ | Nuclear magneton: 3.1524512550(15)$\times 10^{-14}$ MeV/T. |
| $\sigma$ | Sigma operator. It rotates the system $\pi$ rad around an axis symmetry. |
| $g$ | Nuclear giromagnetic factor: $g_{free\ neutron} = -3.8263$, $g_{free\ proton} = +5.5858$. |
| $j$ | Angular momentum of the independent particle: $j = \ell \pm 1/2$. |
| **c** | Speed of the light in the vacuum $c = 299,792,458$ m/s. |

## ACRONYMS

**keV** $10^3$ eV.

**MeV** $10^6$ eV.

**Q** Electric quadrupole moment barn=$10^{-28}$ $m^2$.

**yrast** Set of states of minimum energy for each spin-value.

*The most beautiful thing we can experience is the mysterious. It is the source of all true art and science.*

Albert Einstein

CHAPTER

# 1

# Introduction

The deep understanding of the nature of the interaction between nucleons in stable and radioactive nuclei is the main goal of nuclear structure studies. In the prosecution of this objective, several theoretical efforts and experimental campaigns have been performed during the last decades to uncover the laws of the nuclear interaction. These efforts allowed the measurements of quantum numbers that characterize the nuclear wave function, and are the base for the testing of nuclear structure models.

The onset of deformation in the atomic nucleus lead to the arising of new quantum numbers that modify the functional form of the nuclear potential. Each quantum number, such as energy transition ($E$), spin ($I, j$), parity ($p$), simplex ($s$) and the projection of the spin along a symmetry axis $K$, is associated to a symmetry in the nuclear potential. Usually an axial symmetric deformation, including one with a reflection-asymmetric (pear-like) shape, leads to rotational bands described with quantum number of spin, parity and simplex. Currently, there is a lack of information on the spectroscopy of odd mass octupole nuclei in the actinide region [1] which is summed in chapter 3. One of the signatures observed in excitation spectra associated with broken reflection symmetry is the presence of bands of states with opposite parity. For example, even-even nuclei show (in addition to even-spin and positive-parity bands) low-lying rotational bands with odd spin and negative parity. Their neighboring odd-A nuclei exhibit sometimes sets of such alternating-parity sequences. Moreover, these sequences are found nearly degenerate in energy, and are called *parity doublets* [2]. Also, there are strong transitions between these bands with opposite

parity, which are associated with an induced electric dipole moment. Right side of Fig. 1.1 summarizes some of the experimental evidences of octupole-type excitations which are matter regard to $^{223}$Th. More specifically the evidences are for $^{223}$Th:

- Low-lying states with negative parity for an odd-A nuclei
- High probability of $E1$ transitions between yrast bands of opposite parity.
- Odd-mass nuclei: In many cases four bands are exhibited with nearly degenerated energy levels, with the same spin and opposite parity (parity doublets. See right side of Fig. 1.1).
- The spin states belonging to different bands with equal spin but opposite parity (parity doublets) can be linked by $M1$ transitions.
- For each bandhead with $K^{\pm}$ there could be another bandhead with $K^{\mp}$ close in energy.
- The energy degeneracy (all $I^{\pm}$ are possible) indicates that $s$ (simplex number) is not a good quantum number and it implies a rotation that is not around the principal cranking axis (analogy with high-$K$ bands where the role of the odd-particle is that of a gyroscope: it tilts the rotational axis).

The level scheme represented in Fig. 2.11 for an Odd-A nucleus is the matter of this work

To perform an experimental study of the excited states of the $^{223}$Th nucleus is the aim of this work. For that, it is necessary a high resolution $\gamma$ ray and residual nuclei $\gamma$ ray spectroscopy to look for additional band-like structures in the such like isotope, representative of the A$\sim$220 mass region. The use of a high-resolution $\gamma$-ray array, GAMMASPHERE [3] in conjunction with the HERCULES [4] detector allows a clean selection with high statistic and good $\gamma$-ray resolution and multiplicity. As part of the training process to understand the $\gamma$ ray spectroscopy analysis and the experimental procedure for nuclear reactions, one experiment was performed in the cyclotron at Lawrence Berkeley National Laboratory to measure nuclear magnetic moments and lifetimes of the first excited states of $^{110}$Sn [5] and $^{106}$Cd [6] using $\alpha$-transfer reaction technique with two published articles on the *Physical Review C* as outcome of that project. For this study, the $^{208}\mathrm{Pb}\left(^{18}\mathrm{O}, 3\mathrm{n}\right)^{223}\mathrm{Th}$ fusion-evaporation reaction was performed at Argonne National Laboratory, USA, by the Nuclear Chemistry Group from Washington University in collaboration with the Grupo de Física Nuclear de la Universdiad Nacional de Colombia. All experimental tools have been considered in detail in chapter 4.

The experimental data presented in chapter 5 permits to extend the accepted level scheme for $^{223}$Th and to confirm the latest results of the level scheme of the $^{223}$Th published by Maquart *et. al.* [7]. It has extended our knowledge of the collective behavior of the nucleus, not only in the well known ($K = 5/2$) parity doublet structures but also expected $K < 5/2$ bands. Being the $^{223}$Th$_{133}$ one of the best known examples of the existence of parity doublet structures, it is an attractive case for two reasons: (1) Recent results for $^{221}$Th in Ref. [8] suggest that, in addition to the yrast parity doublet like structures in $^{223}$Th excited structures of different configurations with $K < 5/2$ could be present in the nucleus. The identification of such structures would be crucial to have a complete identification of the odd-neutron states responsible for octupole shapes in this mass region. (2) The analysis of the M1 transitions in the $^{223}$Th yrast structure is sort of pending. The new transitions could provide useful information and the present $K = 5/2$ assignment could be solidified with an improved data set for $^{223}$Th, which is at hand. Outlook and perspectives have been provided in chapter 7.

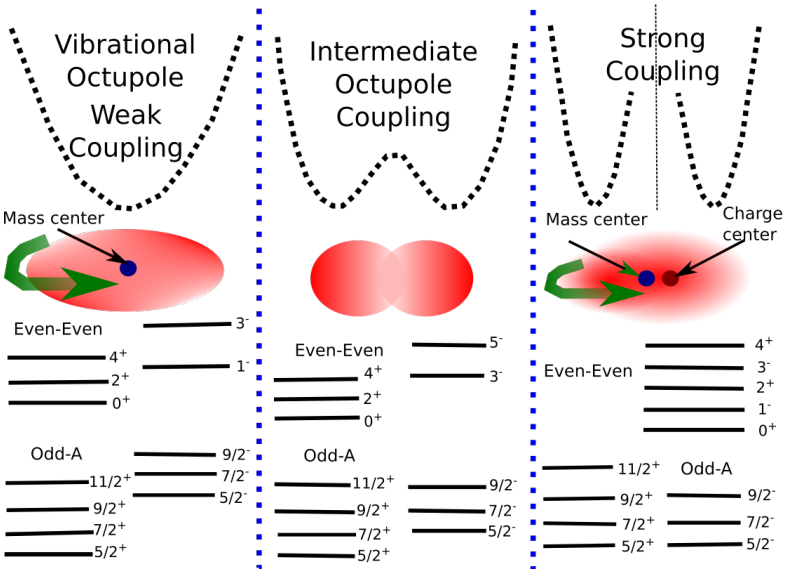


**Figure 1.1:** A review of the different couplings that relates to intrinsic reflection asymmetry in atomic nuclei. The observed collective bands in Even-Even and Odd-A nuclei are presented. The vast majority of collective bands can be located in the middle panel, while few examples can be identified with the strong coupling, among them the yrast structure of $^{223}$Th nucleus [9]. The latter can be viewed as a displacement of the protons relative to the neutrons inside the nucleus [2].

*The saddest aspect of life right now is that science gathers knowledge faster than society gathers wisdom*

Isaac Asimov

CHAPTER

# 2

# Theoretical Framework

In the develop of the science, there are two levels on the formulation of the knowledge: Models and theories. The firs one, help us to the phenomenological understanding through experimental data. The model is an analogy of the reality with approaches and similarities regard to the phenomena. Several different models can explain the same fact and can be fitted to the same set of the experimental results. Theories involve formal asseverations expressed in mathematical language which unveil Nature Laws. The theory unifies the abstract thinking in a single corpus. Currently, many different models point to the same claim: Unveil the nature of the nuclear interaction. Nuclear models are often classified such as independent particle or collective behaviors. In this section a general vision of those categories will be presented.

## 2.1 Nuclear Models

The atomic nucleus is compound by neutrons and protons. Special quantities characterize the properties of these subatomic particles, namely, mass, charge, magnetic moment and spin. Fig. 2.1 summarizes the numbers that describe the properties of protons and neutrons. The residual strong interaction that keeps quarks together is responsible for the stability of the atomic nucleus. The average nuclear potential can be seen as originating from a mean field which depends on the interaction of one nucleon with the remaining ones. The associated distribution of the nuclear mass and charge give us, in turn, information about the nuclear shape and, to some degree, the symmetries of the nuclear potential. The use

of high-resolution $\gamma$-ray spectroscopy, working in coincidence with ancillary detectors for residual nuclei and charged particles, provides a powerful tool to obtain the experimental input for these studies. Effective mean fields have been introduced to explain the nature of the nuclear interaction. Experimental results provide vital information for the modeling of the nuclear potential.

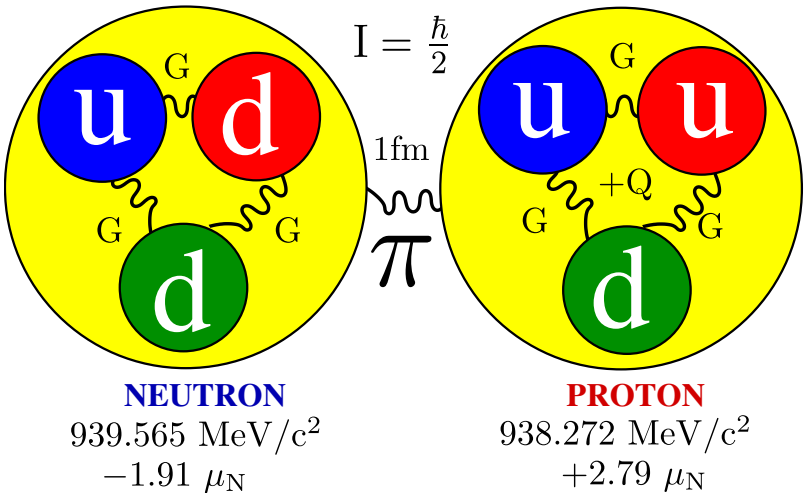


**Figure 2.1:** Protons and neutrons are composed by quarks. The strong interaction is mediated by gluons and the nuclear interaction is mediated by mesons. The masses for a free proton and a free neutron are 938.272 MeV/$c^2$ and 939.565 MeV/$c^2$ respectively, with c the speed of light in the vacuum [10].

Protons and neutrons are confined into a volume with an average radius $R = 0.853A^{1/3} + 0.496$ fm and in this range the mean nuclear potential is atractive. If the distance between two nucleons is smaller than 0.5 fm , it will appear an asymptotic repulsion, otherwise, if the distance between them is larger than 2 fm, the nuclear interaction will vanish. Fig. 2.2 shows an approach to the functional form of the nuclear potential for protons (red line) and neutrons (blue line). The protons have a positive electric charge that produces a Coulomb repulsion which establishes a positive maximum peak on the curve of the mean field. For the last reason, the potential for neutrons is deeper than for protons.

### 2.1.1 The Liquid drop model

The nucleus can be seen as a liquid drop where its constituents particles interact with the closest neighbours (See Fig. 2.3). Protons and neutrons are bound among of the nuclear volume, however, protons due to the electrical charge and Coulomb repulsion tend to reside

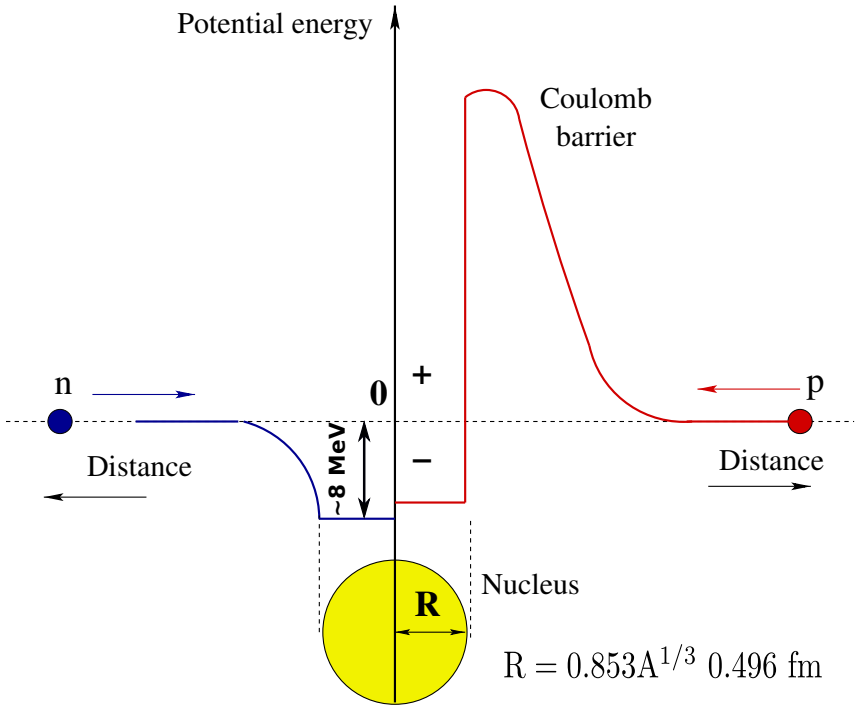


**Figure 2.2:** A sketch of the nuclear potential as a function of the distance R. Nucleons interact attractively among a volume with radius between 1.2-8 fm. The interaction vanishes far from 2 fm. For protons, the Coulomb potential reduce the deep of the nuclear potential and creates a Coulomb barrier [11].

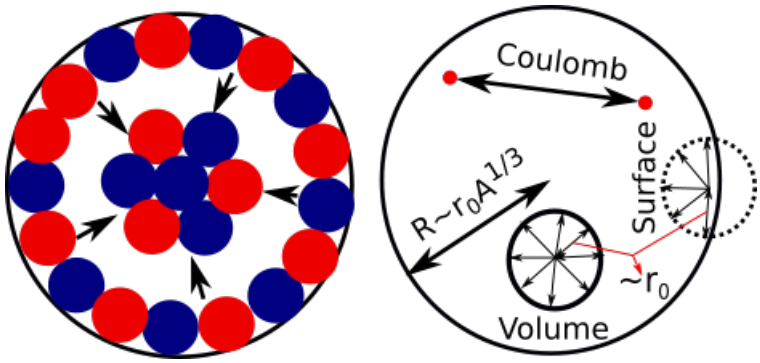


**Figure 2.3:** The Bethe-Weizsäcker mass formula summarizes the theoretical nuclear liquid model. There are five energy terms: Volume($a_\nu$), Surface($a_s$), Coulomb($a_c$), Symmetry($a_A$) and Pairing. See text for details [12].

closest to the surface. The particles which are on the surface of the nuclear volume interact with less neighbours and its binding energy decreases. The Weiszäcker mass formula is

a correction to the first approximation to the liquid model. The semi-empirical formula calculates the binding energy per nucleon , $(BE(A,Z)/A$ as the necessary energy to extract one nucleon from the nucleus. This formula has five terms with experimental coefficients that multiply the $A$ mass number: Volume ($a_\nu$) , Surface ($a_s$), Coulomb ($a_c$), Symmetry ($a_A$) and pairing ($\delta$) are the energy quantities involved in this nuclear model [13].

$$BE(A,Z) = a_\nu A - a_s A^{2/3} - a_c Z\frac{Z-1}{A^{1/3}} - a_A\frac{(A-2Z)^2}{A} \pm \delta \tag{2.1}$$

**Volume** ($a_\nu$): The nucleons are packaged into nuclear volume and because of the nuclear strength there is a binding energy per nucleon ($BE(A,Z)/A$). Because all nucleons interact with the same nuclear neighbours, the binding energy is equal for every one of the particles. The volume energy contributes with $a_\nu = 15.85$ MeV per nucleon to the binding energy of the nucleus. This quantity come from the Fermi energy concept. If $n = A/\frac{4\pi R^3}{3}$ is the density of nucleons, then the Fermi energy is equal to:

$$E_F = V_0 + \frac{\hbar}{2m}\left(\frac{3\pi^2 A}{\frac{4\pi R^3}{3}}\right) \tag{2.2}$$

According to the nucleus radius, this Fermi energy-value can be calculate between 15.85 and 18.7 MeV per nucleon.

**Surface ($a_s$).** In Fig. 2.3 can be seen that the surface particles have less surrounding nucleons and the binding energy must be reduced. At the outward surface of the nucleus there is no nuclear interaction. The surface term must be proportional to the area: $4\pi R^2 = 4\pi\left(1.2A^{1/3}\right)^2 \sim 18.1A^{2/3}$ MeV.

**Coulomb** ($a_c$): Protons have positive charge and the Coulomb potential increases with short-distances. Thus, the electrical repulsion will diminishes to the total binding energy. If the shape of the nucleus is to be spherical, the Coulomb energy must be proportional to the charge density and the $a_c$ factor has been calculated to be equal to 0.71 MeV.

**Symmetry** ($a_A$): Nuclei with the same number of neutrons and protons are more stable. If the neutron number increases, the stability of the nuclei is changed. The binding energy is smaller in heavy nuclei than nuclei with Z=N. The fourth term in the mass formula ($\sim 23.7$ MeV) represent this correction in the binding energy.

**Pairing** ($\delta$): On the other hand, protons tend to join each other in pairs (neutrons behave in the same way). Thus, the nucleons are more bound in the even-even nuclei than in odd-odd nuclei. The coefficient value has been calculated as $+\delta \sim 12$ MeV for even-even, $-\delta \sim 12$ MeV for odd-odd and $+\delta \sim 0$ for odd-even nuclei.

The Bethe-Wiszäcker mass formula predicts the largest binding energy (lowest mass excess) for each isotope on the nuclear map. Fig. 2.4-(b) shows the more stable nuclei located along of the stability line defined by the following equation:

$$Z_0 = \frac{A/2}{1 + 0.0077A^{2/3}} \tag{2.3}$$

The cross section of nuclei in the stability valley determines one parabolic curve for isobar nuclei (Fig. 2.4-(a)). The left side from the minimum defines the $\beta^+$-decay and the right side, the $\beta^-$-decay.

### 2.1.2 The Fermi gas model

The Fermi gas model considers the nucleons as independent particles moving in the nucleus and its individual wave functions are taken to be plane waves. It is say, the particles confined among a nuclear volume behave approximately as an ideal gas. The statistics of Fermi is applied to calculate the distribution of states density on the square potential well. Eq. 2.2 define the Fermi energy around 33 MeV. Fig. 2.4-(d) shows that the binding energy for the most of the isotopes is between 7 and 8 MeV. Then, the total deep of the nuclear potential is:

$$V_0 = E_F + B(E) \sim 40 \text{ MeV} \tag{2.4}$$

Protons and neutrons are located into two different potential wells with approximately the same deep, otherwise, the nuclei would be unstable because one of the potential well would be more favorable regard the second one, and the nucleus tend to the stability by $\beta$-decay (see Fig. 2.4-(a)). In heavy nuclei there is an excess of neutrons, for the last reason the potential well is deeper because the stability. Also, it would be thought that the Coulomb repulsion in protons contributes to the difference in the potential shown in Fig. 2.5.

### 2.1.3 The Nuclear Shell Model

The Fermi gas model cannot explain completely neither the binding energies of nucleus nor the complex interactions in the inner of the nucleus such as pairing and asymmetry. Fig. 2.6 shows that the nucleus can have a shell structure because the experimental evidence of the magic numbers [14, 15]. There are specific orbitals where the binding energy is a

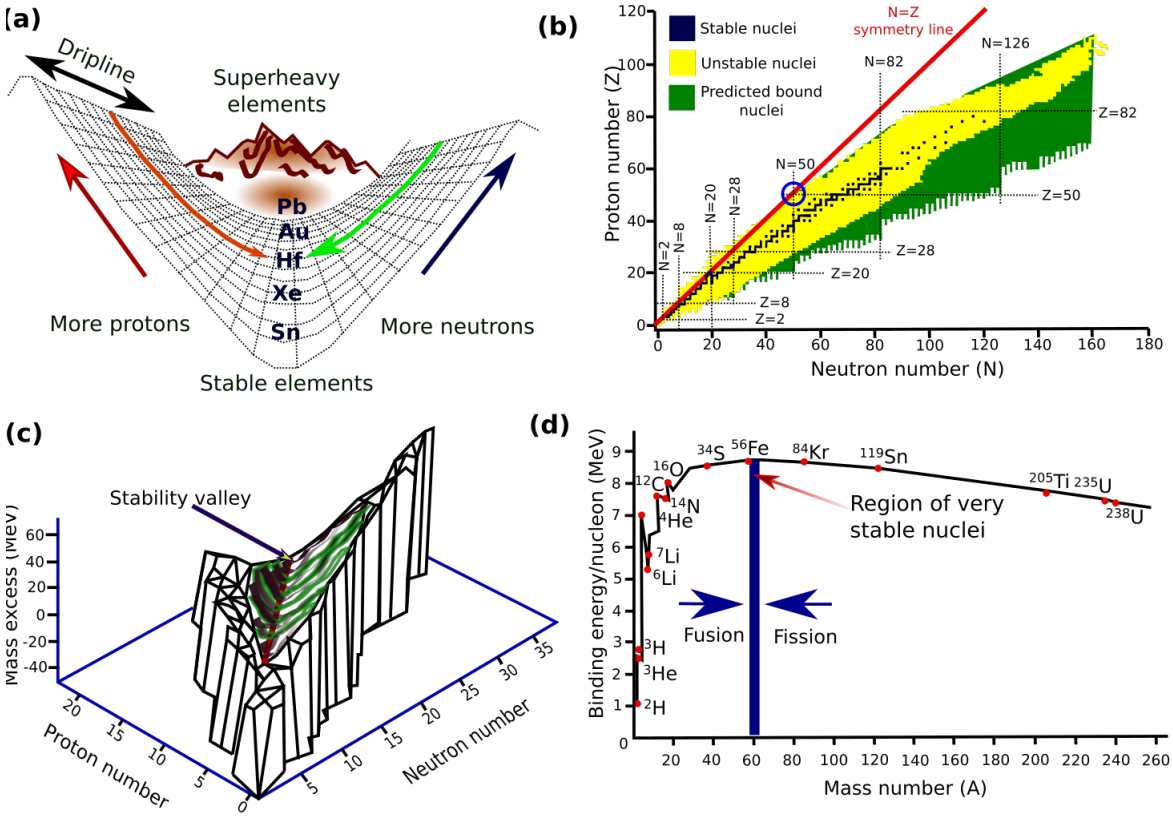


**Figure 2.4:** (a) An artistic view of the valley of stability. Stable nuclei are located at the bottom of the valley, nuclei with excess of neutrons or protons go up to the mountains and have the tendency to return to the bottom. Super heavy elements are located at the end of the valley. Nuclei with excess of nucleons move down the valley towards stability. The neutron side of the valley is poorly understood and the neutron-dripline is very diffuse. (b) Chart of nuclides, where proton number is plotted against the neutron number. Stable nuclei are plotted in black, while unstable nuclei, are in other colors. $Z_0$ defines the minimum points (black points) of the stability valley on the plane of the protons versus neutrons. (c) The height of the valley indicates the excess of the energy. More energy, less stability because the nucleons tend to found one point over the stability line [13]. (d) $^{56}$Fe is located in the region with the largest binding energy per nucleon. The liquid drop model explains the nuclear fusion and fission processes.

maximum. The energy decreases until a minimum and return to other maximum. This behaviour is similar to the shell structure of the electrons on its own atomic orbitals.

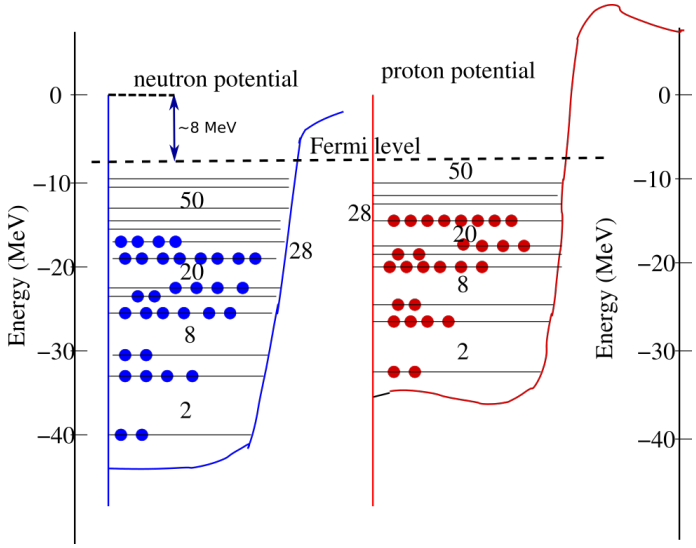


**Figure 2.5:** The potential wells for protons and neutrons have been modeled as square well. The proton potential well is deeper than the neutron well because there is a Coulomb repulsion that reduce the binding energy. Besides, the upper curve for the protons well describes the dominant electric interaction when the nuclear strength is weak because the proton is on nuclear surface. Nucleons, with spin $1/2\hbar$, obey the Pauli Exclusion Principle which establishes that two fermions cannot be in the same quantum state.

The first step in the nuclear shell model was to solve the Schrödinger equation (Eq. 2.5) for the harmonic and square potential well. Here, the particles move among a mean central potential. Fig. 2.7 shows the eigenvalues for energy and angular momentum. The nuclear magic numbers are not coincident with the theoretical prediction, this is why the nuclear potential must be modeled with a more complex shape than the harmonic oscillator and square potential well. In Eq. (2.5), a phenomenological potential $V(r)$ was introduced to achieve the predictions to be fitted to the experimental data. The Woods-Saxon potential is between the harmonic oscillator and square potential well and describe the behaviour of a single particle moving among a mean field. In Eq. (2.6), $R = 1.2A^{1/3}$, $r$ and $a$ are adjustable parameters for diffuseness of the nucleus skin. However, Woods-Saxon potential no explains the energy gap observed from the experimental measurements of the liquid drop model.

$$\left(-\frac{\hbar}{2m}\frac{1}{r}\frac{d^2}{dr^2}r + \frac{\hbar\ell(\ell+1)}{2mr^2} + V(r) - E\right)R(r) = 0 \tag{2.5}$$

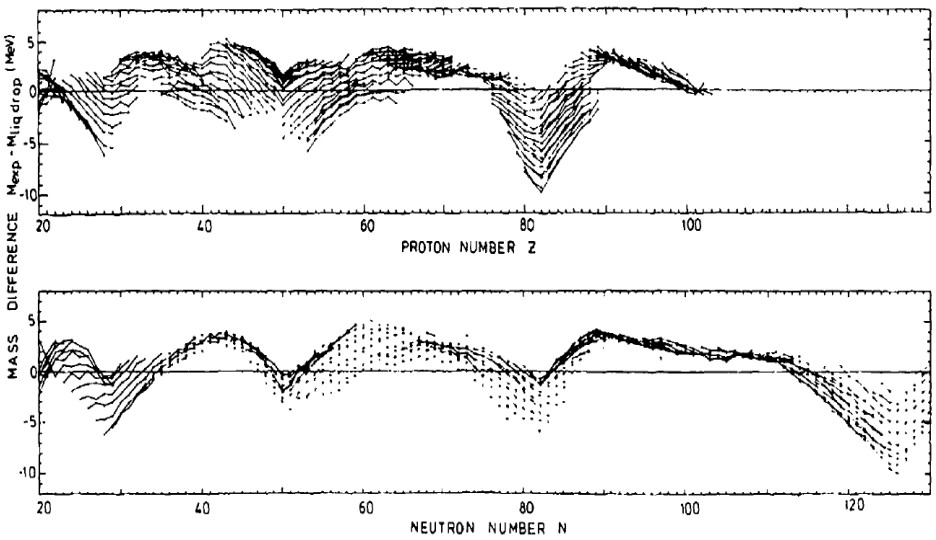


**Figure 2.6:** The calculus of the binding energy shows that the defect mass is minimum for specific protons and neutrons numbers. The larger binding energy for those configurations lead to the idea of a shell structure for the nucleus as the configuration of the electrons in the atom. The vertical axes determines the difference between Experimental data and the calculus of the binding energy of the liquid-drop model without corrections. In this case, there is evidence of the magic numbers on 20, 28, 50 and 82 for protons and 20, 28, 50, 82 and 126 for neutrons. Figure taken from ref [16].

$$V(r) = \frac{V_0}{1 + e^{\frac{r-R}{a}}} \tag{2.6}$$

#### 2.1.3.1 **Spin-orbit interaction.**

In 1949 Maria Goeppert Mayer, and in parallel Haxel, Jensen&Süess published each articles where the spin-orbit interaction was introduced [14, 15]. The contribution led them to be awarded the Nobel Prize in 1963. The spin-orbit interaction explains the existence of the magic numbers and predicts the binding energies for them. The following assumptions are taken verbatim from the Mayer's original article [14]:

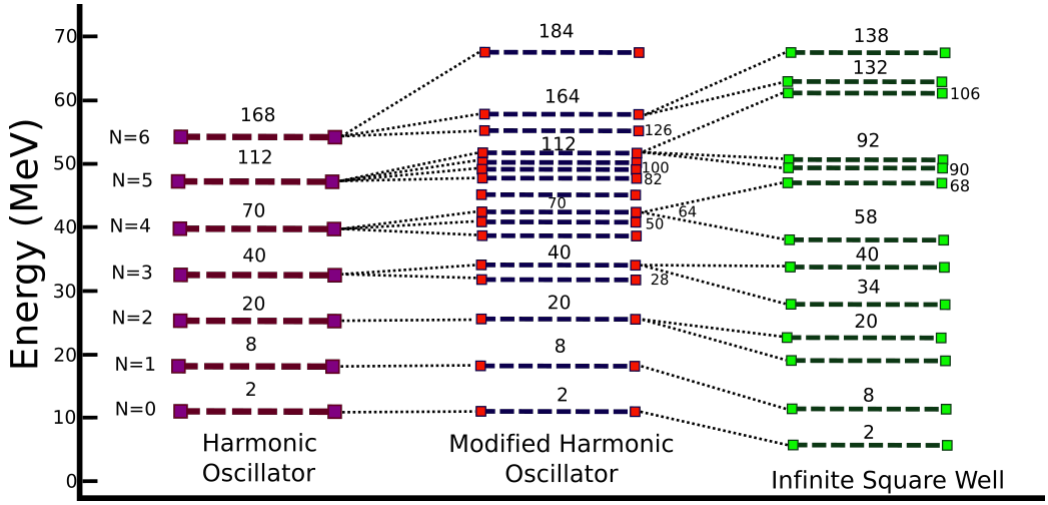


**Figure 2.7:** A comparison between the solution of the Schröringer equation for the harmonic oscillator and the square potential well for a nucleus with A∼82 [17].

*(1) The succession of energies of single particles orbits is that for a square well with strong spin-orbit coupling giving rise to inverted doublets.*
*(1a) For given $\ell$, the level $j = \ell + \frac{1}{2}$ has invariably lower energy and will be filled before that for $j = \ell - \frac{1}{2}$.*
*(1b) Pair of spin levels within one shell, which arise from adjacent orbital levels in the square well in such a way that spin-orbit coupling tends to bring their energy closer together can, and very often will, cross.*
*(2) An even number of identical nucleons in any orbit with total angular momentum quantum number $j$ will always couple to give a spin zero and no contribution to the magnetic moment.*
*(3) An odd number of identical nucleons in a state $j$ will couple to give a total spin $j$ and a magnetic moment equal to that of a single particle in that state.*
*(4) For a given nucleus the "pairing energy" of the nucleons in the same orbit is greater for orbits with larger $j$.*

The Mayer's assumptions are the basic postulates of an independent particle model. The closed shell does not contribute neither to the total nuclear angular momentum nor to the total nuclear magnetic moment. The even-even nuclei can be seen as an inert core similar to the noble gas on the VIII-group of the atomic periodic table. The nuclear spin and the nuclear magnetic moment of the nucleus are determined by the unpaired particle wave function on odd-even nuclei.

### 2.1.3.2 Harmonic Oscillator Modified

The Woods-Saxon potential (eq. 2.6) is complicated to solve and this describes the behaviour for one independent particle. Nilsson has proposed a new potential called Modified Oscillator (eq. 2.7). The spin-orbit term is introduced in the Schröringer equation and the solution fits the functional form of the Woods-Saxon potential. The Modified Oscillator potential is an interpolation between harmonic oscillator and square well (see Fig. 2.2) [17].

$$MO = \frac{1}{2}\omega_0^2 M r^2 - \kappa\hbar\omega_0 \left[2\boldsymbol{S}\cdot\boldsymbol{L} + \mu\left(\ell^2 - \langle\ell^2\rangle_N\right)\right] \tag{2.7}$$

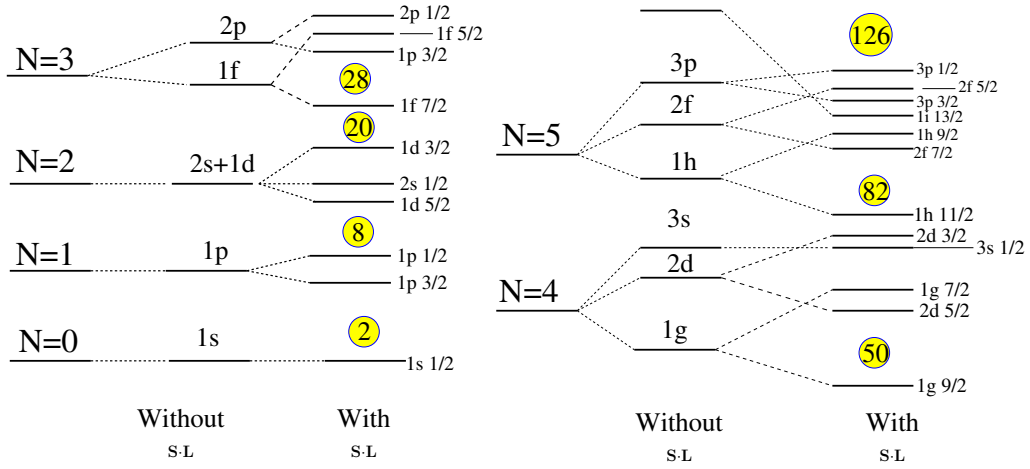


**Figure 2.8:** The potential of the Modified Oscillator is between the harmonic oscillator and the square well. The $\boldsymbol{S}\cdot\boldsymbol{L}$ interaction has been added. $\kappa$ and $\mu$ are fitting parameters for each energy level group.

Fig. 2.8 shows the energy levels for the harmonic oscillator and the Modified Oscillator. The $\boldsymbol{S}\cdot\boldsymbol{L}$ interaction split the $j$-spin in two sub-levels: $j = \ell + 1/2$ and $j = \ell - 1/2$. The parallel spin coupling has more binding energy than anti-parallel pairing, then, the sub-shell with spin $j = \ell + 1/2$ will firstly filled. The magic numbers represents the configurations where the binding energy is a maximum. The nucleons fill each energy level, pairing each other (proton↑-proton↓ and neutron↑-neutron↓). If one level is filled, the contribution to the total spin and the magnetic moment will be null.

## 2.1.4 Other Collective Nuclear Models.

Many nuclei away from closed shells display deformed shapes, and so nucleons interact among of a deformed nuclear mean field too. The different kinds of deformations lead

to broken symmetries, which determine the behaviour of rotational bands [18]. In infinit systems, if a physics quantity takes a zero value in a phase state and a finite value in other one, this quantity is said to be an order parameter. The change of the order-parameter value, when there is a phase transition between two states, can be viewed as a symmetry breaking. In finite systems such as nuclei, symmetry breaking appears when the order parameter in the first phase state is larger than in the second one. Examples for order parameters are: the electric quadrupole moments and the magnetic dipole moments. Fig. 2.9 shows how change the electric quadrupole moment ($Q$) (eq. 2.8) as function of the Z and N numbers. The experimental data are consistent with the shell-model because near to the magic numbers the $Q$ value is around zero. The $Q$ value is maximum in the region between two magic numbers. The electric Quadrupople moment is a measurement of the charge distribution within the nucleus.

$$Q = \frac{3K^2 - I(I+1)}{(I+1)(2I+3)} Q_0;\ Q_0 = \int \rho \left(3Z^2 - r^2\right) dV \tag{2.8}$$

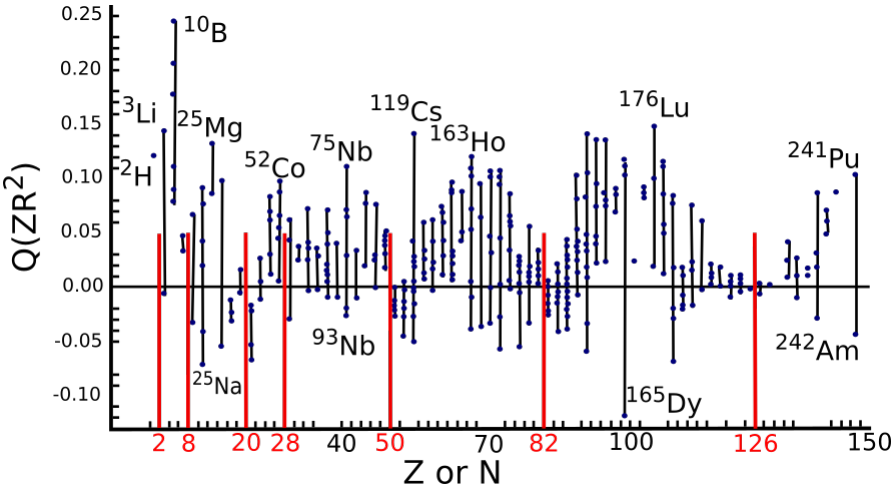


**Figure 2.9:** Experimental data of the electric quadrupole moment. The nuclear deformation increases when the nuclei are far from closed shell [19].

$K$ **number**:

There is another important quantum number which is described by the "crancking model": $K$ is the projection of the total nuclear angular momentum over the symmetry axis, z-axis. This quantum number separates rotational bands with $K = 0$ (even-even nucleus) in two sequences.

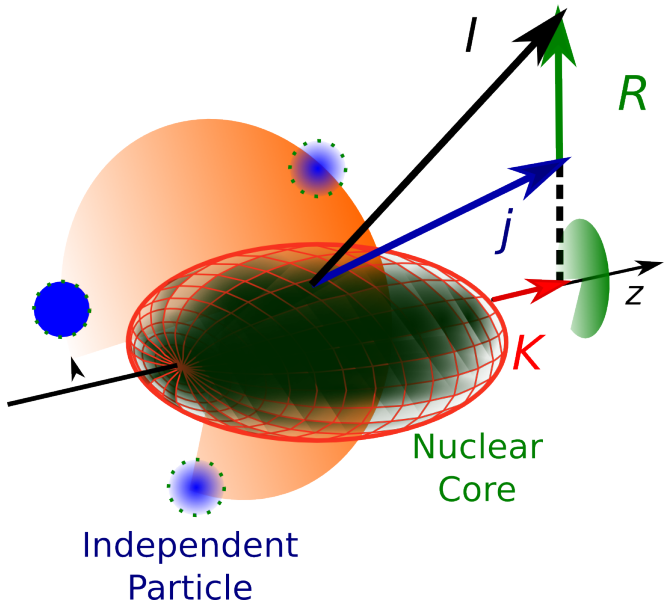


**Figure 2.10:** $K$ is the projection of the total spin, $I = j + R$, over the symmetry axis. $R$ is the core's spin and $j$ is the independent particle's spin. $R = I - j$. The $K$-value is zero for even-even nuclei.

A band consists of a regular sequence of states with defined signature $\sigma$ and parity $p$. The symmetry

$$P\mathfrak{R}^{-1}(\pi)|\psi\rangle = \mathbf{1}|\psi\rangle \tag{2.9}$$

leads to the simplex quantum number $s$ by

$$S|\psi\rangle = e^{-is\pi}|\psi\rangle \tag{2.10}$$

This quantum number fixes the parity for a given spin $I$ [20]. If the rotational axis is not perpendicular to the one of the two symmetry planes, $s$ is not longer a good quantum number. Then a parity doublet for each spin value occurs. The corresponding sets of simplex values are:

$$s = pe^{i\pi I}, \text{ with } p \text{ The eigenvalue of parity operator} \tag{2.11}$$

$$
s = \begin{cases}
 & even-even & \\
+1 & for & I = 0^+, 1^-, 2^+, 3^-, ... \\
 & odd-odd & \\
-1 & for & I = 0^-, 1^+, 2^-, 3^+, ... \\
 & even-odd; odd-even & \\
+i & for & I = 1/2^+, 3/2^-, 5/2^+, 7/2^-, 9/2^+, 11/2^- ... \\
-i & for & I = 1/2^-, 3/2^+, 5/2^-, 7/2^+, 9/2^-, 11/2^+ ...
\end{cases}
$$

Figure 2.11 shows two alternating-parity level sequences with states nearly degenerate in energy with the same spin, but opposite parity (parity doublet) [8]. It is useful to distinguish between even-even, odd-odd and even-odd/odd-even nuclei where $^{223}$Th is an example for the latter case.

#### 2.1.4.1 **Deformations.**

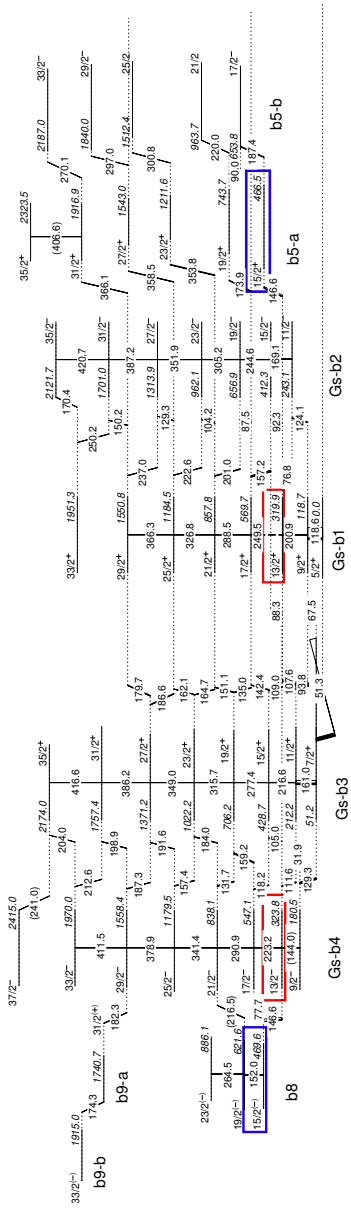


**Figure 2.11:** Level scheme for $^{223}Th_{133}$ constructed in this work. In ref [21] the parity doublet into red boxes was reported ($E_{rel} = -17$ keV, see Figure 3.1). In this work, a second parity doublet was seen (highlighted by the blue boxes). A parity doublet is a pair of states nearly degenerate in energy with the same spin but opposite parity. The b6 and b7 structures have been omitted here. In chapter 5 a complete level scheme is presented.

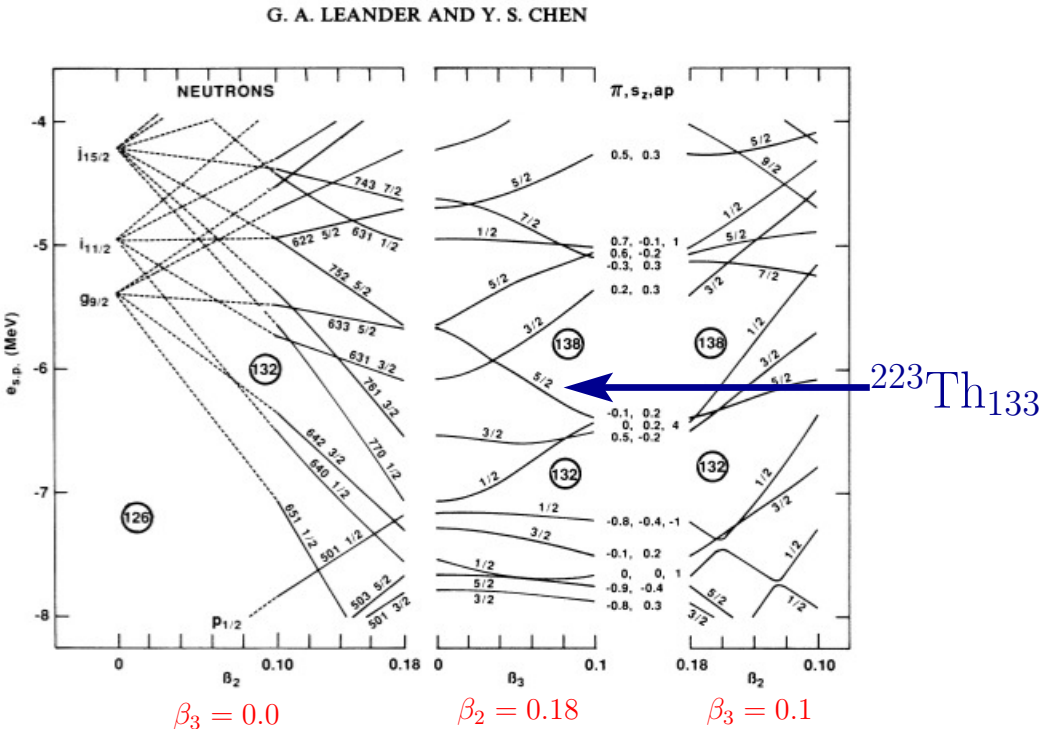


**Figure 2.12:** Neutron single-particle levels using a Wood-Saxon potential from Ref. [22]. The left-most panel has a $\beta_3 = 0.0$ value and a range of values $\beta_2 = 0.0 - 0.18$. In the center panel $\beta_2 = 0.18$ and $\beta_3 = 0.0 - 0.1$. In the right-most panel $\beta_3 = 0.1$ and $\beta_2 = 0.18 - 0.10$. The $K = 5/2$ level that is crucial for the yrast parity-doublet structure of $^{223}$Th, and that is downsloping as a function of $\beta_3$, is highlighted. The predicted deformation values at spin zero are: $\beta_3 = 0.106$ and $\beta_2 = 0.118$, see Table 2.1.

**Table 2.1:** Compilation of $\langle\beta_3\rangle$ values in the region relevant to this proposal. Values are derived from average $B(E1)/B(E2)$ ratios and calculated $\beta_3$ and $\beta_2$ values according to Refs. [8, 23]. The $K$ quantum number represents the assigned configuration. Additional entries for $^{223}$Th (left partially blank) accommodate additional $\beta_3$ and $\beta_2$ values from Ref. [23].

| Nucleus | $\overline{B(E1)/B(E2)}$ ($10^{-6}$ fm$^{-2}$) | $\langle\beta_3\rangle$ | $2\cdot\beta_3$ | $\beta_3$ | $\beta_2$ | $K$ |
|---|---|---|---|---|---|---|
| $^{221}$Th (y) | 2.17 (24) | 0.215 (12) | 0.180 | 0.090 | 0.101 | $1/2$ |
| $^{221}$Th (b, c) | 2.28 (37) | 0.220 (18) | 0.220 | 0.110 | 0.094 | $5/2$ |
| $^{223}$Th | 1.68 (32) | 0.189 (18) | 0.212 | **0.106** | **0.118** | $5/2$ |
| $^{223}$Th | | | | 0.108 | 0.112 | $1/2$ |
| $^{223}$Th | | | | 0.095 | 0.121 | $3/2$ |
| $^{225}$Th | 0.83 (31) | 0.133 (25) | 0.216 | 0.108 | 0.137 | $3/2$ |
| $^{219}$Ra (y) | 1.65 (7) | 0.188 (4) | 0.166 | 0.083 | 0.092 | $1/2$ |
| $^{219}$Ra (I) | 1.07 (28) | 0.151 (19) | 0.142 | 0.071 | 0.088 | $3/2$ |
| $^{221}$Ra | 0.93 (14) | 0.141 (10) | 0.202 | 0.101 | 0.107 | $5/2$ |

The experimental evidences have established that the positive-parity states are regarded to even-multipolarity nuclei, and the odd-multipolarity nuclei show negative-parity states which are mainly determined by octupole deformations (reflection-asymmetric) [24]. The alternating parity bands in actinide nuclei, built from spectra with some specific properties show that those nuclei exhibit not-only nuclear rotation collectivity (axial deformation) but also non-axial deformation. Figure 2.12 and table 2.1 present experimental $\beta$ values regard to the deformation of radioactive nuclei. $\beta$ is a deformation parameter defined by the Modified Oscillator model.

#### 2.1.4.2 The Nuclear Rotor.

Aage Bohr and Ben R. Mottelson shown that the energies of the excited states of a nucleus with quadrupole deformation can be sorted out in a rotational band, defined as a set of states with the same parity and $\gamma$-energy transitions in a cascade showing a systematic spacing according to the eq. 2.12. The even-even nucleus is seen as a rigid body which rotates around an axes perpendicular to the symmetry plane. This rigid body has a constant moment of inertia $\Im$ [25].

$$E_I = \frac{\hbar}{2\Im} I(I+1);\ I^\pi = 0^+, 2^+, 4^+, ... \tag{2.12}$$

There are three experimental evidences of the rotational states of the nucleus:

- The lifetimes for independent particle states are shorter than rotational states.
- The energy of the first excited state is larger for nuclei around closed shell than nuclei with mass number between magic numbers.
- The energies of high spin states are consistent with Eq. (2.12). In a simplest model, the inertia moment is to be constant and the excited states are considered as promotion of a set of nucleons that align its spin to the symmetry axes, and then, high spin states can be obtained. Also, vibrational effects have not been included [17].

#### 2.1.4.3 The crancking model.

Equation (2.13) shows the hamiltonian of the crancking model –proposed by Inglis (1954) [26]– where the rotational axis is denoted as $z$-axis. $\hat{J}_z$ is the corresponding component of the total angular moment. Equation (2.14) is the hamiltonian in the rotating frame. $V$ describes the rotating mean field potential.

$$\hat{H}' = \hat{H} - \omega \hat{J}_z \tag{2.13}$$

$$h' = T + V - \omega \hat{J}_z \tag{2.14}$$

Figures 2.13 and 2.14 shown the possibilities of how the mean field could rotate according to the choosing of the rotation-axis. Here, the rotating mean field has a mirror symmetry or asymmetry about the principal planes.

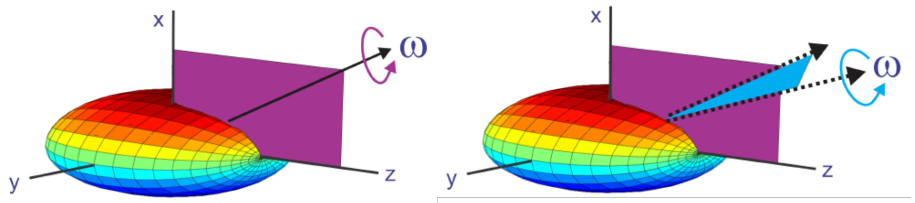


**Figure 2.13:** The case where the $\Re_z(\pi)$ symmetry is broken and the $I$ values have not restriction. Left: rotation-axis in a principal plane. Right: rotation-axis out of a principal plane.

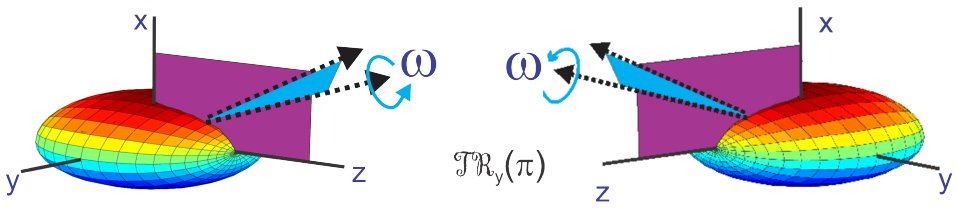


**Figure 2.14:** This case of study considers two identical $\Delta I = 1$ sequences with the same parity, which are the even and odd linear combinations of the left- and right handed mean-field solutions. Two degenerated states are obtained by applying space inversion: $|\psi\rangle$ and $\boldsymbol{p}|\psi\rangle$. For additional details see Refs. [20] and [18]

The mean field is, for mirror symmetry, quantized on three principal planes. Table-I summarizes the possibilities of a symmetry breaking and the consequences for the rotational bands.

#### 2.1.4.3.1 Rotation about z-axis

If the nucleus is "pure" rotational, the hamiltonian must be conserved under rotations of $\pi$ degrees around an axis perpendicular to the symmetry axis. This is represented by the operator:

**Table 2.2:** Discrete Symmetries of the rotating mean field. Columns 1, 2 and 3 indicate the operations that conserve or break the symmetries. S means the mean field does not change and D it does. Column 4 describes the number of rotating bands which can be seen from the experimental results. The blue row is the seen structure in the level scheme of $^{223}$Th. For a complete theoretical develop about it see Ref. [20].

| $P$ | $\Re_z(\pi)$ | $T\Re_y(\pi)$ | Level Sequence |
|---|---|---|---|
| S | S | S | $I^+, (I+2)^+, (I+4)^+, \ ...$ |
| S | D | S | $I^+, (I+1)^+, (I+2)^+, \ ...$ |
| S | D | D | $2I^+, 2(I+1)^+, 2(I+2)^+, \ ...$ |
| S | S | D | $2I^+, 2(I+2)^+, 2(I+4)^+, \ ...$ |
| S | S | $\Re_z(\pi)$ | $I^+, (I+1)^+, (I+2)^+, \ ...$ |
| D | S | S | $I^\pm, (I+2)^\pm, (I+4)^\pm, \ ...$ |
| D | D | S | $I^\pm, (I+1)^\pm, (I+2)^\pm, \ ...$ |
| D | S | D | $2I^\pm, 2(I+2)^\pm, 2(I+4)^\pm, \ ...$ |
| D | D | $\Re_z(\pi)$ | $I^\pm, (I+1)^\pm, (I+2)^\pm, \ ...$ |
| $\Re_z(\pi)$ | D | S | $I^+, (I+1)^-, (I+2)^+, \ ...$ |
| $\Re_z(\pi)$ | D | D | $2I^+, 2(I+1)^-, 2(I+2)^+, \ ...$ |
| $T\Re_y(\pi)$ | S | D | $I^\pm, (I+2)^\pm, (I+4)^\pm, \ ...$ |
| $T\Re_y(\pi)$ | D | D | $I^\pm, (I+1)^\pm, (I+2)^\pm, \ ...$ |
| $\Re_z(\pi)$ | D | $\Re_z(\pi)$ | $I^+, (I+1)^-, (I+2)^+, \ ...$ |
| D | D | D | $2I^\pm, 2(I+1)^\pm, 2(I+2)^\pm, \ ...$ |

$$\mathfrak{R}(\pi)|\psi\rangle = e^{-i\sigma\pi}|\psi\rangle \tag{2.15}$$

with $\sigma$ being the signature quantum number. The spin satisfies the condition: $I = \sigma + 2n$; $n = 0, 1, 2, 3, 4, ...$

$$\langle\mathfrak{R}(\pi)\rangle = (-1)^I = \sigma$$

#### 2.1.4.3.2 Rotation-axis into principal plane

An interesting case is the following scenario, the rotational axis is tilted away from the principal axis, but still lies in one of the three principal planes (See left side of Fig. 2.13. Then there is a only band with $\Delta I = 1$ and the same parity. The signature is not a good quantum number (see Sec. F.4. of [18]).

#### 2.1.4.3.3 Rotation-axis out of the principal planes

The right side of Fig. 2.13 represents the application of the rotation operator around an axis out of the principal symmetry plane. Fig. 2.14 shows the application of two operators: the first operator is the rotation of $\pi$ degrees around an y-axis and the second one, the time reversal operator. In this case there are two degenerated values of energy with opposite "handedness" or chirality (For more details, see Sec. II.F.5 of [18]). Fig. 2.11 represents the complex level scheme of a pear-like nucleus, the odd-mass isotope $^{223}_{90}$Th. Its alternating parity bands are classified according to their parity and simplex quantum numbers [2]. Nowadays, there is a challenging task to explain the connection between the experimental results (leading to a detailed level scheme) and the deformed nuclear shape using mean field models and comparable approaches.

**Mathematical construction of the nuclear shape:**

A general shape of the nucleus, can be described as an expansion of spherical harmonic functions [2]

$$R(\theta,\varphi,t) = c(\alpha)R_0\left[1+\sum_{\lambda=1}^{\infty}\sum_{\mu=-\lambda}^{\lambda}\alpha_{\lambda\mu}Y_{\lambda\mu}(\theta,\varphi)\right] \tag{2.16}$$

where $R_0 = 1.2A^{1/3}$, $\lambda$ is the multipolarity index of the $Y$ spherical harmonic. The equation of the nuclear surface establishes the matrix elements and its relevance on the multipole-multipole correlations on the energy surface: If the $Y_{20}$ are large between closest orbitals, then there is reflection symmetry quadrupole shapes, on the other hand, if the $Y_{30}$ matrix elements are large between orbitals, the octupole is dominant. According to the latter, $2f_{7/2}$ and $1i_{13/2}$ are close in energy, also, $2g_{9/2}$ and $1j_{15/2}$. It would imply that the best octupole correlation could be seen for Z=88 and N=134 [27]. According to the $Q_2$ and $Q_3$ multipoles, there is a mix of the quadrupolo-octupole deformation. The experimental spectra of a nucleus with quadrupole deformation leads to band-heads with $K^+ = 0$ and a sequence of states with $\Delta I = 2$. If there is a soft energy surface due to the octupole

vibration, built on the ground state, a second sequence of states with negative parity will appear with an energy higher than the positive-parity band. Also, it is possible to have an stable octupole deformation with an alternating parity band, because there is an octupole deformation which arise from the coupling between close-lying states with $\Delta j = 3$ [28]. For the last, could be two minimum, one for the reflection symmetric shape, the second one, for the stable octupole band [29]. Then, there are a strong, intermediate and weak coupling interaction.

*We live in a society exquisitely dependent on science and technology, in which hardly anyone knows anything about science and technology.*

Carl Sagan

CHAPTER

3

# State of the art

The main signature of existence of parity doublets is the existence of degenerate states in energy with the same spin but opposite parity. M. Dahlinger *et al* reported parity-doublet structures from yrast states in $^{223}$Th [21], while recent result for the neighbor $^{221}$Th report nearly degenerated parity-doublet sequences from non-yrast states [8]. Parity-doublets structures have been observed in the odd thorium isotopes $^{219,221,223,225}$Th [7, 8, 21, 30, 31]. The systematic aspect of these findings is that the configurations of these structures have been assigned $K \geq 3/2$. Notably, there are no parity doublets in even-even nuclei ($K$= 0). Similarly, there is no parity doublet in the $K$ = 1/2 yrast structure of $^{221}$Th (i.e., the parity doublet in this nucleus is "off-yrast"). In 1953, F. Stephens *et al* performed an experimental study of the $^{228}_{90}$Th$_{138}$ and $^{224}_{88}$Ra$_{136}$ nuclei. Level schemes were built and spins and parities were assigned to the energy levels [32]. The following year (1954), the same authors studied even-even nuclei of spin 1 and odd parity [33] on a specific region of the nuclear map. Those were the first observations of negative-parity states near ground states [34]. Since that time, abrupt breaking of the reflection symmetry has been associated to deformed nuclei with low-lying states of odd parity. BTW Stephens saw this in alpha decay [33].

Figure 3.1 summarizes the parity-doublet structures in the region relevant to this work. The structures are presented in terms of the relative energies, $E_r$, for the $^{219-225}$Th and $^{219,221}$Ra isotopes. The $^{223}$Th and $^{221}$Ra structures are particularly close to E$_{rel} \approx 0$. In $^{223}$Th and $^{221}$Ra one deals with $K = 5/2$ bands. No additional structures with $K = 1/2$ and $K = 3/2$ have been reported and are part of the justifications of the present work.

$$E_r = E_{I,s=+i} - E_{I,s=-i} \tag{3.1}$$

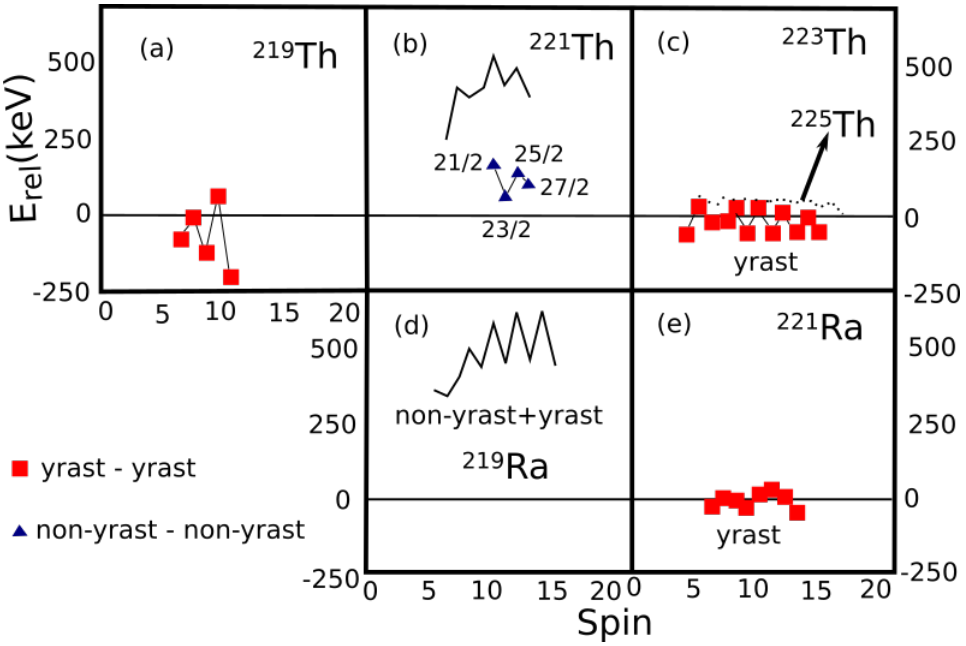


**Figure 3.1:** Relative energies $E_{rel}$ $=E_{I,s=+i}-E_{I,s=-i}$ for the $^{219-225}$Th [(a) to (c)] and $^{219,221}$Ra isotopes [(d) and (e)]. Yrast states are shown with squares and non-yrast states by triangles, and lines without symbols correspond to sets of yrast and non-yrast states. The $^{223}$Th and $^{221}$Ra bands have $E_{rel} \sim 0$. The yrast bands for $^{221}$Th and $^{219}$Ra are "special": no parity doublet ($K$=1/2). When $K$ is large, there is a tendency to form parity doublets. All the others bands are either $K$=3/2$\left(^{219}\text{Th}\right)$ or $K$=5/2, including the $^{221}$Th non-yrast structure. For additional information see ref. [8]

Multiple efforts lead to explain the parity splitting using nuclear models which include deformations of higher orders than quadrupole-deformation. The first surface octupole "deformations" (better described as vibrations) were introduced by Strutinsky in 1956 [35] where the possibility that some nuclei might have an asymmetric shape under reflection was discussed. Lee and Inglis considered the stability of the pear-deformation by a perturbation theory considering a constant volume condition, which establishes that nucleus' volume does not change despite deformation. [36]. The last study, made by Maquart *et al* [7] found a new non-yrast band without interlink with opposite simplex and they have interpreted this result as a dominant $K = 1/2$ contribution. In addition to the latter, an extension to the rotational $K = 5/2$ yrast band has been added concluding the existence

of a backbending from the interpretation of a band crossing. Maquart's study was analyzed with triple-gamma coincidence while this experiment was performed with the $\gamma-\gamma$ particle coincidence.

Three collective modes of octupole behaviour have been found in the actinide region: octupole surface vibration, static quadrupole and octupole deformations and octupole phonon excitations. Quadrupole waves running over the nuclear surface have been also discussed, however, for cases in another mass region of the nuclear chart [37]. For example, the $^{239}$Pu nucleus can be considered as an example for the surface-vibration mode (with an additional rotational band), see Ref. [38]. Studies of $^{224}$Th and $^{146}$Ba have shown that rotation of octupole-deformed nuclei lead to static octupole shape. An example for the octupole tidal wave is discussed in Ref. [39].There is a phase transition between vibration and quadrupole- octupole rotation. In 1995, Jolos and Brentano suggested that a common moment of inertia can be evidenced in levels of opposite parity at low spin. However, at higher spin, backbending effects could modify the inertia values [40].

The use of microscopic methods to study octupole deformations and intrinsic reflection asymmetric on nuclei is one of the challenges of present studies in nuclear structure theory. For example, properties of ground and excited states in several light actinides were studied by R. Chasman using theoretical wave functions of many-bodies [41, 42, 43]. Also, simulations by Hartree-Fock plus BCS[1] calculations have established the E1 and E3 transitions probabilities in $^{222}$Ra [44]. Additionally, P. Bonche calculated rotational bands in $^{194}$Pb with microscopic collective wave functions [45]

So called macroscopic-microscopic (or Nilsson-Strutinsky) methods are referenced in the Nazarewicz et al. studies: Woods-Saxon-Bogolyubov cranking calculation at high spin [46] and the cranking model with the Woods-Saxon average potential and pairing [47]. The review article of Ref [2], provides more literature dealing with the macroscopic-microscopic, Self-consistent, Algebraic, Boson and Cluster Models.

[1] Bardeen-Cooper-Schrieffer variational method

*Scientific views end in awe and mystery, lost at the edge in uncertainty, but they appear to be so deep and so impressive that the theory that it is all arranged as a stage for God to watch man's struggle for good and evil seems inadequate.*

Richard P. Feynman

CHAPTER

4

# Experimental Details and Analysis Methods

In the path to unveil the main quests for nuclear structure, the experimental use of high-resolution $\gamma$-ray detector arrays, in conjunction with charged-particle detectors, is the most outstanding and useful tools of the field. The develop of high precision detectors has allowed the opening of new techniques to study the nature of the nuclear interactions. In this section the experimental setup required to detect and correlate $\gamma$ rays and charged particles, using the GAMMASPHERE and the HERCULES array, and other simpler setups, and how this can be utilized to measure quantities such as magnetic moments and the building of level schemes. Nuclear magnetic moments, with the so called Transient Field Technique, will be presented. The use of $\alpha$-transfer reactions to populate nuclear excited states of short life-time will be also presented with some recent results obtained from an experiment made at the Lawrence Berkeley National Laboratory, USA, as part of the training to understand the system detection and the analysis on $\gamma$-ray spectroscopy.

## 4.1 Experimental Setup: GAMMASPHERE

GAMMASPHERE is an array of 110 n-type Ge detectors, each one feed with $\sim$2500 V and cool down with liquid nitrogen to keep the Ge crystal at low temperature. Fig. 4.1 shows the configuration of the system. In front of the BGO compton suppressor there is a shield

(Hevimet Sheld) that protects the scintillators from frontal $\gamma$ hitting and also to filter x-ray coming from internal excitations of the nuclei. Each HPGe has its own Dewar and detection electronic system. All details of the system are found in Ref [3]. Fig. 4.2 exhibit the full setup with all detectors. The goal is to cover $4\pi$ solid angle and to detect $\gamma$-rays at higher efficiency. The target is at the center of the sphere and the Hercules system is behind the target to measure the heavy sub-products of the reaction.

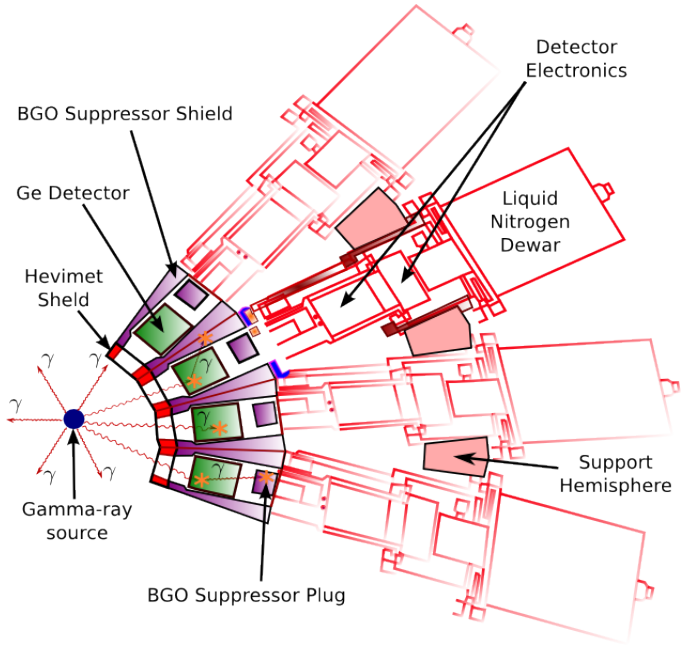


**Figure 4.1:** GAMMASPHERE is composed with 110 HPGe detectors rounded with BGO. Germanium detectors are feed with $\sim$ 2500 Volts and cool down around 77 Kelvin degrees.

## 4.2 Detectors

### 4.2.1 Hyper-pure Germanium detector: HPGe

The resolution of hyper-pure Germanium (HPGe) detector at 1.33 MeV is $\sim$2 keV. The difficulty to grow big crystal of Germanium is one of the reasons for the low efficiency of the photopeaks. It would be necessary to increase the volume of the detector and it is not desirable because the increment of the Compton Effect [48, 49]. To reduce the Compton effect the use of fast **BGO** detector is implemented.

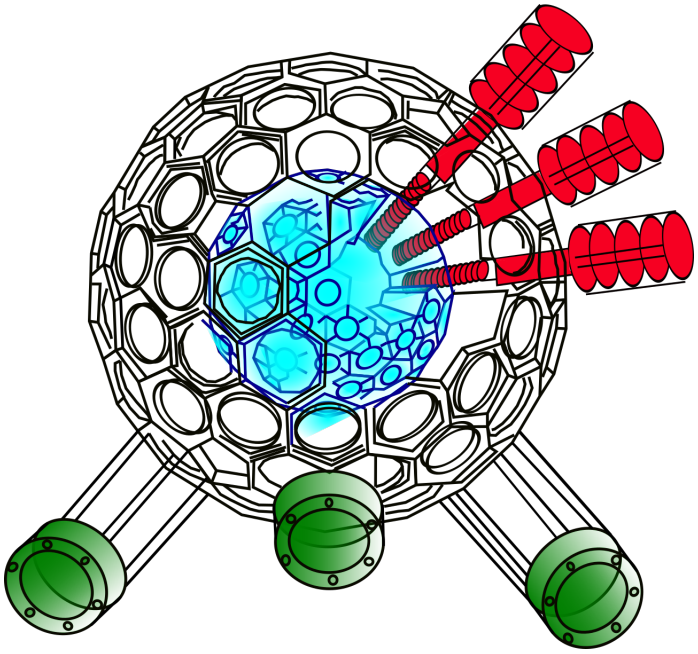

**Figure 4.2:** GAMMASPHERE is a $4\pi$ array of n-type detector resistant to neutron damage, high energy resolution and an achievement of the efficiency and good response function [3].

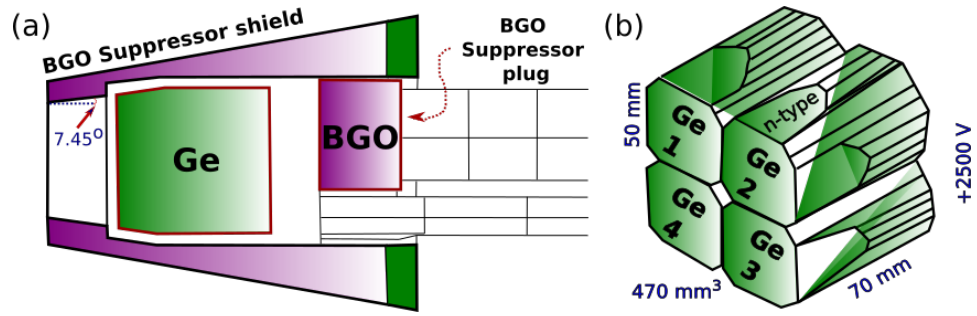


**Figure 4.3:** (a) Germanium detector surrounded with BGO scintillator useful as Compton suppressor and neutron shield. HPGe has an energy resolution $\sim$2.5 keV at 1.33 MeV. (b) A clover is composed by four HPGe detectors. It is has been useful for data acquisition to measure nuclear magnetic moments of excited states of short life-time.

### 4.2.2 BGO Scintillator

A BGO detector is a crystal composed of Bismuth (Z=83), Germanium (Z=32) and Oxygen (Z=8). Because the high atomic number and high density, Bismuth Germanate Oxide ($Bi_4Ge_3O_{12}$) can be utilized as a Compton Suppressor. The Compton Radiation at low energies is unwanted for $\gamma$-ray spectroscopy of high resolution. The scattered $\gamma$-rays from the Compton effect can be absorbed by a suppressor such as the BGO which is an efficient $\gamma$-ray absorber. Also, the BGO is a shield that protects the HPGe from the neutron damage. Fig. 4.3-(a) shows the configuration of a single detector with BGO Compton suppressors.

### 4.2.3 HERCULES.

HERCULES is an array of 64 plastic scintillators distributed in 4 rings. On the first ring there are eight detectors, on the second one, 14 detectors; on the third ring, 14 detectors and on the fourth one, 24 detectors (see Fig. 4.4). HERCULES is designed to detect the heavy recoil sub-products of the reaction. The three prime characteristics of Hercules are: (a) a large solid-angle coverage. Then, the covered angle range from $5^o$ to $19^o$ degrees with time resolution less of one pico-second. (b) High segmentation Plastic scintillators which enable one to perform time-of-flight measurement at a short distance to conserve the large solid-angle coverage. (c) High-count rate capability to be able to take scattered particles and compatible with 110 HPGe detectors [4].

## 4.3 Nuclear Reactions

### 4.3.1 Alpha Transfer reaction.

As part of the understanding in the $\gamma$-ray spectroscopy analysis, an experiment was performed at the Lawrence Berkeley National laboratory in may 2015. Using alpha transfer reaction in combination with the Transient Field Technique, excited states of $^{110}$Sn were populated and their nuclear magnetic moments were measured. One advantage of the use of alpha transfer reactions is the close reaction energy to the Coulomb barrier. In the same experiment, the life-time of the lowest excited spin states of $^{106}$Cd were measured for the first time. Fig. 4.7 summarizes the main details of the Alpha Transfer reaction and Coulomb excitation. On the other hand, the Transient Field Technique is an experimental tool to measure the precession of the angular distribution of radiation of short life-time spin states, due the magnetic interaction between the spin and an strong magnetic transient field

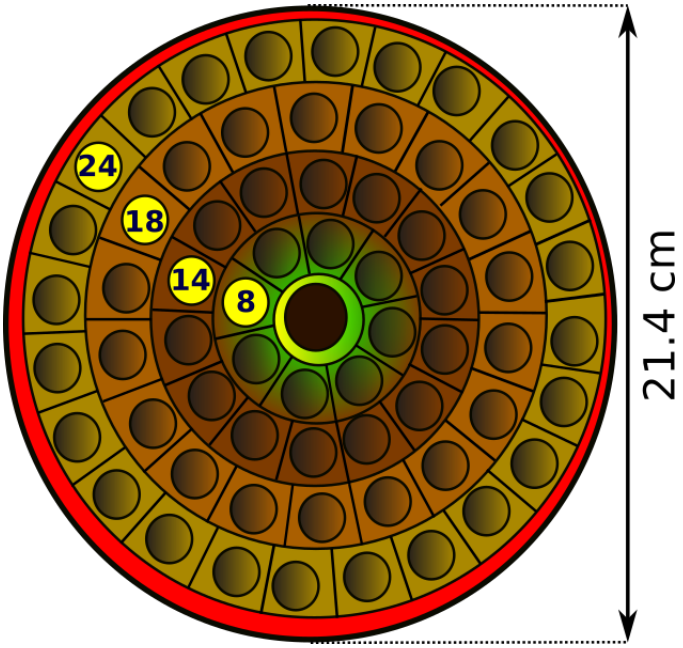


**Figure 4.4:** The $\gamma - \gamma$-rays are measured in coincidence with the heavy sub-product of the reaction. Hercules is a set of 64 detectors distributed on four concentric rings. This disk is behind of the target at 20 cm and covering 5.6% of the total solid angle.

of hyperfine origin. All details of the Transient Field and its parametrizations are described in ref [50].

The nuclear $g$ factor is defined as the ratio between the nuclear magnetic moment, $\mu_{\mathrm{nuclear}}$, to the nuclear spin, $\mathrm{I}_{\mathrm{nuclear}}$, for a given state.

$$\mathrm{g} = \frac{\mu_{\mathrm{nuclear}}}{\mathrm{I}_{\mathrm{nuclear}}} \tag{4.1}$$

- Nuclear magnetic moments, $\mu$, appear because there are internal currents in the nuclei originated by charged protons.
- Intrinsic magnetic moments due to the proton and neutron spins also contribute with the total magnetic moment of nuclei.
- The opposite sign in the intrinsic g factor for protons and neutrons allow us to distinguish which is the main particle contribution to the nuclear wave function:

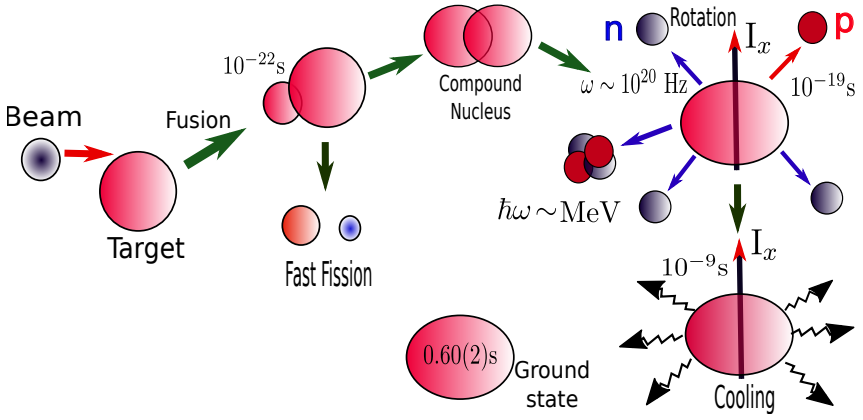


**Figure 4.5:** A sketched vision about the mechanism of the Fusion evaporation reaction. There are several channels in the reaction: fragmentation, direct break up, Coulomb excitation, nucleon transfer and fusion evaporation. A heavy compound nucleus is produced with a large amount of energy, then the system tend to minimum energy state. In that way, alpha particles, protons and neutrons are emitted and the $^{223}$Th is produced in its own highly excited states. An amount of $\gamma$ rays are emitted by the excited nucleus along the way from the highest state spin to the ground state. The rapid rotation allow the break up of independent particles and there is a competition between the collectives and independet particles properties. Transitions $E$-type are sensitive to charge distribution and collective behavior, and transitions M-type are sensitive to current densities into the nucleus.

$$\mathrm{g}_\pi = +5.5858 \text{ and } \mathrm{g}_\nu = -3.8263$$

$\mu_{nuclear}$ will precess an angle $\Delta\theta$ under the influence of a Transient Magnetic Field $\mathrm{B_{TF}}$. The measuring of $\Delta\theta$ provides a model independent value of g,

$$\Delta\theta = -\mathrm{g}\left(\frac{\mu_\mathrm{N}}{\hbar}\right)\int_0^\mathrm{t} \mathbf{B}[\mathrm{v(t)}]\mathrm{e}^{-\mathrm{t}/\tau}\mathrm{dt} \tag{4.2}$$

- The Coulex and alpha-transfer reactions exhibit different spin alignments and hence different correlations W($\theta$) [51]. Coulex excitation studies yield a pronounced angular correlation of the gamma-decay with respect to the beam direction [52]. Spin alignment is better in Coulex than in the alpha-transfer reactions.

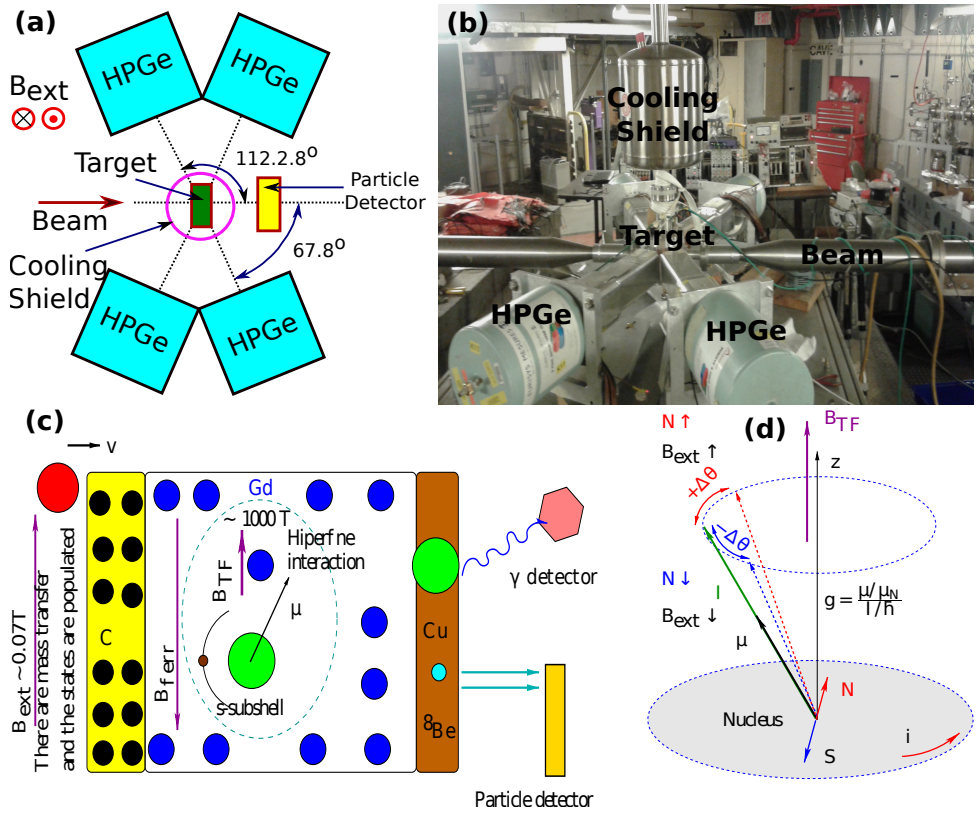


**Figure 4.6:** (a) Each square represents a clover detector composed with four HPGe crystal. The target is at the center and the particle detector is located behind the target. $67.8^o$ is the angle of largest variation of the angular distribution of the radiation. (b) Facilities at the Lawrence Berkeley National Laboratory. In the picture the beam-line, the Cooling Shield and the dewars of the HPGe can be seen. (c) The isotope interact with a first carbon layer and an alpha particle of the carbon is transfered to the ion. The bar ion travel through a ferromagnetic material which is aligned by an external magnetic field. The only electron in the $s$ sub-shell of the ion establishes an hyperfine interaction because of the ferromagnet, and then, the magnetic moment can be aligned. (d) The variation of the external magnetic field allows to measure a variation of the angular distribution of the radiation and then, the angle $\theta$ can be obtained with a resolution of mrad.

- The alpha transfer reaction is shown to be an important alternative to the spectroscopy of low-intensity radioactive beams [53], specially for neutron deficient beams [54].

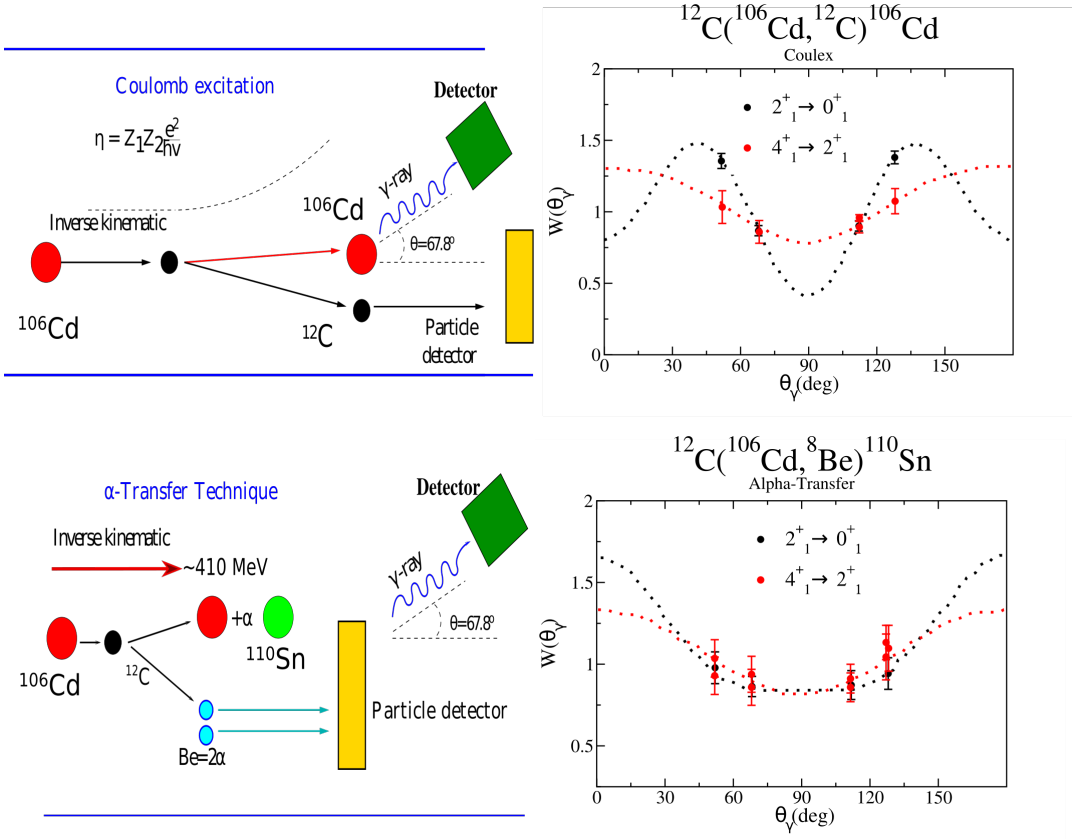


**Figure 4.7:** The energy to produce Alpha transfer reaction is close to Coulomb barrier. In this experiment beam energies of 390, 400, and 410 MeV were employed to find the best $\alpha$-transfer yield [5] in combination with Transient Field Technique. The nuclear magnetic moments and life-time of the low lying spin states were measured. Coulomb excitation reaction were useful to measure the life-time of the first excited states of $^{106}$Cd [6]

- The spin alignment and the relative role of direct population increase slightly with the excitation-energy [55, 56, 57].

Magnetic and electric moments are useful to study nuclear properties because multipole moments are sensitive to nuclear magnetic moments, single particles properties, charge distributions and deformation.

### 4.3.2 Fusion-evaporation reaction.

The experimental method for fusion-evaporation reaction is similar to the alpha-transfer, but in this case 110 detectors are utilized to cover $4\pi$ strad and the silicon detector is replaced by Hercules system detection. If the energy of the reaction is above of the Coulomb barrier a fusion-evaporation reaction is produced. The compound nucleus have an excess of energy and it will tend to the minimum energy state. For that, protons, neutrons and alpha particles are evaporated until the nucleus keep only the energy for the excitation of the populated states. The highest states are firstly populated and a cascade of transitions produces the populating of the lowest states after the evaporation process [58]. The possible channels of the fusion-evaporation process say us which can be the possible contaminants of the reaction. The spectra of those sub-products must be subtracted from the main one dimensional spectrum.

In this study, beams of $^{18}$O at an energy of 80-86 MeV from the ATLAS superconducting linear accelerator at Argonne National Laboratory, bombarded a target consisting of 0.28-0.36 mg/cm$^2$ layer of $^{209}$Pb, supported on a carbon substrate of 0.008 mg/cm$^2$. Gamma rays were detected with GAMMASPHERE array plus HERCULES detector combination. High-spin sates in $^{223}$Th were populated with the so-called Fusion-Evaporation Technique.

The $\gamma$-$\gamma$ coincidences were stored in a two dimensional histogram so-called *coincidence matrix* (Fig. 4.8-(a)). The number of counts in each ($x$,$y$) channel of the matrix indicates how many pairs of $\gamma$-rays with energies $\left(E_{\gamma_x}; E_{\gamma_y}\right)$ have been detected. Summing all counts of all channels in $y$-axis for each $x$-channel, a spectrum over the $x$ direction is obtained. After that, narrow windows (gates) can be established around a $y$ channel and its projection on $x$ axis shows the one dimensional coincidence $\gamma$-ray spectrum (Fig. 4.8-(b)). If a set of channels on $y$ axis is selected, a peak will appear on the total spectrum. The spectrum tell us what other $\gamma$-ray the peak is in coincidence with. Examining appropriate models and precedents spectra, the orders of the transitions can be ordered using **escl8r** program.

The intensities must be fitted because *The sum of all decays into an excited state of a nucleus must equal the number of decays out of the same energy level.* On the other hand, *the background in the matrix consists of Compton scattered events. Such events occur when one or both of the $\gamma$-rays deposited less than their total energy in the detectors. This background has to be correctly subtracted for each gated $\gamma$-ray spectrum* [59].

The one dimensional spectrum does not contain information about the order of the $\gamma$-ray in each cascade, for which, the sort of all transitions must be analyzed calculating intensities

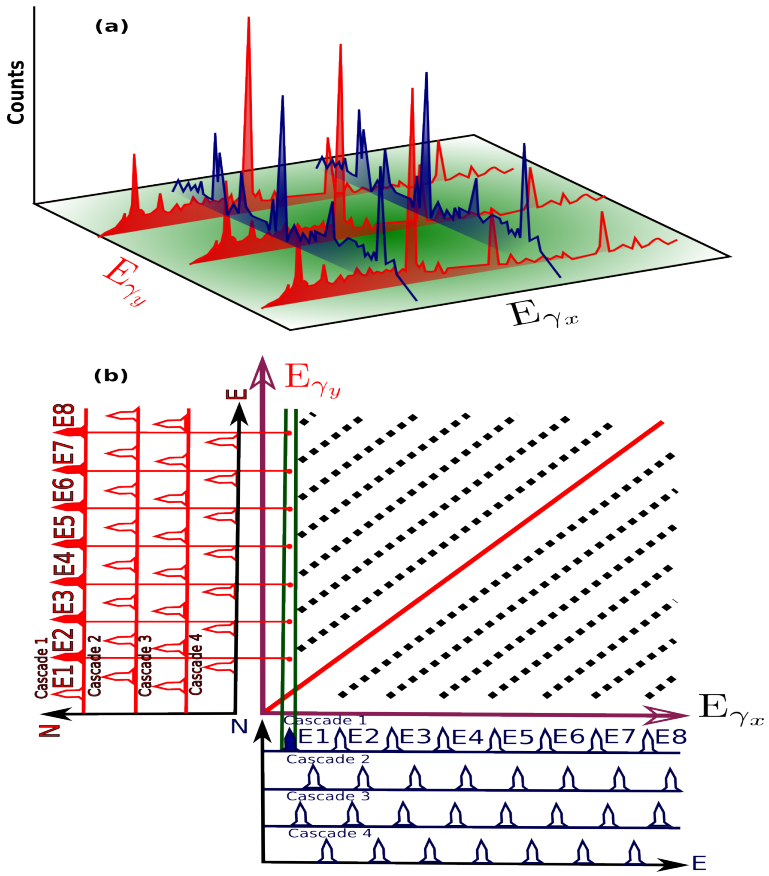


**Figure 4.8:** (a) Matrix build from the $\gamma$-$\gamma$ coincidences. Each event is the detection of two $\gamma$-rays, the first is absorbed by $E_y$ detector and the second one, by $E_x$ detector. (b) The green line represents a narrow window of 5 channels which shows all coincidences. One-dimensional spectrum is calculated by the summing of all channels of $y$-axis for each $x$-axis.

and seeing coincidences. The analysis of the one-dimensional spectrum (total projection of the coincidence $\gamma$-ray matrix over $x$-axis) leads to the building of the $^{223}$Th level schemes, which could tell us about the nature of the rotational bands, and so, the deformation of the nuclear mean field. The E1, E2 and M1 transitions, spin, signature and associated parities can be measured by the analysis of the experimental results.

The cascade of $\gamma$-rays emitted from the highest excited spin state to the ground state are stored in a *matrix.mat* file which registers the detection of the radiation through 4096 channels. The **.mat* format is an coordinates array of 4096 by 4096 where each point is one

$\gamma$-$\gamma$ coincidence event ($E_{\gamma_x}$,$\gamma_y$). The following steps are previous to have already the total projection spectrum for the analysis and construction of the level scheme.

1. Project all channels of $y$-axis per each $x$-channel. This process is known as *slicing* for which the matrix is projected over one-dimensional spectrum.

2. *matrix.mat* file is load with gf3 which is a program belonging to the RADWARE Suite. The output is a file with extension *.esc* extension. This file contain a reduced matrix of 2048 by 2048 channels. gf3 ask the following inputs: Calibration file (.aca), projection over $x$-axis and background subtraction (.spe).

Once the one dimensional spectrum has been generated, the analysis can be begun.

*The history of science shows that theories are perishable. With every new truth that is revealed we get a better understanding of Nature and our conceptions and views are modified.*

Nikola Tesla

CHAPTER

# 5

# Results

## 5.1 Level schemes

In this section the level schemes for $^{220}_{88}$Ra, $^{224}_{90}$Th and $^{223}_{90}$Th will be presented, being the last one the isotope of interest in this study. The level schemes for $^{220}_{88}$Ra and $^{224}_{90}$Th have been completely built from the total projection spectrum and them are consistent with the chart of nuclides of the National Nuclear Data Center [60, 61], providing us trustfulness in the construction of the $^{223}_{90}$Th level scheme.

The nuclear reaction follows several possible channels and undesirable $\gamma$ rays rise up from the such called reaction contaminants (See Tab. 5.1). New $\gamma$ rays were analyzed to determine if the emission could be come from undesirable sub-products of the reaction. If a new $\gamma$ ray does not belong to one of the contaminants, this would be considered to be part of the $^{223}_{90}$Th level scheme. In this analysis characteristics $\gamma$ rays of $^{224}_{90}$Th and $^{220}_{88}$Ra were detected, and Fig. 5.1 shows their corresponding level schemes, which have been inferred from balance and intensity coincidences.

### 5.1.1 Level Schemes of the contaminants

The spectra for $^{220}_{88}$Ra and $^{224}_{90}$Th are consistent with level schemes reported in the National Nuclear Data Center citenndc-220Ra, nndc-224Th. Two new crossover transitions have been proposed in this work for the contaminants: In the $^{220}_{88}$Ra level scheme the 53.1-keV, $6^+ \rightarrow 5^-$, transition is proposed for the first time here. With the inclusion of this

**Table 5.1:** Sub-products of the reaction ${}^{18}_{8}\mathrm{O}_{10} + {}^{208}_{82}\mathrm{Pb}_{126}$ at 85 MeV. The bold text indicates the sub-products detected from this reaction. The level schemes for ${}^{220}_{88}$Ra, ${}^{224}_{90}$Th and ${}^{223}_{90}$Th were build completely from the experimental data.

$$
{}^{18}_{8}\mathrm{O}_{10} + {}^{208}_{82}\mathrm{Pb}_{126} \rightarrow \begin{cases} {}^{224}_{89}\mathrm{Ac}_{135} + 1\mathrm{p} + 1\mathrm{n} & Decay\ radiation : \alpha \\ {}^{223}_{89}\mathrm{Ac}_{134} + 1\mathrm{p} + 2\mathrm{n} & Decay\ radiation : \alpha \\ \mathbf{{}^{223}_{90}Th_{133} + 3n} & Decay\ radiation : \alpha \\ \mathbf{{}^{224}_{90}Th_{134} + 2n} & Decay\ radiation : \alpha,\ \beta^{-} \\ \mathbf{{}^{220}_{88}Ra_{132} + \alpha + 2n} & Decay\ radiation : \alpha \\ {}^{219}_{88}\mathrm{Ra}_{131} + 1\alpha + 3\mathrm{n} & Decay\ radiation : \alpha \\ {}^{221}_{88}\mathrm{Ra}_{133} + 1\alpha + 1\mathrm{n} & Decay\ radiation : \alpha \end{cases}
$$

transition, the coincidence of the 313.0-keV, $8^{+} \rightarrow 6^{+}$, and the 184.9-keV, $7^{-} \rightarrow 6^{+}$, can be explained when a gate is made on the 224.6-keV, $5^{-} \rightarrow 4^{+}$ $\gamma$-ray transition. Without the presence of the 53.1-keV, $6^{+} \rightarrow 5^{-}$, transition the coincidences presented here will not be possible to observe. See upper part of Fig. 5.2

For ${}^{224}_{90}$Th a $\gamma$-ray transition of 70.2-keV, $6^{+} \rightarrow 5^{-}$, is proposed for the first time here. This transition allows to understand the coincidences between the 180.4-keV, $5^{-} \rightarrow 4^{+}$, transition with the transitions in the upper band (See the lower part of Fig. 5.2). Transitions with energies lower than 80 keV have been missed because the hevimet shield located in front of the germanium detector. The hevimet is useful to filter the x-ray coming from the internal electronic shells.

### 5.1.2 ${}^{223}_{90}$Th Level Scheme

The proposed level scheme for ${}^{223}_{90}$Th is presented in Fig. 5.5. A recent publication on ${}^{223}_{90}$Th is presented in Ref. [7]. A comparison with this work will be presented later on. The spin of

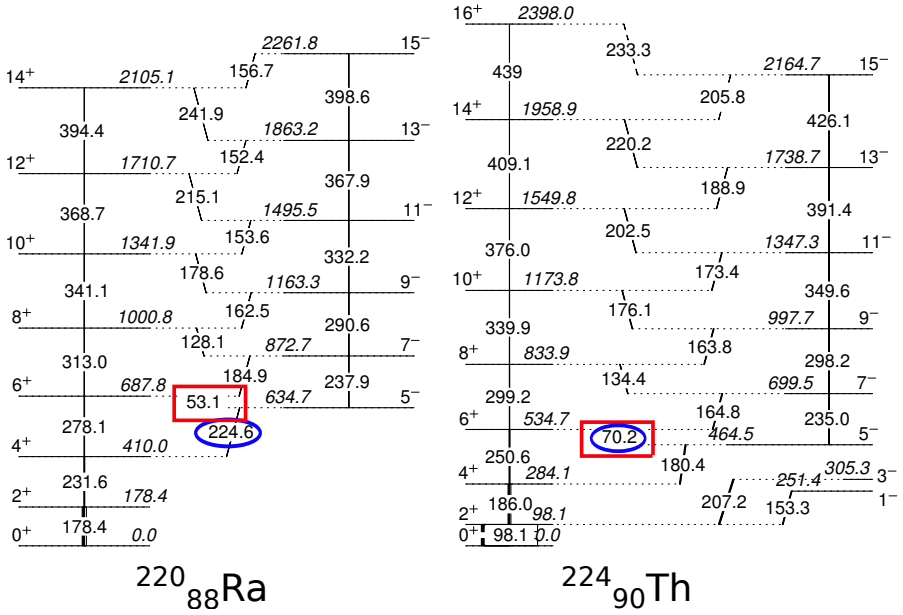


**Figure 5.1:** Level scheme for $^{220}_{88}$Ra and $^{224}_{90}$Th. Red boxes: new transitions. Blue circles: Transitions gated. The 53.1-keV, $6^+ \rightarrow 5^-$, and the 70.2-keV, $6^+ \rightarrow 5^-$, transitions have been seen in this work for first time. Fig. 5.2 shows how the highest states of the $^{220}_{88}$Ra are communicated with the 224.6-keV, $5^- \rightarrow 4^+$, transition through 53.1-keV, $6^+ \rightarrow 5^-$, transition. In the same way, the upper states of $^{224}_{90}$Th are communicated with 180.4-keV, $5^+ \rightarrow 4^-$, transition by 70.2-keV, $6^+ \rightarrow 5^-$, transition. The 180.4-keV, $5^- \rightarrow 4^+$, transition is in coincidence with the 207.2-keV, $3^- \rightarrow 2^+$, and the 153.3-keV, $1^- \rightarrow 2^+$, transitions.

the ground state is to be $5/2^+$ and this is the band head of the yrast band by definition [8]. Inside the coloured boxes the new results from this work are presented. 26 new $\gamma$-ray transitions and 17 new energy levels are reported, tentative assignment for spin and parity of the states are given by the systematic from previos results. The largest observed spin state for this work is $37/2^-$ at a $E_x = 2415$ keV, upper states are not observed due to the experimental setup that needs the detection of the recoil sub-products in the HERCULES array, thus, only recoil sub-products with enough kinetic energy will reach and excite the scintillators of HERCULES, leaving less internal energy to excite the upper states of the recoil nuclei. Ref. [7] used a tick target experiment that allows the use of $\gamma - \gamma - \gamma$ coincidences in a set of sub products, while in the case of this work a better discrimination of $^{223}$Th is obtained.

A first evidence of parity doublets can be seen in the 223.2-keV, $17/2^- \rightarrow 13/2^-$, $\gamma$-ray transition and the 249.5-keV, $17/2^+ \rightarrow 13/2^+$, $\gamma$-ray transition. The energy levels at $E_x = 323.8$ keV, $13/2^-$, keV and at $E_x = 319.2$ keV, $13/2^+$, respectively, are nearly degenerate states with opposite parity (it is worth to remember that for case of a perfect parity doublet the energy has to be the same). The new $\gamma$-ray transition 146.6-keV, $15/2^{(-)} \rightarrow 13/2^-$, in the b8 band identified in this work presents evidence of a new parity doublet, between the states at $E_x = 469.6$ keV, $15/2^{(-)}$ (b8 band), and at $E_x = 466.5$ keV, $15/2^+$ (b5-a band), firstly reported here, the high possible $M1$ character of the $\gamma$-ray transition 146.6-keV, $15/2^{\pm} \rightarrow 13/2^{\pm}$ in the b8 and the b5-a structures, confirm this affirmation, and then, a like-pear structure is confirmed in the medium spin structure. The difference on energy is less than the first parity double. Fig. 5.3 shows the presence of the 146.6-keV, $15/2^- \rightarrow 13/2^-$, $\gamma$-ray transition that connects the b8 and GS-b4 bands. The spectrum gated by 146.6-keV, $15/2^- \rightarrow 13/2^-$, $\gamma$-ray transition shows the coincidences with the 111.6-keV, $13/2^- \rightarrow 11/2^+$; the 129.3-keV, $11/2^+ \rightarrow 9/2^-$; the 131.7-keV, $21/2^- \rightarrow 19/2^+$ and with the 159.2-keV, $19/2^+ \rightarrow 17/2^-$, $\gamma$-ray transitions between the GS-b4 and the GS-b3 bands. On the other hand, the 146.6-keV, $15/2^+ \rightarrow 13/2^+$, $\gamma$-ray transition is coincident with the 200.9-keV, $13/2^+ \rightarrow 9/2^+$, $\gamma$-ray transition in the GS-b1 band and with the 124.1-keV, $11/2^- \rightarrow 9/2^+$, transition that connect the GS-b2 and GS-b1 bands. The $\gamma$-ray transition 77.7-keV, $17/2^- \rightarrow 15/2^-$ in the GS-b4 band, which is a doublet with the $\gamma$-ray transition 76.8-keV, $13/2^+ \rightarrow 11/2^-$ in the GS-b2 band, is coincident with the 159.2-keV, $19/2^+ \rightarrow 17/2^-$, $\gamma$-ray transition.

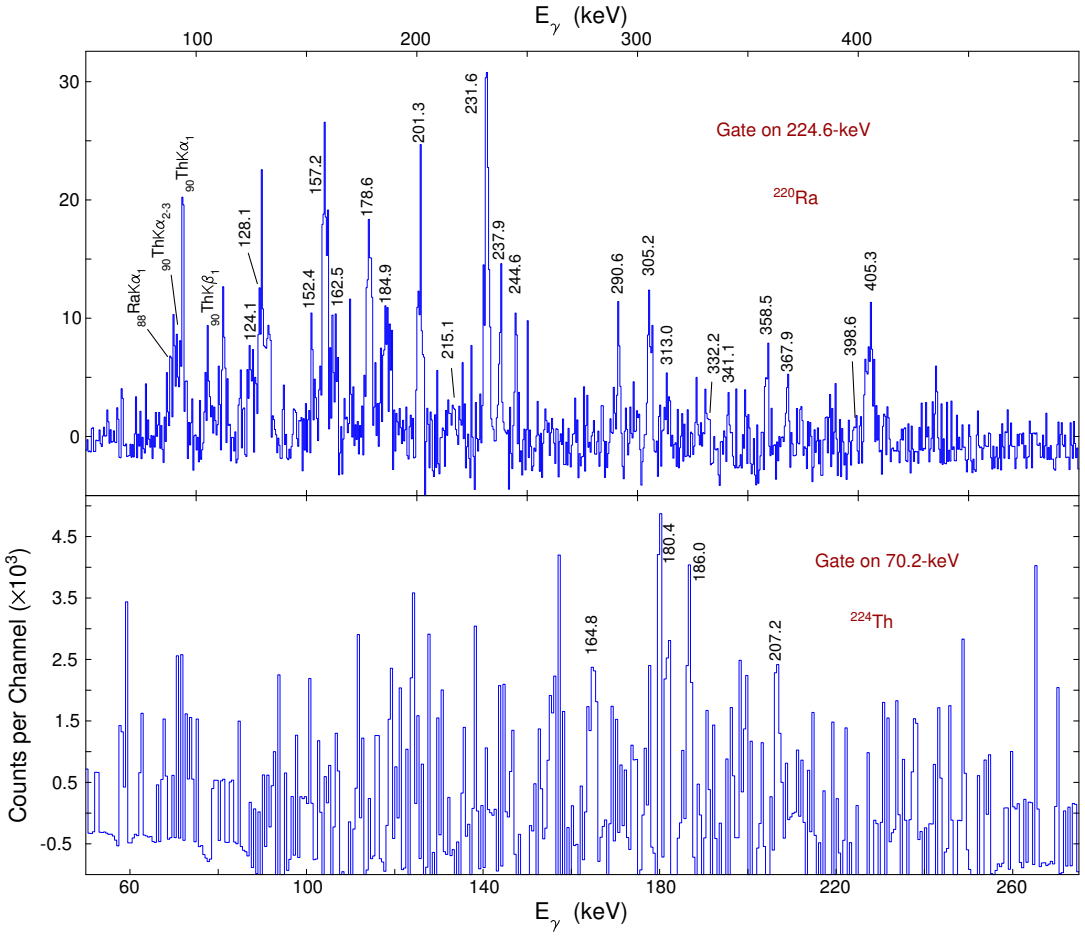


**Figure 5.2:** Upper: Gate on the 224.6-keV, $5^- \rightarrow 4^+$, transition. The 53.1-keV, $6^+ \rightarrow 5^-$, transition connects the 224.6-keV, $5^- \rightarrow 4^+$, transition with the 313.0-keV, $8^+ \rightarrow 6^+$ and 341.1-keV, $10^+ \rightarrow 8^+$, transitions. $E1$ cross transitions are in coincidence with 224.6-keV, $5^- \rightarrow 4^+$, too. Lower: Gate on the 70.2-keV, $6^+ \rightarrow 5^-$, transition which is in coincidence with the 164.8-keV, $7^- \rightarrow 6^+$; with the 180.4-keV, $5^- \rightarrow 4^+$, and with the 186.0-keV, $4^+ \rightarrow 2^+$, transitions.

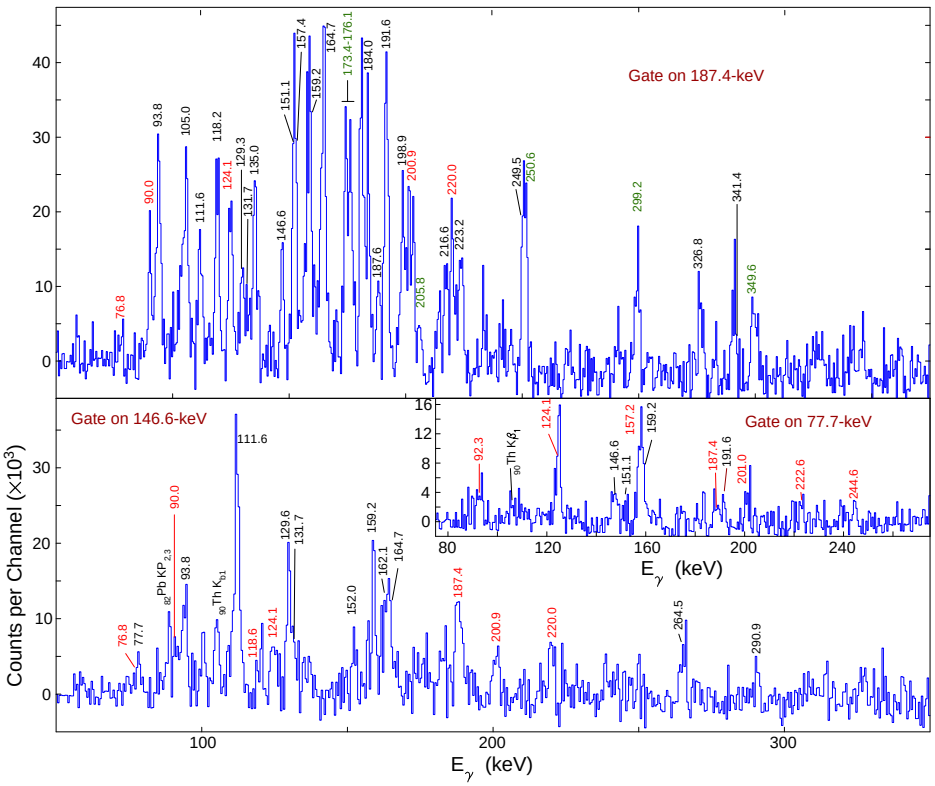


**Figure 5.3:** Lower: Spectrum gated on 146.6-keV, $(15/2^{\pm} \rightarrow 13/2^{\pm})$, transition. The black labels correspond to the coincidences with the transition that connects the b8 band with the GS-b4 band. The red labels are the coincidences located in the GS-b1 band. Energy levels at $E_x = 469.6$ keV $(15/2^{-})$ and at $E_x = 466.5$ keV $(15/2^{+})$ exhibit a doublet parity. These spin states are nearly degenerates belonging to non-yrast structures. The 77.7-keV, $17/2^{-} \rightarrow 15/2^{(-)}$, the 152.0-keV $19/2^{(-)} \rightarrow 15/2^{(-)}$ and the 264.5-keV, $23/2^{(-)} \rightarrow 19/2^{(-)}$ transitions, have been built from intensity balance. Lower-right: The 77.7-keV, $17/2^{-} \rightarrow 15/2^{(-)}$ and the 76.8-keV, $13/2^{+} \rightarrow 11/2^{-}$, transitions are in coincidence with the 159.2-keV, $19/2^{+} \rightarrow 17/2^{-}$ and the 124.1-keV, $11/2^{-} \rightarrow 9/2^{+}$ transitions respectively. The 187.3-keV, $29/2^{-} \rightarrow 27/2^{+}$, transition is self-coincident showing that the 186.6-keV, $27/2^{+}$[GS-b3] $\rightarrow 25/2^{+}$[GS-b1] transition is a crossover that connect with the 326.1-KeV, $25/2^{+} \rightarrow 21/2^{+}$, transition. On the other hand, the 146.6-KeV, $15/2^{+} \rightarrow 13/2^{+}$, $\gamma$-ray transition is in coincidence with the 187.4-keV $(17/2^{-} \rightarrow 15/2^{+})$ transition in the b5-a band. The coincidences of these transitions are marked in fig 5.4.

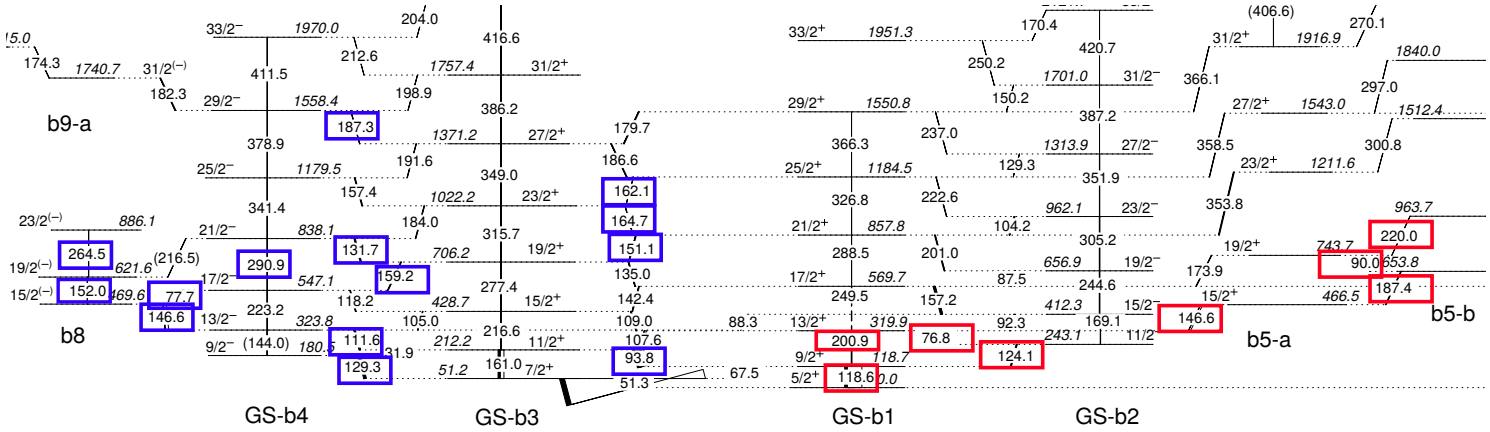


**Figure 5.4:** Red box: Transitions in coincidence with the 146.6-keV, $15/2^+ \rightarrow 13/2^+$, transition. Blue box: Transitions in coincidence with the 146.6-keV, $15/2^{(-)} \rightarrow 13/2^-$, transition.

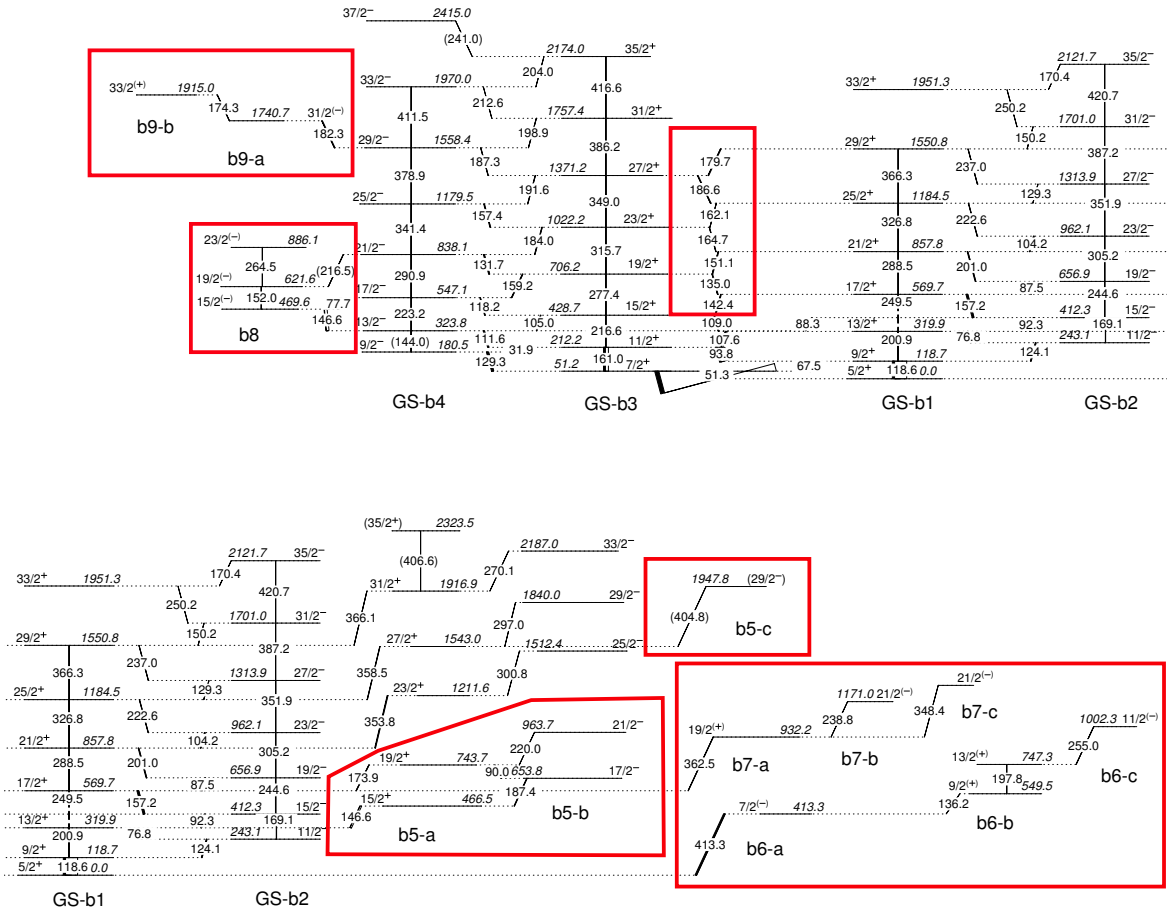


**Figure 5.5:** Level scheme for $^{223}_{90}$Th. The red boxes enclose the 26 new transitions and 17 new energy levels found in this work.

The 187.4-keV, $29/2^-$[GS-b4] $\rightarrow$ $27/2^+$[GS-b3], has a doublet with the 187.4-keV, $17/2^-$[b5-b] $\rightarrow$ $15/2^+$[b5-a], is also a contaminant present on $^{220}_{88}$Ra, $7^- \rightarrow 6^+$ . The gated spectrum in 187.4 keV, $17/2^- \rightarrow 15/2^+$, is presented in the upper part of Fig. 5.3 and it exhibits the $\gamma$-ray coincidences where it is easy to identify the $\gamma$ rays that belongs to the $^{223}$Th and $^{220}$Ra. The 187.4-keV, $17/2^- \rightarrow 15/2^+$, is in coincidence with the 146.6-keV, $15/2^+ \rightarrow 13/2^+$; the 200.9-keV, $13/2^+ \rightarrow 9/2^+$; and with the 124.1-keV, $11/2^- \rightarrow 9/2^+$, $\gamma$-ray transitions. The transition between GS-b4, $29/2^-$, and GS-b3, $27/2^+$ has been confirmed according to the reported in the literature [7, 21, 62].

New $M1$ crossover transitions have been seen between GS-b3 and GS-b1 bands: The 151.1-keV, $21/2^+ \rightarrow 19/2^+$; the 164.7-keV, $23/2^+ \rightarrow 21/2^+$; 162.1-keV, $25/2^+ \rightarrow 23/2^+$; the 186.6-keV; $27/2^+ \rightarrow 25/2^+$ and the 179.7-keV, $29/2^+ \rightarrow 27/2^+$, transitions. The $\gamma$-ray transitions, 142.4-keV, $17^+ \rightarrow 15/2^+$ and the 135.0-keV, $19/2^+ \rightarrow 17/2^+$, which were reported as tentative $\gamma$-ray transitions, 140.9-keV and 136.0-keV respectively, by Dahlinger [21, 62] have been confirmed here. Also, the 353.8-keV, $23/2^+ \rightarrow 21/2^+$, the 358.5, $27/2^+ \rightarrow 25/2^+$ and the 366.1-keV, $31/2^+ \rightarrow 29/2^+$, in the b5-a structure are transitions which have been reported in the Maquart's work [7]. The b5 structure presents two additional crossover transitions which were not reported by the Maquart's work: The first, the 146.6-keV, $15/2^+ \rightarrow 13/2^+$, transition is in coincidence with the 187.4-keV, $17/2^- \rightarrow 15/2^+$, transition. The second one, the 173.9-keV, $19/2^+ \rightarrow 17/2^+$, transition is in coincidence with the 220.0-keV, $21/2^- \rightarrow 19/2^+$, $\gamma$-ray transition. In addition the $E2$-type transitions reported by Maquart, the 373-keV, $31/2^+ \rightarrow 27/2^+$, and the 331-keV, $27/2^+ \rightarrow 23/2^+$, transitions have not been seen in this data analysis. The 406.6-keV, $35/2^+ \rightarrow 31/2^+$ transition is a tentative $\gamma$ ray in the Maquart's level scheme. The 404.8-keV, $(29/2^-) \rightarrow 27/2^+$ and the 358.5-keV, $27/2^+ \rightarrow 25/2^+$ transitions are in coincidence with the 222.6-keV, $25/2^+ \rightarrow 2/2^-$, transition, it leads us to propose the existence of the 406.6-keV $(29/2^-$[b5-c] $\rightarrow 27/2^+$[b5-a]) transition in the b5-c structure. possible.

The lower fig. 5.6 shows the gate at the 173.9-keV, $19/2^+ \rightarrow 17/2^+$, transition. The red labels in the spectrum are the coincidences belonging to the $^{224}_{90}$Th contaminant. The black labels are the coincidences belonging to the b5-b and GS-b1 bands of the $^{223}_{90}$Th level scheme. It can be seen that the 173.9-keV, $19/2^+ \rightarrow 17/2^+$, transition is in coincidence with the 220.0-keV, $21/2^- \rightarrow 19/2^+$ and the 249.5-keV, $17/2^+ \rightarrow 13/2^+$ transitions. The 157.2-keV, $17/2^+ \rightarrow 15/2^-$; the 249.5-keV, $17/2^+ \rightarrow 13/2^+$; the 220.0-keV, $21/2^- \rightarrow 19/2^+$; the 76.8-keV, $13/2^+ \rightarrow 11/2^-$; the 124.1-keV, $11/2^- \rightarrow 9/2^+$ and the 118.6-keV, $9/2^+ \rightarrow 15/2^+$ transitions are in coincidence with 173.9-keV, $19/2^+ \rightarrow 17/2^+$, transition. The 353.8-keV, $23/2^+$[b5-a] $\rightarrow 21/2^+$[GS-b1], transition is in coincidence with the 300.8-keV, $25/2^-$[b5-b] $\rightarrow 23/2^+$[b5-a], this also appear in the Maquart's work [7].

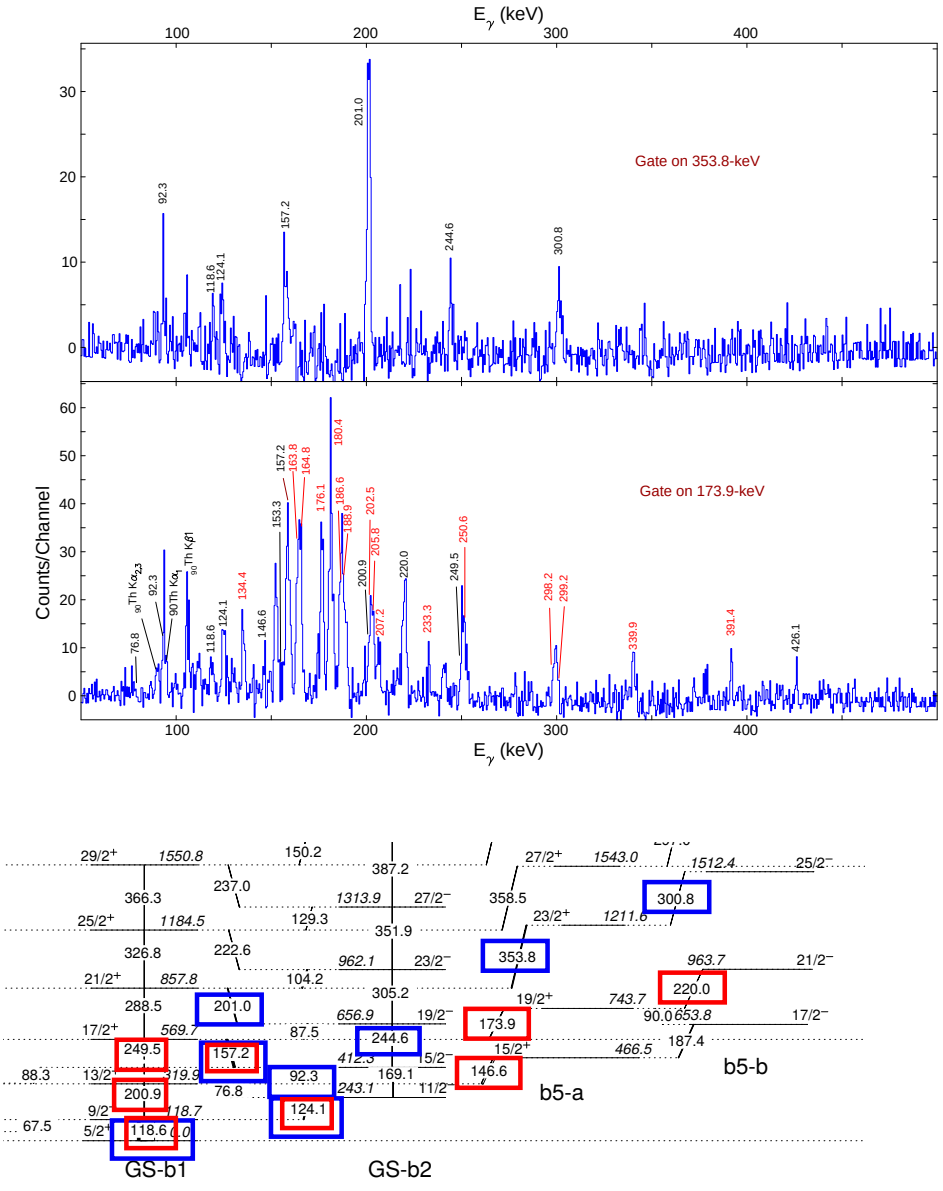


**Figure 5.6:** Upper: Coincidences with the 173.9-keV, $19/2^+ \rightarrow 17/2^+$, and on the 353.8-keV, $23/2^+ \rightarrow 21/2^+$, transitions. Lower: Level scheme showing the gated transitions on the spectra. Red box: $\gamma$ rays in coincidece with the 173.9-keV, $19/2^+ \rightarrow 17/2^+$, $\gamma$-ray transition. Blue box: $\gamma$ rays in coincidence with the 353.8-keV, $23/2^+ \rightarrow 21/2^+$, transition.

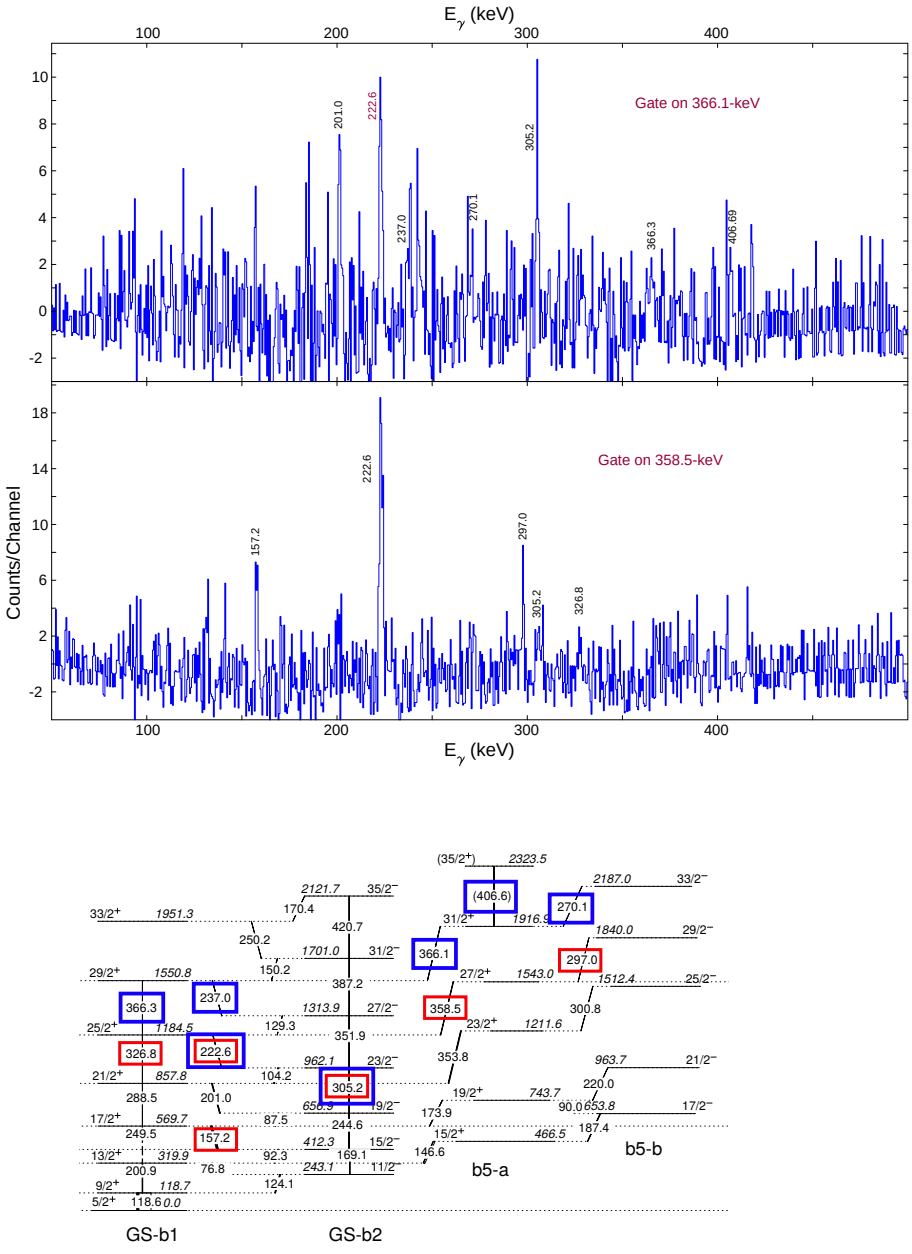


**Figure 5.7:** The spectra show two additional transitions reported by Maquart [7]. The 358.5-keV, $27/2^+ \rightarrow 25/2^+$, transition is in coincidence with the 326.8-keV, $25/2^+ \rightarrow 21/2^+$, and the 222.6-keV, $25/2^+$[GS-b1] $\rightarrow$ $23/2^-$[GS-b2], $\gamma$-ray transitions (Red boxes). The 366.1-keV, $31/2^+$[b5-a] $\rightarrow$ $29/2^+$[GS-b1], transition is a doublet with the 366.3-keV, $29/2^+ \rightarrow 25/2^+$[GS-b1], and also, with the 237.0-keV, $29/2^+$[GS-b1] $\rightarrow$ $27/2^-$[GS-b2], transitions (Blue boxes).

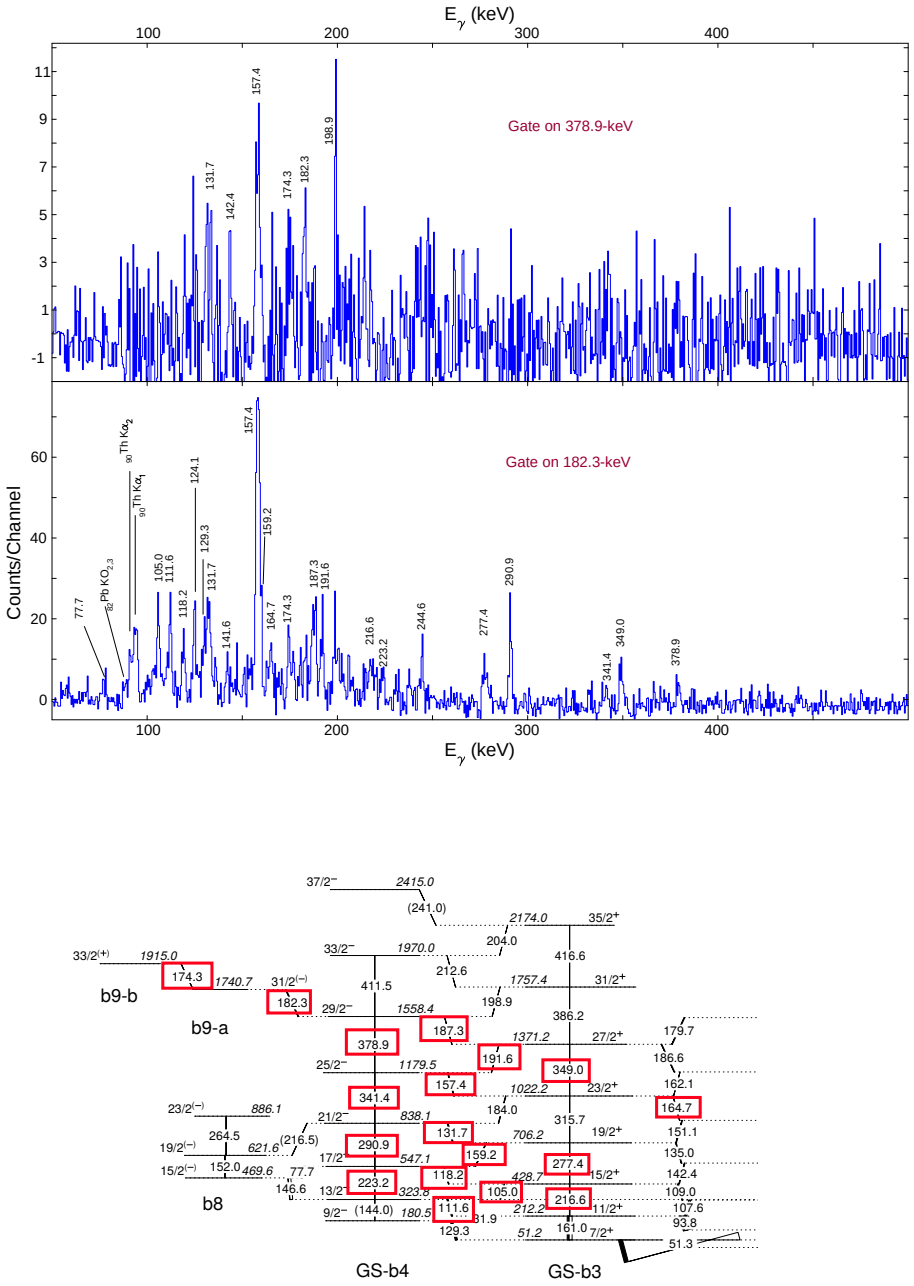


**Figure 5.8:** Lower: The 182.3-keV, $31/2^{(-)}$[b9-a] $\rightarrow$ $29/2^{-}$[GS-b4], transition has been proposed in this position due to the coincidences with the $\gamma$-ray transitions shown in the red boxes. Upper: Gate on the 182.3-keV, $31/2^{(-)} \rightarrow 29/2^{-}$], and the 378.9-keV, $29/2^{-} \rightarrow 25/2^{-}$[GS-b4], transition shows the coincidence with the 174.3-keV, $33/2^{(+)}$[b9-b] $\rightarrow$ $31/2^{(-)}$[b9-a], $\gamma$-ray transition.

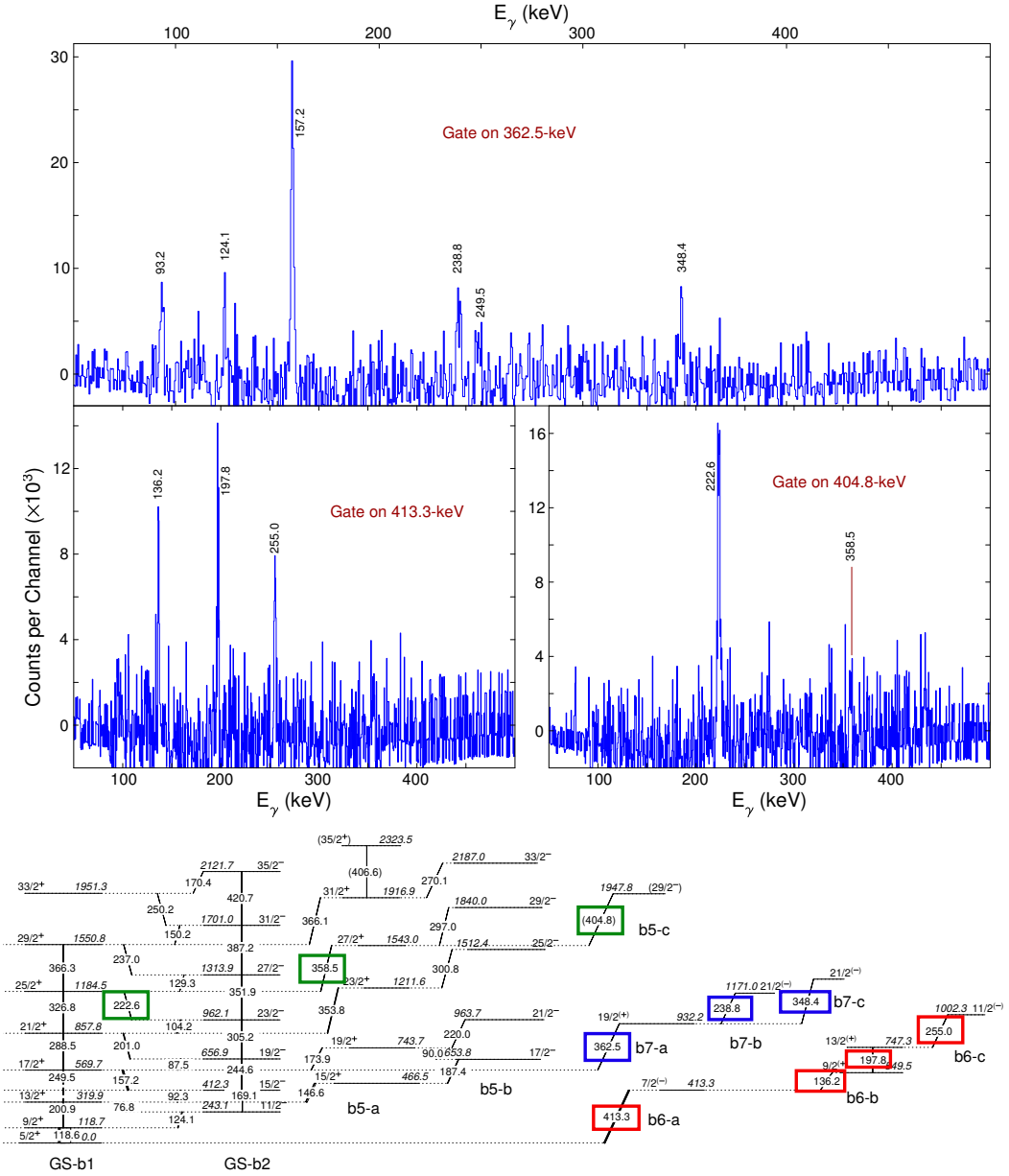


**Figure 5.9:** Center middle: Spectrum gated on the 413.3-keV, $7/2^{(-)}$[b6-a] $\rightarrow$ $5/2^{+}$[GS-b1], transition. Middle: Spectrum gated on the (404.8)-keV, $(29/2^{-})$ [b5-c] $\rightarrow$ $27/2^{+}$[b5-a], $\gamma$-ray transition. Upper: Spectrum gated on the 362.5-keV, $19/2^{(+)}$[b7-a] $\rightarrow$ $17/2^{+}$[GS-b1], $\gamma$-ray transition.

## 5.2 Comparison with previous work

In relation with Ref [7] which presents results for $^{223}_{90}$Th using the same reaction but different setup, some of the transitions have been confirmed, new transitions have been added, and other transitions that are not seen in this work will be also presented. In this section a comparison between a recent work published by G. Maquart *et. al* [7] and the data analysis from this work is made. Below some comments about G. Maquart's work when is compared with our work:

- The 331-keV, $27/2^{(+)} \rightarrow 23/2^{(+)}$ and the 373-keV $31/2^{(+)} \rightarrow 27/2^{(+)}$ transitions have no been found in coincidence each other as the 3(a) band suggests (See fig. 5.10). The intensities observed in the spectra from this work are very low, belonging to the background.
- The 353-keV, 23/2$^{(+)}$[3(a)] $\rightarrow$ 21/2$^{+}$[2(b)]) transition. 5.10) is observed in this work in the b5-a structure.
- The 404.8-keV, (29/2)$^{-} \rightarrow 27/2^{+}$, is believed to be in coincidence with the 358-keV, 27/2$^{(+)} \rightarrow 25/2^{+}$. We have proposed a configuration in the b5-c structure for the 404.8-keV, $29^{-} \rightarrow 27^{+}$.
- The proposed 366-keV, 31/2$^{(+)} \rightarrow 29/2^{+}$, transition has been confirmed in this work.
- The transitions reported on the lower scheme of fig. 5.10 as an extension band are not observed by us:
  - Transitions over level with 33/2$^{-}$ on 1(a) band.
  - Transitions over level with 35/2$^{+}$ on 1(b) band.
  - Transitions over level with 31/2$^{-}$ on 2(a) band.
  - Transitions over level with 33/2$^{+}$ on 2(b) band.

There are four parity doublets at medium and high spin.

- The level at $E_x = 323.8$ keV, $13/2^{-}$, and the level at $E_x = 319.9$ keV, $13/2^{+}$
- The level at $E_x = 469.9$ keV, $15/2^{(-)}$ and the level at $E_x = 466.5$ keV, $15/2^{+}$
- The level at $E_x = 428.7$ keV, $15/2^{+}$ and the level at $E_x = 412.3$ keV, $15/2^{-}$
- The level at $E_x = 1179.5$ keV, $25/2^{-}$ and the level at $E_x = 1184.5$ keV, $15/2^{+}$

- The level at $E_x = 1558.4$ keV, $29/2^-$, and the level at $E_x = 1550.8$ keV, $29/2^+$
- The M1 crossover transitions between GS-b1 and GS-b3 bands have been reported for first time in this work.
- The b8 and b9 bands are proposed for the first time in this work for the level scheme of $^{223}$Th.

The average branching ratios obtained in this work for the whole level scheme of $^{223}_{90}$Th are:

$$\overline{B(E1)/B(E2)} = 1.83(34) \times 10^{-9}\ fm^{-2}$$

$$\overline{B(M1)/B(E2)} = 0.47(9) \times 10^{-9}\,(\mu_N/eb)^2$$

The literature report the following values:

$$\overline{B(E1)/B(E2)} = 1.68(32) \times 10^{-9}\ fm^{-2}$$

$$\overline{B(M1)/B(E2)} = 0.712(25) \times 10^{-9}\,(\mu_N/eb)^2$$

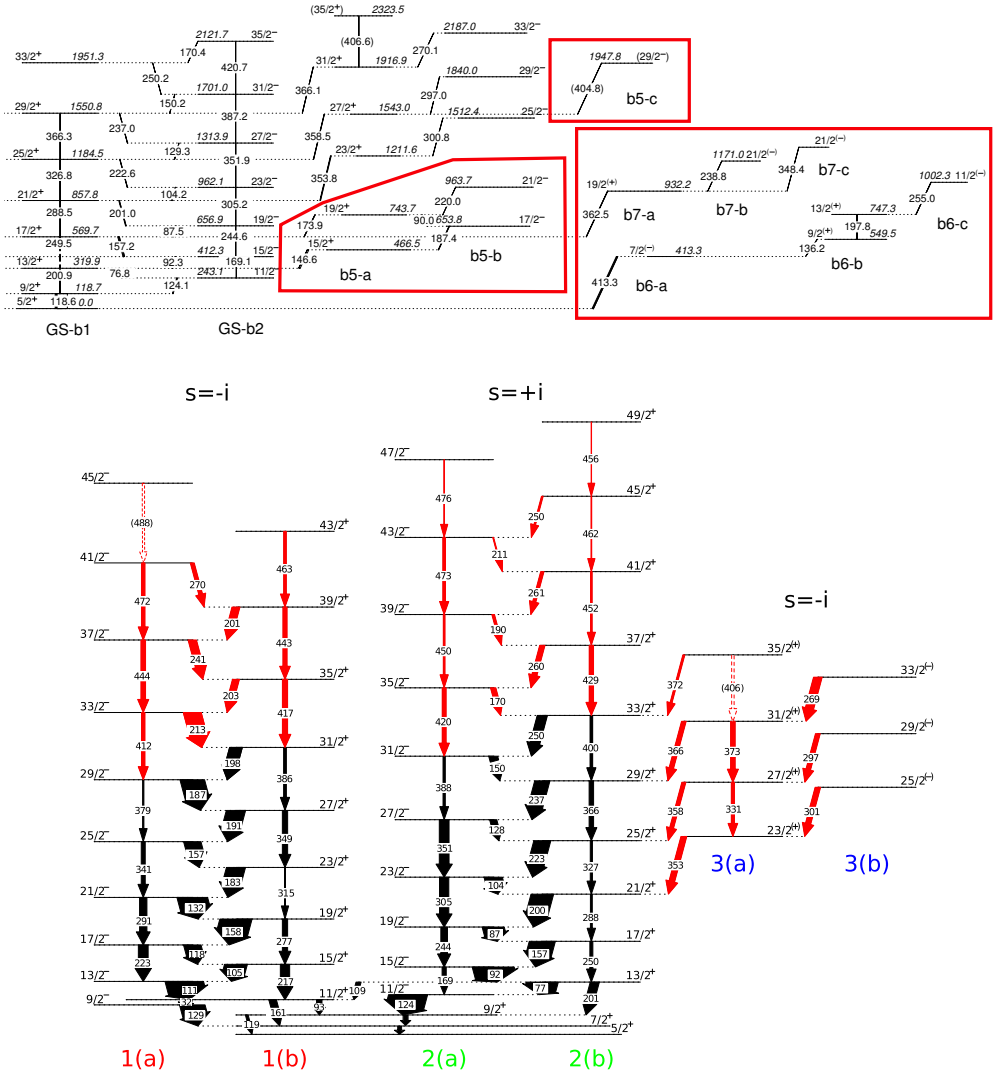


**Figure 5.10:** Comparison between the work from Maquart's et. al.'s level scheme [7] and this work. Lower: According to ref. [7]'s work, the 3(a) and 3(b) structures are non-yrast bands and a backbending phenomenon ha been reported. Upper: On the b5 structure the $E2$-type transitions cannot be confirmed in this work. The red boxes enclose the new transitions found from the analyzed experimental data in this study.

CHAPTER

# 6

# Discussion

In chapter 5, the level schemes for $^{223}$Th and for its neighbor contaminat isotopes, $^{220}$Ra and $^{224}$Th, were presented. Additional experimental information is sorted in the tables of the Appendixes. In this section, the discussion will be focused in two quantities: relative energies and parity splittings. In the nuclear model exposed in ref. [63], the nuclear deformation is explained through the multiple-type interaction between valence nucleons and the core. The nuclear core determines a self-consistet potential which can be modeled by even-multipole interaction. The unpaired nucleons interact with the average potential through residual forces: long-range multipole-multipole forces in the direction of the holes, in otherwise, short-long pairing forces in the direction of the particles. The valence nucleons polarize the core establishing stable or unstable electromagnetic moments [22]. The $^{224}$Th is considered as a transitional isotope between even-even nuclei with quadrupole to octupole deformation. The level scheme for the $^{224}$Th shows two rotational bands with $E2$ transitions increasing the level spacing with spin. Additional to the later, there is an alternating parity, evidence of a asymmetric-reflection: There is an stable quadrupole and octupole correlations [8]. Valence nucleons can weaken even-multipolarity and to strengthen Odd-multipolarity correlations. $^{223}$Th is thought to be a nucleus with a strong coupling between the unpaired neutron and the core.

## 6.1 Intensities

The level scheme for $^{223}$Th shown in Fig. 5.5 establishes four rotational bands: Two bands (Gs-b1 and Gs-b2) with alternating parity and positive simplex number and two bands (Gs-b3 and Gs-b4) with alternating parity and negative simplex number. The b5-a, b5-b and b5-c sequences, which are reported as the 3(a) and 3(b) structures in the Maquart's level scheme (Fig. 5.10) could have a negative simplex number. Nevertheless, the experimental data of this study does not allow construct $E2$-type transitions and the conclusion of a new non-yrast rotational band is not consistent. Fig. 6.1 shows that the intensities are larger for positive parities than negative parities at low spin. At medium spin, the intensity increases slowly and it becomes larger for negative parities than positive parities. At high spin, the intensities are similar. The latter provide useful information about the deformation with spin.

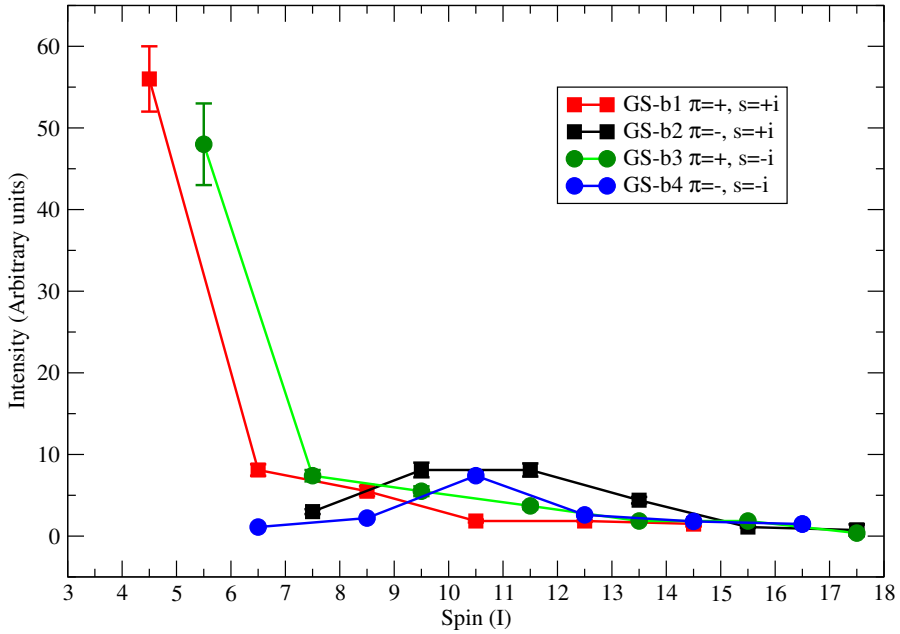


**Figure 6.1:** Slowing intensity with spin.

It is interesting the symmetry of the black and blue curves in Fig. 6.1 around the spin 21/2 for negative parity bands. In this region, the intensity is larger for negative parity than positive parity bands where the splitting parity, $\delta E$, has a minimum. It could imply a reduction of the probability of the $E1$ transitions, which indicates an attenuation of the electric dipolar moment. The quadrupole and the octupole modes must transfer $4\hbar$ of the

angular momentum to the $I^+ \rightarrow (I-1)^-$ transition, but if the frequency difference has only $2\hbar$, the possible transition is $I^- \rightarrow (I-1)^+$. When the transition frequency different is reduced, the transition probabilities between two transitions-type become the same, then, shows up a static dipole moment. The behavior around spin 21/2 can be understand as an unstable octupole deformation which come from stable heart shape at low spin, and it pass through a phase transition at medium spin. At high spin an stable octupole deformation is again reached. The mechanism is exposed in the A-Appendixes.

## 6.2 $\delta E$

The $\delta E$ value is a measurement of the evolution of the octupole correlation [7] and it indicates the interpolation of a positive parity state between two consecutive negative parity states:

$$\delta(E(I^-) = E(I^-) - \frac{(I+1)E_{(I-1)^+} + IE_{(I+1)^+}}{2I+1} \tag{6.1}$$

Fig. 6.2 shows the characteristic tendency of the isotopes with octupole deformation. At low spin the splitting has a high positive value, at medium spin it changes sing to negative, and at high spin, the splitting value tend to zero. $\delta E \sim 0$ indicates that the rotation stabilizes the octupole deformation [7, 8]. It is more favorable for the nucleus to increase the spin with the alignment of the phonos along the symmetry axis than to increases the angular frequency. All details about the condensation of rotational-aligned octupole phonos is explained by Frauendorf in ref. [64]. We can imagine an octupole wave traveling over the rigid rotor surface. The rotor has a rotational frequency of $\omega_r$ and the octupole wave has a frequency $\omega_p$. The frequency of the octupole wave over the rotor surface seen from laboratory framework is $\omega_p - \omega_r$. If $\omega_r = \omega_p$, the parity splitting is zero and the deformation of the nucleus is the sum of the quadrupole plus octupole modes, leading to an stable shape. In this interpretation, the frequency of the octupole mode is the that rigid octupole rotor and an electric dipole is induced allowing transitions E1-type. With rigor, three parity doublets have been observed: At medium (13/2) and high spin (25/2 and 29/2). In real case, the frequencies are not the same, an a fluctuation around zero is evident. When $\delta E \sim 0$ the interaction between phonons is stronger, and the level repulsion increases because the even-phonons and odd-phonos have the same parity. It is say, the even-multipole competes with the odd-multipole, and the transitions $I^- \rightarrow (I-1)^+$ acquire the same probability as $I^+ \rightarrow (I-1)^-$. The sum of the $Y_{20} + Y_{30}$ modes from the equation 2.16 generate an effective electric dipole moment and the transitions $E1$-type are a finger of the heart shape.

The first vision about asymmetric-reflection was the oscillation of a cluster by tunneling

through the nuclear potential. The change of chirality determines the two sequences of states with opposite parity. The increasing of the angular moment can quench the tunnel effect and the deformation becomes stable. However, fluctuation around zero of the parity splitting have been observed and the interpretation of a like a pear-shape can be more complex.

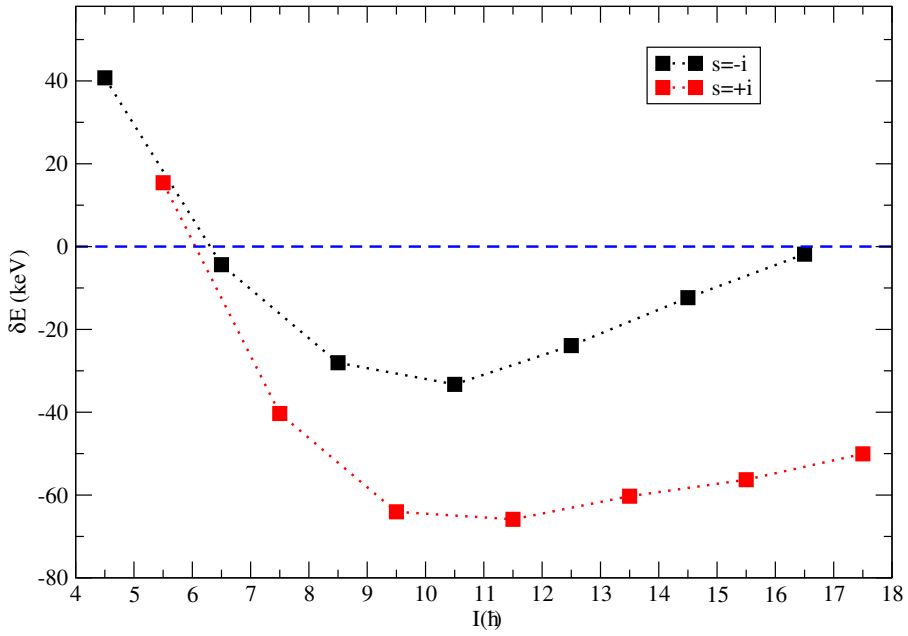


**Figure 6.2:** Energy splitting between states of opposite parity but the same simplex number: $\delta(E(I^-) = E(I^-) - \frac{(I+1)E_{(I-1)^+} + IE_{(I+1)^+}}{2I+1}$.

## 6.3 Relative Energy

The energy differences between energy levels with the same spin and opposite parity and simplex, give us information about the $K$-value number. According to the analysis for $^{221}$Th made by Reviol et. al. [8], parity doublets for $K = 0$ and $K = 1/2$ bands does not emerge because those groups have good simplex number (See fig. 3.1). The parity doublets have been related with the $K = 5/2$ configurations and the experimental data in Fig. 6.3 confirm this hypothesis. The new parity doublet found at $E_x = 469.6$ keV, $15/2^{(-)}$, and at $E_x = 466.5$ keV, $15/2^+$, could determinate a non-yrast structure if transitions $E2$-type are confirmed. In this case, the b8 band would be a positive simplex band and the b5 structure, a negative simplex band. That conclusion rise up from the finger that determine the

asymmetric-reflection: The decay through $M1$ transitions. These $M1$ high-energy transitions from $s = -i$ non-yrast bands to $s = +i$ yrast band have higher intensity regard the transitions from the $s = -i$ yrast band to $s = +i$ non-yrast band, and then, the connections between Gs-b1 band to b5-a band cannot be seen due the low probability [65].

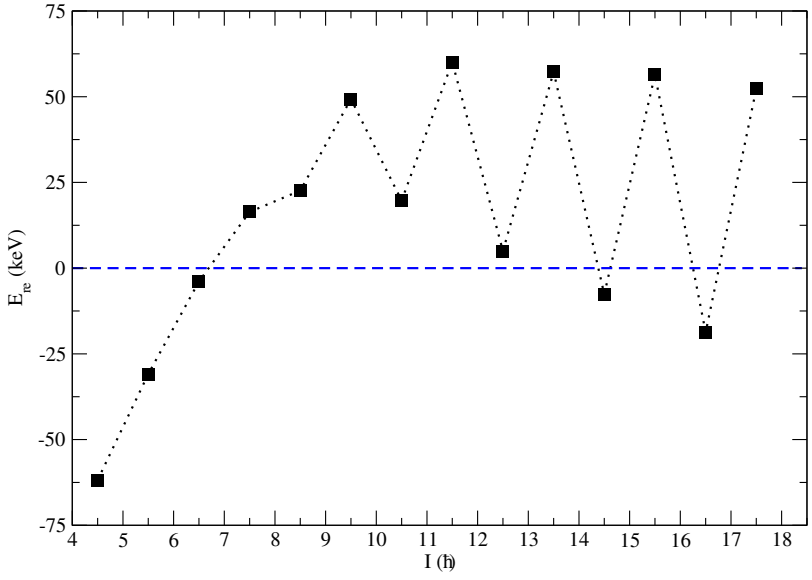


**Figure 6.3:** Relative scale of the excitation energies: $E_{rel} = E(s = +i) - E(s = -i)$.

*The science of today is the technology of tomorrow.*

Edward Teller

CHAPTER

7

# Conclusions and Perspectives

The level scheme for $^{223}_{90}$Th was built from experimental data obtained from the $^{208}_{82}\mathrm{Pb}\left(^{18}_{8}\mathrm{O},\ 3\mathrm{n}\right)^{223}_{90}\mathrm{Th}$ reaction in an experiment performed at the Argonne National Laboratory by the Washington University group. The yrast structures were contrasted with to the last publication written by Maquart *et. al.* [7]. 26 new transitions and 17 new energy levels were identified in this study. On the other hand, a new transition was found for each contaminant, $^{220}_{88}$Ra and $^{224}_{90}$Th.

The yrast bands, GS-b1 and GS-b2 with simplex number $s = i$, and the GS-b3 and GS-b4 bands, with simplex number $s = -i$ tell us about the quadrupole-octupole band structure because each pair of bands, with the same simplex number determines an alternating parity sequences for their spin states. Three strict parity doublets have been observed for level energy at the $E_x = 323.6$ keV, $13/2^-$, and at the $E_x = 319.9$ keV, $13/2^+$; at the $E_x = 1179.5$ keV, $25/2^-$, and the $E_x = 1184.5$ keV, $25/2^+$; at the $E_x = 1558.4$ keV, $29/2^-$, and at the $E_x = 1550.8$ keV, $29/2^+$. The last allows us to confirm the spin assingment of 5/2$\hbar$ for the ground state. According to the analysis for $^{221}_{90}$Th made by W. Reviol *et. al.* [8], structures with spin assingment $K < 5/2$ do not exhibit parity doublets and the energy splitting is larger than structures with octupole deformation. The presence of parity doublets at medium (13/2) and at high (29/2) spin is evidence of the $K = 5/2$ structure for $^{223}_{90}$Th.

A new doublet was found at $E_x = 469.6$ keV, $15/2^{(-)}$ and at the $E_x = 466.5$ keV, $15/2^+$. It is necessary to calculate angular distribution of the $\gamma$-ray radiation to confirm the spin

and parity. The $E2$-type transitions for the new structures cannot be confirmed in this work, so, the new structures cannot be confirmed as non-yrast structures. It is possible that the intensities for $E2$ transitions in those new structures lead to be very low, however, due that the intensity is in ratio with the probability of the transition, it is right to say that the quadrupole character is null.

Measurements of ratios, $B(M1)/B(M2)$, tell us that the octupole behavior is present at low and medium spin because the presence of $M1$ crossover transitions between the GS-b1 and GS-b3 bands. It is evidence a flip of the spin, then, the contribution of the independent particle is strong.

The challenge after this analysis is to continue with the following tasks:

- To calculate the $A_1$, $A_2$ and $A_3$ coefficients of the angular distribution and to determine the weight for each multipole order of the structures.
- To determine what is the explanation of the new structures found in this level scheme.

This work is in construction yet. The information contain in this work is a source of experimental evidence for the formulation of new theoretical models and future experiments.

# Appendices

# A. List of level energy values

**Table 1:** List of the level energies values. States sorted with the same simplex number. Each column shows a sequence of alternating parity states (GS-b1 and GS-b2 bands have the same simplex number but opposite parity). The simplex number and parity of the GS-b3 and GS-b4 bands are opposite to the GS-b1 and GS-b2 bands respectively.

| Level Energy | $J^{\pi,\ s=+i}$ | Band | Level Energy | $J^{\pi,\ s=-i}$ | Band |
|---|---|---|---|---|---|
| 0.0(0) | $5/2^+$ | GS-b1 | 180.5(8) | $9/2^-$ | GS-b4 |
| 118.7(8) | $9/2^+$ | GS-b1 | 323.8(9) | $13/2^-$ | GS-b4 |
| 319.9(9) | $13/2^+$ | GS-b1 | 547.1(10) | $17/2^-$ | GS-b4 |
| 569.7(9) | $17/2^+$ | GS-b1 | 838.1(10) | $21/2^-$ | GS-b4 |
| 857.8(10) | $21/2^+$ | GS-b1 | 1179.5(11) | $25/2^-$ | GS-b4 |
| 1184.5(11) | $25/2^+$ | GS-b1 | 1558.4(13) | $29/2^-$ | GS-b4 |
| 1550.8(13) | $29/2^+$ | GS-b1 | 1970.0(14) | $33/2^-$ | GS-b4 |
| 1951.3(22) | $33/2^+$ | GS-b1 | 2415.0(18) | $37/2^-$ | GS-b4 |
| 243.1(9) | $11/2^-$ | GS-b2 | 51.2(8) | $7/2^+$ | GS-b3 |
| 412.3(9) | $15/2^-$ | GS-b2 | 212.2(8) | $11/2^+$ | GS-b3 |
| 656.9(9) | $19/2^-$ | GS-b2 | 428.7(9) | $15/2^+$ | GS-b3 |
| 962.1(10) | $23/2^-$ | GS-b2 | 706.2(10) | $19/2^+$ | GS-b3 |
| 1313.9(12) | $27/2^-$ | GS-b2 | 1022.2(10) | $23/2^+$ | GS-b3 |
| 1701.0(20) | $31/2^-$ | GS-b2 | 1371.2(11) | $27/2^+$ | GS-b3 |
| 2121.7(22) | $35/2^-$ | GS-b2 | 1757.4(13) | $31/2^+$ | GS-b3 |
| | | | 2174.0(15) | $35/2^+$ | GS-b3 |

# B. New non-yrast structures

**Table 2:** New non-yrast structures. Because the low intensity of the $E2$-type transitions, the new structures can not be confirmed as rotational bands. Nevertheless, the existence of such transitions could be thought as part of the level scheme by completeness. The b5 structure is an example of this idea. In the Maquart's level scheme for $^{223}_{90}$Th, the $E2$ transitions in b5-a band are reported, while this work has suppressed this values because thet are not visible in the gate of coincidences.

| New structures with parity assignments | | | New structures with tentative parity assignments | | |
|---|---|---|---|---|---|
| Level Energy | $J^\pi$ | Band | Level Energy | $J^\pi$ | Band |
| 466.5(10) | $15/2^+$ | b5-a | 469.6(10) | $15/2^{(-)}$ | b8 |
| 743.7(10) | $19/2^+$ | b5-a | 621.6(11) | $19/2^{(-)}$ | b8 |
| 1211.6(14) | $23/2^+$ | b5-a | 886.1(12) | $23/2^{(-)}$ | b8 |
| 1543.0(15) | $27/2^+$ | b5-a | 1740.7(16) | $31/2^{(-)}$ | b9-a |
| 1916.9(16) | $31/2^+$ | b5-a | 1915.0(17) | $33/2^{(+)}$ | b9-b |
| 2323.5(19) | $(35/2^+)$ | b5-a | 932.2(13) | $19/2^{(+)}$ | b7-a |
| 653.8(12) | $17/2^-$ | b5-b | 1171.0(17) | $21/2^{(-)}$ | b7-b |
| 963.7(14) | $21/2^-$ | b5-b | 1280.7(17) | $21/2^{(-)}$ | b7-c |
| 1512.4(17) | $25/2^-$ | b5-b | 413.3(10) | $7/2^{(-)}$ | b6-a |
| 1840.0(18) | $29/2^-$ | b5-b | 549.5(14) | $9/2^{(+)}$ | b6-b |
| 2187.0(19) | $33/2^-$ | b5-b | 747.3(17) | $13/2^{(+)}$ | b6-b |
| 1947.8(16) | $(29/2^-)$ | 5b-c | 1002.3(20) | $11/2^{(-)}$ | b6-c |

# C. List of $B(M1)/B(E2)$ ratios

**Table 3:** List of $B(M1)/B(E2)$ ratios in units of $(\mu_N/eb)^2$ where $\mu$ is the nuclear magneton, $e$ is the proton charge and $b$ is a barn=$10^{-28}$ m$^2$. The energies are in units of keV and the intensities are normalized in arbitrary units.

| Initial | Final | $E_\gamma$ | $I_\gamma$ | Err | $\lambda$ | Err | $B(M1)/B(E2)$ | Err |
|---|---|---|---|---|---|---|---|---|
| GS-b1 | GS-b1 | 118.6 | 55.72 | 4.43 | | | | |
| | GS-b3 | 67.5 | 7.75 | 0.22 | 7.190 | 0.607 | 0.007 | 0.001 |
| GS-b1 | GS-b1 | 200.9 | 8.12 | 0.74 | | | | |
| | GS-b3 | 107.6 | 11.07 | 1.11 | 0.733 | 0.099 | 0.248 | 0.034 |
| GS-b1 | GS-b1 | 249.5 | 5.54 | 0.55 | | | | |
| | GS-b3 | 142.4 | 1.85 | 0.18 | 3.000 | 0.424 | 0.077 | 0.011 |
| GS-b1 | GS-b1 | 288.5 | 1.85 | 0.18 | | | | |
| | GS-b3 | 151.1 | 2.33 | 0.35 | 0.792 | 0.143 | 0.507 | 0.092 |
| GS-b1 | GS-b1 | 326.8 | 1.85 | 0.11 | | | | |
| | GS-b3 | 162.1 | 0.74 | 0.07 | 2.500 | 0.292 | 0.024 | 0.003 |
| GS-b1 | GS-b1 | 366.3 | 1.48 | 0.30 | | | | |
| | GS-b3 | 179.7 | 3.69 | 0.37 | 0.400 | 0.089 | 1.970 | 0.440 |
| GS-b2 | GS-b2 | 169.1 | 2.95 | 0.30 | | | | |
| | GS-b4 | 88.3 | 2.58 | 0.26 | 1.143 | 0.162 | 0.122 | 0.017 |
| GS-b3 | GS-b3 | 161.0 | 47.97 | 4.80 | | | | |
| | GS-b1 | 93.8 | 37.64 | 3.69 | 1.275 | 0.178 | 0.071 | 0.010 |
| GS-b3 | GS-b3 | 216.6 | 7.38 | 0.74 | | | | |
| | GS-b1 | 109.0 | 4.43 | 0.44 | 1.667 | 0.236 | 0.153 | 0.022 |
| GS-b3 | GS-b3 | 277.4 | 5.54 | 0.55 | | | | |
| | GS-b1 | 135.0 | 1.85 | 0.18 | 3.000 | 0.424 | 0.154 | 0.022 |
| GS-b3 | GS-b3 | 315.7 | 3.69 | 0.37 | | | | |
| | GS-b1 | 164.7 | 1.49 | 0.20 | 2.477 | 0.414 | 0.196 | 0.033 |
| GS-b3 | GS-b3 | 349.0 | 1.85 | 0.18 | | | | |
| | GS-b1 | 186.6 | 3.69 | 0.37 | 0.500 | 0.071 | 1.104 | 0.156 |
| GS-b4 | GS-b4 | 223.2 | 2.21 | 0.22 | | | | |
| | b8 | 77.7 | 5.17 | 1.11 | 0.429 | 0.101 | 1.909 | 0.452 |
| GS-b4 | GS-b4 | 290.9 | 7.38 | 0.48 | | | | |
| | b8 | 216.5 | 1.11 | 0.11 | 6.667 | 0.795 | 0.021 | 0.003 |

# D. Listof $B(E1)/B(E2)$ ratios

**Table 4:** $B(E1)/B(E2)$ $\left(10^{-9}\text{ (fm)}^{-}2\right)$ where a fm=$10^{-15}$ m. The energies are in units of keV and the intensities are in arbitrary units.

| Initial | Final | $E_\gamma$ | $I_\gamma$ | Err | $\lambda$ | Err | B(E1)/B(E2) | Err |
|---|---|---|---|---|---|---|---|---|
| GS-b1 | GS-b1 | 200.9 | 8.12 | 0.74 | | | | |
| | GS-b2 | 76.8 | 21.40 | 1.85 | 0.379 | 0.048 | 1460.89 | 183.03 |
| GS-b1 | GS-b1 | 249.5 | 5.54 | 0.55 | | | | |
| | GS-b2 | 157.2 | 40.59 | 4.06 | 0.136 | 0.019 | 1399.88 | 197.97 |
| GS-b1 | GS-b1 | 288.5 | 1.85 | 0.18 | | | | |
| | GS-b2 | 201.0 | 15.50 | 1.55 | 0.119 | 0.017 | 1585.68 | 224.25 |
| GS-b1 | GS-b1 | 326.8 | 1.85 | 0.11 | | | | |
| | GS-b2 | 222.6 | 6.64 | 0.66 | 0.278 | 0.032 | 933.11 | 108.82 |
| GS-b1 | GS-b1 | 366.3 | 1.48 | 0.30 | | | | |
| | GS-b2 | 237.0 | 4.43 | 0.44 | 0.333 | 0.075 | 1139.87 | 254.88 |
| GS-b2 | GS-b2 | 169.1 | 2.95 | 0.30 | | | | |
| | GS-b1 | 92.3 | 25.09 | 2.51 | 0.118 | 0.017 | 1146.38 | 162.12 |
| GS-b2 | GS-b2 | 244.6 | 8.12 | 0.92 | | | | |
| | GS-b1 | 87.5 | 15.51 | 1.82 | 0.523 | 0.086 | 1914.03 | 312.81 |
| GS-b2 | GS-b2 | 305.2 | 8.12 | 0.81 | | | | |
| | GS-b1 | 104.2 | 18.45 | 1.85 | 0.440 | 0.062 | 4080.02 | 577.00 |
| GS-b2 | GS-b2 | 351.9 | 4.43 | 0.44 | | | | |
| | GS-b1 | 129.3 | 1.85 | 0.30 | 2.400 | 0.453 | 797.78 | 150.53 |
| GS-b2 | GS-b2 | 387.2 | 1.11 | 0.11 | | | | |
| | GS-b1 | 150.2 | 1.85 | 0.18 | 0.600 | 0.085 | 3283.30 | 464.33 |
| GS-b3 | GS-b3 | 161.0 | 47.97 | 4.80 | | | | |
| | GS-b4 | 31.9 | 44.28 | 4.43 | 1.083 | 0.153 | 2361.27 | 333.93 |
| GS-b3 | GS-b3 | 216.6 | 7.38 | 0.74 | | | | |
| | GS-b4 | 105.0 | 11.07 | 1.11 | 0.667 | 0.094 | 473.82 | 67.01 |
| GS-b3 | GS-b3 | 277.4 | 5.54 | 0.55 | | | | |
| | GS-b4 | 159.2 | 12.92 | 0.15 | 0.429 | 0.043 | 728.58 | 73.33 |
| GS-b3 | GS-b3 | 315.7 | 3.69 | 0.37 | | | | |
| | GS-b4 | 184.0 | 10.33 | 1.03 | 0.357 | 0.051 | 1081.11 | 152.89 |
| GS-b3 | GS-b3 | 349.0 | 1.85 | 0.18 | | | | |

| | | | | | | | | |
|---|---|---|---|---|---|---|---|---|
| | GS-b4 | 191.6 | 6.78 | 0.59 | 0.272 | 0.036 | 2075.94 | 274.54 |
| GS-b3 | GS-b3 | 386.2 | 1.85 | 0.18 | | | | |
| | GS-b4 | 198.9 | 3.32 | 0.37 | 0.556 | 0.083 | 1505.51 | 224.15 |
| GS-b4 | GS-b4 | 144.0 | 1.11 | 0.11 | | | | |
| | GS-b3 | 111.6 | 24.72 | 0.26 | 0.045 | 0.005 | 763.08 | 76.72 |
| GS-b4 | GS-b4 | 223.2 | 2.21 | 0.22 | | | | |
| | GS-b3 | 118.2 | 11.81 | 1.11 | 0.188 | 0.026 | 1372.18 | 188.09 |
| GS-b4 | GS-b4 | 290.9 | 7.38 | 0.48 | | | | |
| | GS-b3 | 131.7 | 20.71 | 1.34 | 0.356 | 0.033 | 1960.92 | 180.00 |
| GS-b4 | GS-b4 | 341.4 | 2.58 | 0.26 | | | | |
| | GS-b3 | 157.4 | 14.76 | 1.48 | 0.175 | 0.025 | 5212.70 | 737.19 |
| GS-b4 | GS-b4 | 378.9 | 1.85 | 0.26 | | | | |
| | GS-b3 | 187.3 | 6.64 | 0.66 | 0.278 | 0.048 | 3281.78 | 564.62 |
| GS-b4 | GS-b4 | 411.5 | 1.48 | 0.11 | | | | |
| | GS-b3 | 212.6 | 1.48 | 0.15 | 1.000 | 0.125 | 941.81 | 117.73 |
| GS-b3 | GS-b3 | 416.6 | 0.37 | 0.20 | | | | |
| | GS-b4 | 204.0 | 1.11 | 0.11 | 0.333 | 0.186 | 3401.14 | 1901.24 |
| GS-b2 | GS-b2 | 420.7 | 0.74 | 0.07 | | | | |
| | GS-b1 | 170.4 | 0.37 | 0.26 | 2.000 | 1.420 | 1021.58 | 725.11 |

# E. List of transitions

**Table 5:** List of all transitions sorted in the level scheme of $^{223}_{90}$Th. All $\gamma$ rays were obtained from the experimental spectra of coincidences of this work. The most of them have been confirmed, and also, new transitions have been proposed.

| $E_i$ (keV) | $Band_i$ | $\rightarrow$ | $Band_f$ | $J_i^\pi$ | $\rightarrow$ | $J_f^\pi$ | $E_\gamma$ (keV) | $I_\gamma$ | $\lambda$ |
|---|---|---|---|---|---|---|---|---|---|
| 119 | $GS-b1$ | $\rightarrow$ | $GS-b3$ | $9/2^+$ | $\rightarrow$ | $7/2^+$ | 67.5(10) | 7.75(22) | M1 |
| 119 | $GS-b1$ | $\rightarrow$ | $GS-b1$ | $9/2^+$ | $\rightarrow$ | $5/2^+$ | 118.6(10) | 56(4) | E2 |
| 320 | $GS-b1$ | $\rightarrow$ | $GS-b2$ | $13/2^+$ | $\rightarrow$ | $11/2^-$ | 76.8(5) | 21.4(18) | E1 |
| 320 | $GS-b1$ | $\rightarrow$ | $GS-b3$ | $13/2^+$ | $\rightarrow$ | $11/2^+$ | 107.6(10) | 11.1(11) | M1 |
| 320 | $GS-b1$ | $\rightarrow$ | $GS-b1$ | $13/2^+$ | $\rightarrow$ | $9/2^+$ | 200.9(10) | 8.1(7) | E2 |
| 570 | $GS-b1$ | $\rightarrow$ | $GS-b3$ | $17/2^+$ | $\rightarrow$ | $15/2^+$ | 142.4(10) | 1.85(18) | M1 |
| 570 | $GS-b1$ | $\rightarrow$ | $GS-b2$ | $17/2^+$ | $\rightarrow$ | $15/2^-$ | 157.2(10) | 41(4) | E1 |
| 570 | $GS-b1$ | $\rightarrow$ | $GS-b1$ | $17/2^+$ | $\rightarrow$ | $13/2^+$ | 249.5(5) | 5.5(6) | E2 |
| 858 | $GS-b1$ | $\rightarrow$ | $GS-b3$ | $21/2^+$ | $\rightarrow$ | $19/2^+$ | 151.1(10) | 2.3(4) | M1 |
| 858 | $GS-b1$ | $\rightarrow$ | $GS-b2$ | $21/2^+$ | $\rightarrow$ | $19/2^-$ | 201.0(5) | 15.5(15) | E1 |
| 858 | $GS-b1$ | $\rightarrow$ | $GS-b1$ | $21/2^+$ | $\rightarrow$ | $17/2^+$ | 288(3) | 1.85(18) | E2 |
| 1185 | $GS-b1$ | $\rightarrow$ | $GS-b3$ | $25/2^+$ | $\rightarrow$ | $23/2^+$ | 162.1(10) | 0.74(7) | M1 |
| 1185 | $GS-b1$ | $\rightarrow$ | $GS-b2$ | $25/2^+$ | $\rightarrow$ | $23/2^-$ | 222.6(15) | 6.6(7) | E1 |
| 1185 | $GS-b1$ | $\rightarrow$ | $GS-b1$ | $25/2^+$ | $\rightarrow$ | $21/2^+$ | 326.8(10) | 1.85(11) | E2 |
| 1551 | $GS-b1$ | $\rightarrow$ | $GS-b3$ | $29/2^+$ | $\rightarrow$ | $27/2^+$ | 179.7(10) | 3.7(4) | M1 |
| 1551 | $GS-b1$ | $\rightarrow$ | $GS-b2$ | $29/2^+$ | $\rightarrow$ | $27/2^-$ | 237(3) | 4.4(4) | E1 |
| 1551 | $GS-b1$ | $\rightarrow$ | $GS-b1$ | $29/2^+$ | $\rightarrow$ | $25/2^+$ | 366.3(10) | 1.5(3) | E2 |
| 1951 | $GS-b1$ | $\rightarrow$ | $GS-b2$ | $33/2^+$ | $\rightarrow$ | $31/2^-$ | 250.2(10) | 2.6(3) | E1 |
| 243 | $GS-b2$ | $\rightarrow$ | $GS-b1$ | $11/2^-$ | $\rightarrow$ | $9/2^+$ | 124.1(10) | 17.0(13) | E1 |
| 412 | $GS-b2$ | $\rightarrow$ | $GS-b4$ | $15/2^-$ | $\rightarrow$ | $13/2^-$ | 88.3(10) | 2.6(3) | M1 |
| 412 | $GS-b2$ | $\rightarrow$ | $GS-b1$ | $15/2^-$ | $\rightarrow$ | $13/2^+$ | 92.3(10) | 25(3) | E1 |
| 412 | $GS-b2$ | $\rightarrow$ | $GS-b2$ | $15/2^-$ | $\rightarrow$ | $11/2^-$ | 169.1(5) | 3.0(3) | E2 |
| 657 | $GS-b2$ | $\rightarrow$ | $GS-b1$ | $19/2^-$ | $\rightarrow$ | $17/2^+$ | 87.5(5) | 15.5(18) | E1 |
| 657 | $GS-b2$ | $\rightarrow$ | $GS-b2$ | $19/2^-$ | $\rightarrow$ | $15/2^-$ | 244.6(5) | 8.1(9) | E2 |
| 962 | $GS-b2$ | $\rightarrow$ | $GS-b1$ | $23/2^-$ | $\rightarrow$ | $21/2^+$ | 104.2(10) | 18.5(18) | E1 |
| 962 | $GS-b2$ | $\rightarrow$ | $GS-b2$ | $23/2^-$ | $\rightarrow$ | $19/2^-$ | 305.2(5) | 8.1(8) | E2 |
| 1314 | $GS-b2$ | $\rightarrow$ | $GS-b1$ | $27/2^-$ | $\rightarrow$ | $25/2^+$ | 129.3(10) | 1.8(3) | E1 |
| 1314 | $GS-b2$ | $\rightarrow$ | $GS-b2$ | $27/2^-$ | $\rightarrow$ | $23/2^-$ | 351.9(10) | 4.4(4) | E2 |
| 1701 | $GS-b2$ | $\rightarrow$ | $GS-b1$ | $31/2^-$ | $\rightarrow$ | $29/2^+$ | 150.2(20) | 1.85(18) | E1 |
| 1701 | $GS-b2$ | $\rightarrow$ | $GS-b2$ | $31/2^-$ | $\rightarrow$ | $27/2^-$ | 387(3) | 1.11(11) | E2 |
| 2122 | $GS-b2$ | $\rightarrow$ | $GS-b1$ | $35/2^-$ | $\rightarrow$ | $33/2^+$ | 170.4(10) | 0.4(3) | E1 |
| 2122 | $GS-b2$ | $\rightarrow$ | $GS-b2$ | $35/2^-$ | $\rightarrow$ | $31/2^-$ | 420.7(10) | 0.74(7) | E2 |

| | | | | | | | | | |
|---|---|---|---|---|---|---|---|---|---|
| 51 | $GS-b3$ | $\rightarrow$ | $GS-b1$ | $7/2^+$ | $\rightarrow$ | $5/2^+$ | 51.3(10) | 100(9) | M1 |
| 212 | $GS-b3$ | $\rightarrow$ | $GS-b4$ | $11/2^+$ | $\rightarrow$ | $9/2^-$ | 31.9(10) | 44(4) | E1 |
| 212 | $GS-b3$ | $\rightarrow$ | $GS-b1$ | $11/2^+$ | $\rightarrow$ | $9/2^+$ | 93.8(10) | 38(4) | M1 |
| 212 | $GS-b3$ | $\rightarrow$ | $GS-b3$ | $11/2^+$ | $\rightarrow$ | $7/2^+$ | 161.00(7) | 48(5) | E2 |
| 429 | $GS-b3$ | $\rightarrow$ | $GS-b4$ | $15/2^+$ | $\rightarrow$ | $13/2^-$ | 105.0(10) | 11.1(11) | E1 |
| 429 | $GS-b3$ | $\rightarrow$ | $GS-b1$ | $15/2^+$ | $\rightarrow$ | $13/2^+$ | 109.0(5) | 4.4(4) | M1 |
| 429 | $GS-b3$ | $\rightarrow$ | $GS-b3$ | $15/2^+$ | $\rightarrow$ | $11/2^+$ | 216.6(10) | 7.4(7) | E2 |
| 706 | $GS-b3$ | $\rightarrow$ | $GS-b1$ | $19/2^+$ | $\rightarrow$ | $17/2^+$ | 135.0(10) | 1.85(18) | M1 |
| 706 | $GS-b3$ | $\rightarrow$ | $GS-b4$ | $19/2^+$ | $\rightarrow$ | $17/2^-$ | 159.2(5) | 12.92(15) | E1 |
| 706 | $GS-b3$ | $\rightarrow$ | $GS-b3$ | $19/2^+$ | $\rightarrow$ | $15/2^+$ | 277.4(10) | 5.5(6) | E2 |
| 1022 | $GS-b3$ | $\rightarrow$ | $GS-b1$ | $23/2^+$ | $\rightarrow$ | $21/2^+$ | 164.7(10) | 1.49(20) | M1 |
| 1022 | $GS-b3$ | $\rightarrow$ | $GS-b4$ | $23/2^+$ | $\rightarrow$ | $21/2^-$ | 184.0(10) | 10.3(10) | E1 |
| 1022 | $GS-b3$ | $\rightarrow$ | $GS-b3$ | $23/2^+$ | $\rightarrow$ | $19/2^+$ | 315.7(10) | 3.7(4) | E2 |
| 1371 | $GS-b3$ | $\rightarrow$ | $GS-b1$ | $27/2^+$ | $\rightarrow$ | $25/2^+$ | 186.6(10) | 3.7(4) | M1 |
| 1371 | $GS-b3$ | $\rightarrow$ | $GS-b4$ | $27/2^+$ | $\rightarrow$ | $25/2^-$ | 191.6(10) | 6.8(6) | E1 |
| 1371 | $GS-b3$ | $\rightarrow$ | $GS-b3$ | $27/2^+$ | $\rightarrow$ | $23/2^+$ | 349.0(10) | 1.85(18) | E2 |
| 1757 | $GS-b3$ | $\rightarrow$ | $GS-b4$ | $31/2^+$ | $\rightarrow$ | $29/2^-$ | 198.9(10) | 3.3(4) | E1 |
| 1757 | $GS-b3$ | $\rightarrow$ | $GS-b3$ | $31/2^+$ | $\rightarrow$ | $27/2^+$ | 386.2(10) | 1.85(18) | E2 |
| 2174 | $GS-b3$ | $\rightarrow$ | $GS-b4$ | $35/2^+$ | $\rightarrow$ | $33/2^-$ | 204.0(10) | 1.11(11) | E1 |
| 2174 | $GS-b3$ | $\rightarrow$ | $GS-b3$ | $35/2^+$ | $\rightarrow$ | $31/2^+$ | 416.6(10) | 0.37(20) | E2 |
| 180 | $GS-b4$ | $\rightarrow$ | $GS-b3$ | $9/2^-$ | $\rightarrow$ | $7/2^+$ | 129.30(3) | 44(4) | E1 |
| 324 | $GS-b4$ | $\rightarrow$ | $GS-b3$ | $13/2^-$ | $\rightarrow$ | $11/2^+$ | 111.6(10) | 24.7(3) | E1 |
| 324 | $GS-b4$ | $\rightarrow$ | $GS-b4$ | $13/2^-$ | $\rightarrow$ | $9/2^-$ | 144.0(10) | 1.11(11) | E2 |
| 547 | $GS-b4$ | $\rightarrow$ | $b8$ | $17/2^-$ | $\rightarrow$ | $15/2^{(-)}$ | 77.7(5) | 5.2(11) | M1 |
| 547 | $GS-b4$ | $\rightarrow$ | $GS-b3$ | $17/2^-$ | $\rightarrow$ | $15/2^+$ | 118.2(10) | 11.8(11) | E1 |
| 547 | $GS-b4$ | $\rightarrow$ | $GS-b4$ | $17/2^-$ | $\rightarrow$ | $13/2^-$ | 223.2(10) | 2.21(22) | E2 |
| 838 | $GS-b4$ | $\rightarrow$ | $GS-b3$ | $21/2^-$ | $\rightarrow$ | $19/2^+$ | 131.7(10) | 20.7(13) | E1 |
| 838 | $GS-b4$ | $\rightarrow$ | $b8$ | $21/2^-$ | $\rightarrow$ | $19/2^{(-)}$ | 216.5(10) | 1.11(11) | M1 |
| 838 | $GS-b4$ | $\rightarrow$ | $GS-b4$ | $21/2^-$ | $\rightarrow$ | $17/2^-$ | 290.9(10) | 7.4(5) | E2 |
| 1180 | $GS-b4$ | $\rightarrow$ | $GS-b3$ | $25/2^-$ | $\rightarrow$ | $23/2^+$ | 157.4(10) | 14.8(15) | E1 |
| 1180 | $GS-b4$ | $\rightarrow$ | $GS-b4$ | $25/2^-$ | $\rightarrow$ | $21/2^-$ | 341.4(10) | 2.6(3) | E2 |
| 1558 | $GS-b4$ | $\rightarrow$ | $GS-b3$ | $29/2^-$ | $\rightarrow$ | $27/2^+$ | 187.3(10) | 6.6(7) | E1 |
| 1558 | $GS-b4$ | $\rightarrow$ | $GS-b4$ | $29/2^-$ | $\rightarrow$ | $25/2^-$ | 378.9(10) | 1.8(3) | E2 |
| 1970 | $GS-b4$ | $\rightarrow$ | $GS-b3$ | $33/2^-$ | $\rightarrow$ | $31/2^+$ | 212.6(10) | 1.48(15) | E1 |
| 1970 | $GS-b4$ | $\rightarrow$ | $GS-b4$ | $33/2^-$ | $\rightarrow$ | $29/2^-$ | 411.5(10) | 1.48(11) | E2 |
| 2415 | $GS-b4$ | $\rightarrow$ | $GS-b3$ | $37/2^-$ | $\rightarrow$ | $35/2^+$ | 241.0(10) | 0.37(4) | E1 |
| 470 | $b8$ | $\rightarrow$ | $GS-b4$ | $15/2^{(-)}$ | $\rightarrow$ | $13/2^-$ | 146.6(10) | 10.0(7) | M1 |
| 622 | $b8$ | $\rightarrow$ | $b8$ | $19/2^{(-)}$ | $\rightarrow$ | $15/2^{(-)}$ | 152.0(5) | 1.48(15) | E2 |
| 886 | $b8$ | $\rightarrow$ | $b8$ | $23/2^{(-)}$ | $\rightarrow$ | $19/2^{(-)}$ | 264.5(5) | 1.11(11) | E2 |
| 466 | $b5-a$ | $\rightarrow$ | $GS-b1$ | $15/2^+$ | $\rightarrow$ | $13/2^+$ | 146.6(5) | 5.5(6) | M1 |
| 744 | $b5-a$ | $\rightarrow$ | $b5-b$ | $19/2^+$ | $\rightarrow$ | $17/2^-$ | 90.0(10) | 5.5(7) | E1 |

| | | | | | | | | | |
|---|---|---|---|---|---|---|---|---|---|
| 744 | $b5-a$ | $\rightarrow$ | $GS-b1$ | $19/2^{+}$ | $\rightarrow$ | $17/2^{+}$ | 173.9(5) | 5.2(3) | M1 |
| 1212 | $b5-a$ | $\rightarrow$ | $GS-b1$ | $23/2^{+}$ | $\rightarrow$ | $21/2^{+}$ | 353.8(10) | 11.1(11) | M1 |
| 1543 | $b5-a$ | $\rightarrow$ | $GS-b1$ | $27/2^{+}$ | $\rightarrow$ | $25/2^{+}$ | 358.5(10) | 4.4(4) | M1 |
| 1917 | $b5-a$ | $\rightarrow$ | $GS-b1$ | $31/2^{+}$ | $\rightarrow$ | $29/2^{+}$ | 366.1(10) | 0.6(3) | M1 |
| 2324 | $b5-a$ | $\rightarrow$ | $b5-a$ | $(35/2^{+})$ | $\rightarrow$ | $31/2^{+}$ | 406.6(10) | 2.03(18) | E2 |
| 654 | $b5-b$ | $\rightarrow$ | $b5-a$ | $17/2^{-}$ | $\rightarrow$ | $15/2^{+}$ | 187.4(10) | 11.1(11) | E1 |
| 964 | $b5-b$ | $\rightarrow$ | $b5-a$ | $21/2^{-}$ | $\rightarrow$ | $19/2^{+}$ | 220.0(10) | 2.21(22) | E1 |
| 1512 | $b5-b$ | $\rightarrow$ | $b5-a$ | $25/2^{-}$ | $\rightarrow$ | $23/2^{+}$ | 300.8(10) | 3.7(4) | E1 |
| 1840 | $b5-b$ | $\rightarrow$ | $b5-a$ | $29/2^{-}$ | $\rightarrow$ | $27/2^{+}$ | 297.0(10) | 3.0(3) | E1 |
| 2187 | $b5-b$ | $\rightarrow$ | $b5-a$ | $33/2^{-}$ | $\rightarrow$ | $31/2^{+}$ | 270.1(10) | 0.6(4) | E1 |
| 932 | $b7-a$ | $\rightarrow$ | $GS-b1$ | $19/2^{(+)}$ | $\rightarrow$ | $17/2^{+}$ | 362.5(10) | 5.2(3) | M1 |
| 1171 | $b7-b$ | $\rightarrow$ | $b7-a$ | $21/2^{(-)}$ | $\rightarrow$ | $19/2^{(+)}$ | 238.8(10) | 1.85(18) | E1 |
| 1281 | $b7-c$ | $\rightarrow$ | $b7-a$ | $21/2^{(-)}$ | $\rightarrow$ | $19/2^{(+)}$ | 348.4(10) | 1.85(18) | E1 |
| 413 | $b6-a$ | $\rightarrow$ | $GS-b1$ | $7/2^{(-)}$ | $\rightarrow$ | $5/2^{+}$ | 413.3(10) | 37(4) | E1 |
| 550 | $b6-b$ | $\rightarrow$ | $b6-a$ | $9/2^{(+)}$ | $\rightarrow$ | $7/2^{(-)}$ | 136.2(10) | 1.48(15) | E1 |
| 747 | $b6-b$ | $\rightarrow$ | $b6-b$ | $13/2^{(+)}$ | $\rightarrow$ | $9/2^{(+)}$ | 197.8(10) | 0.74(7) | E2 |
| 1002 | $b6-c$ | $\rightarrow$ | $b6-b$ | $11/2^{(-)}$ | $\rightarrow$ | $13/2^{(+)}$ | 255.0(10) | 1.11(18) | E1 |
| 1741 | $b9-a$ | $\rightarrow$ | $GS-b4$ | $31/2^{(-)}$ | $\rightarrow$ | $29/2^{-}$ | 182.3(10) | 3.7(4) | M1 |
| 1915 | $b9-b$ | $\rightarrow$ | $b9-a$ | $33/2^{(+)}$ | $\rightarrow$ | $31/2^{(-)}$ | 174.3(5) | 2.6(3) | E1 |
| 1948 | $5b-c$ | $\rightarrow$ | $b5-a$ | $(29/2^{-})$ | $\rightarrow$ | $27/2^{+}$ | 404.8(5) | 3.69(15) | E1 |

# F. Condensation of rotational-aligned octupole phonons

The energy of a rigid core with inertia moment, $\Im$, rotational frequency, $\omega$, and an octupole vibration $\Omega_3$ is the sum of the rotational energy plus phonon excitation energy. The valance nucleons conform a set of particles which have a collective behavior and them, interact with the core as a whole:

$$E_n = \Omega_3\hbar(n+1/2) + \frac{\omega^2}{2}\Im$$

If the angular momentum of all phonons are alignment with the rotational axis, the system reaches its maximal angular momentum for a given energy $E_n$. Then, the angular momentum and the energy are:

$$I_n = ni + \omega\Im$$

$$E_n = \Omega_3\hbar(n+1/2) + \frac{(I_n - ni)^2}{2\Im}$$

In the frame rotating with the frequency $\omega$,

$$E'(\omega) = E_n - \omega I = \hbar\Omega_3(n+1/2) - ni\omega - \frac{\omega^2}{2}\Im$$

If one boson carries $i = 3\hbar$, the difference
$\omega(I^+) - \omega(I-1)^- = [I - ((I-1) - 3)]/\Im$ corresponds to a decrease of the angular momentum of the quadrupole rotor by $4\hbar$. The dipole moment is proportional to the product of the quadrupole moment $Q_2$ and the octupole moment $Q_3$. The transition is suppressed because $Q_2$ can only transfer $\pm 2\hbar$ to the rotor. The difference $\omega(I^-) - \omega(I-1)^+ = [I - 3 - (I-1))]/\Im$ corresponds to an increase of $2\hbar$, which can be transferred by $Q_2$ . The transitions $I^- \to (I-1)^+$ are allowed.

In the case of a static heart shape, the transitions $I^- \to (I-1)^+$ and
$I^+ \to (I-1)^-$ have equal probability. Here the difference frequency between the rotor and octupole phonon is reduced, the interaction is strong because the anharmonicities and the level repulsion increases [64].

# References


[1] F. Cristancho, J. Saladin, M. Metlay, W. Nazarewicz, C. Baktash, M. Halbert, I-Y. Lee, D. Winchell, S. Fischer, and M. Kabadiyski. High-spin studies of $^{219}$Ac. *Phys. Rev. C*, 49:663–671, Feb 1994.

[2] P. Butler and W. Nazarewicz. Intrinsic reflection asymmetry in atomic nuclei. *Rev. Mod. Phys.*, 68:349–421, Apr 1996.

[3] I-Yang Lee. The GAMMASPHERE. *Nuclear Physics A*, 520(0):c641 – c655, 1990. Nuclear Structure in the Nineties.

[4] W. Reviol, D.G. Sarantites, R.J. Charity, C.J. Chiara, J. Elson, M. Montero, O.L. Pechenaya, S.K. Ryu, and L.G. Sobotka. "hercules": Design, instrumentation, and performance characteristics of a high-efficiency evaporation-residue counter under a lot of elastic scattering for spectroscopic studies with gammasphere. *Nuclear Instruments and Methods in Physics Research Section A: Accelerators, Spectrometers, Detectors and Associated Equipment*, 541(3):478 – 500, 2005.

[5] G. J. Kumbartzki, N. Benczer-Koller, K.-H. Speidel, D. A. Torres, J. M. Allmond, P. Fallon, I. Abramovic, L. A. Bernstein, J. E. Bevins, H. L. Crawford, Z. E. Guevara, G. Gürdal, A. M. Hurst, L. Kirsch, T. A. Laplace, A. Lo, E. F. Matthews, I. Mayers, L. W. Phair, F. Ramirez, S. J. Q. Robinson, Y. Y. Sharon, and A. Wiens. $z = 50$ core stability in $^{110}$Sn from magnetic-moment and lifetime measurements. *Phys. Rev. C*, 93:044316, Apr 2016.

[6] N. Benczer-Koller, G. J. Kumbartzki, K.-H. Speidel, D. A. Torres, S. J. Q. Robinson, Y. Y. Sharon, J. M. Allmond, P. Fallon, I. Abramovic, L. A. Bernstein, J. E. Bevins, H. L. Crawford, Z. E. Guevara, A. M. Hurst, L. Kirsch, T. A. Laplace, A. Lo, E. F. Matthews, I. Mayers, L. W. Phair, F. Ramirez, and A. Wiens. Magnetic moment and

lifetime measurements of coulomb-excited states in $^{106}\mathrm{Cd}$. *Phys. Rev. C*, 94:034303, Sep 2016.

[7] G. Maquart, L. Augey, L. Chaix, I. Companis, C. Ducoin, J. Dudouet, D. Guinet, G. Lehaut, C. Mancuso, N. Redon, O. Stézowski, A. Vancraeyenest, A. Astier, F. Azaiez, S. Courtin, D. Curien, I. Deloncle, O. Dorvaux, G. Duchêne, B. Gall, T. Grahn, P. Greenlees, A. Herzan, K. Hauschild, U. Jakobsson, P. Jones, R. Julin, S. Juutinen, S. Ketelhut, M. Leino, A. Lopez-Martens, P. Nieminen, P. Petkov, P. Peura, M.-G. Porquet, P. Rahkila, S. Rinta-Antila, M. Rousseau, P. Ruotsalainen, M. Sandzelius, J. Sarén, C. Scholey, J. Sorri, S. Stolze, and J. Uusitalo. Backbending in the pear-shaped $^{223}_{90}\mathrm{Th}$ nucleus: Evidence of a high-spin octupole to quadrupole shape transition in the actinides. *Phys. Rev. C*, 95:034304, Mar 2017.

[8] R. V. F. Reviol, Janssens, S. Frauendorf, D. G. Sarantites, M. P. Carpenter, X. Chen, C. J. Chiara, D. J. Hartley, K. Hauschild, T. Lauritsen, A. Lopez-Martens, M. Montero, D. Seweryniak O. L. Pechenaya, J. B. Snyder, and S. Zhu. Characterization of octupole-type strctures in $^{221}\mathrm{Th}$. *Physical Review C*, 90:044318, October 2014.

[9] I. Ahmad and P.A. Butler. Octupole shapes in nuclei. *Annual Review of Nuclear and Particle Science*, 43:71–116, December 1993.

[10] R. Casten. *Nuclear Structure from a Simple Perspective*. Oxford, 2000.

[11] G. Seaborg W. Loveland, D. J. Morrisey. *Modern Nuclear Chemistry*. Ed. John Wiley&Sons Inc, 2006.

[12] P.E. Hodgson&E. Gadioli. *Introductory Nuclear Physics*. Oxford, 1997.

[13] Kris L. G. Heyde. *Basics Ideas and Concepts in Nuclear Physics*. Institute of Physics Publishing, Bristol and Philadelphia, Dirac House, Temple Back, Bristol BS1 6BE, UK, 1999.

[14] Maria Goeppert Mayer. Nuclear configurations in the spin-orbit coupling model. i. empirical evidence. *Phys. Rev.*, 78:16–21, Apr 1950.

[15] Otto Haxel, J. Hans D. Jensen, and Hans E. Suess. On the "magic numbers" in nuclear structure. *Phys. Rev.*, 75:1766–1766, Jun 1949.

[16] William D. Myers and Wladyslaw J. Swiatecki. Nuclear masses and deformations. *Nuclear Physics*, 81(1):1 – 60, 1966.

[17] Sven Gosta Nillson and Ingemar Ragnarsson. *Shapes and Shells in Nuclear Structure*. Cambridge University Press, The Edinburgh Building, Cambridge CB2 2RU, UK, 1995.

[18] S. Frauendorf. Symmetries in nuclear strcture. *Nuclear Physics A*, 752:203c–212c, 2005.

[19] Richard B Firestone. *Table of isotopes. vol. 1, A*. John Wiley, 1996.

[20] S. Frauendorf. Spontaneous symmetry breaking in rotating nuclei. *Reviews of Modern Physics*, 73:463–514, April 2001.

[21] M. Dahlinger, E. Kankeleit, D. Habs, D. Schwalm, B. Schwartz, R.S. Simon, J.D. Burrows, and P.A. Butler. Alternating parity bands and octupole effects in $^{221}\mathrm{Th}$ and $^{223}\mathrm{Th}$. *Nuclear Physics A*, 484(2):337 – 375, 1988.

[22] G. Leander and Y. Chen. Reflection-asymmetric rotor model of odd a$\sim$219˘229 nuclei. *Phys. Rev. C*, 37:2744–2778, Jun 1988.

[23] S. Ćwiok and W. Nazarewicz. Reflection-asymmetric shapes in odd-a actinide nuclei. *Nuclear Physics A*, 529(1):95 – 114, 1991.

[24] M. S. Nadirbekov, G. A. Yuldasheva, and V. Yu. Denisov. Alternating-parity collective states of yrast and nonyrast bands in lanthanide and actinide nuclei. *Physics of Atomic Nuclei*, 78(2):215–219, 2015.

[25] A. Bohr and B.R. Mottelson. Rotational states in even-even nuclei [13]. *Physical Review*, 90(4):717–719, 1953. cited By 30.

[26] D.R. Inglis. Particle derivation of nuclear rotation properties associated with a surface wave. *Physical Review*, 96:1059, November 1954.

[27] P A Butler. Octupole collectivity in nuclei. *Journal of Physics G: Nuclear and Particle Physics*, 43(7):073002, 2016.

[28] T H Hoare, P A Butler, G D Jones, M Loiselet, O Naviliat-Cuncic, J Vervier, M Dahlinger, A M Y El-Lawindy, R Wadsworth, and D L Watson. A study of $^{223}$th levels populated by alpha -decay. *Journal of Physics G: Nuclear and Particle Physics*, 17(2):145, 1991.

[29] R. K. Sheline. Character of the low-lying $0^-$ and $0^+$ states in the even rn, ra, th, u, and pu isotopes. *Phys. Rev. C*, 21:1660–1663, Apr 1980.

[30] W. Reviol, D. G. Sarantites, C. J. Chiara, M. Montero, R. V. F. Janssens, M. P. Carpenter, T. L. Khoo, T. Lauritsen, C. J. Lister, D. Seweryniak, S. Zhu, O. L. Pechenaya, and S. G. Frauendorf. Parity doubling in $^{219}\mathrm{Th}$ and the onset of collectivity above $\mathrm{N} = 126$. *Phys. Rev. C*, 80:011304, Jul 2009.

[31] J.R. Hughes, R. Tölle, J. De Boer, P.A. Butler, C. Günther, V. Grafen, N. Gollwitzer, V.E. Holliday, G.D. Jones, C. Lauterbach, M. Marten-Tölle, S.M. Mullins, R.J. Poynter, R.S. Simon, N. Singh, R.J. Tanner, R. Wadsworth, D.L. Watson, and C.A. White. Octupole correlations in $^{225}\mathrm{Th}$. *Nuclear Physics A*, 512(2):275 – 293, 1990.

[32] F. Asaro, F. Stephens, Jr., and I. Periman. Complex alpha spectra of radiothorium (th228) and thorium-x (ra224). *Physical Review*, 92:1495, December 1953.

[33] F. Asaro, F. Stephens, Jr., and I. Periman. Low-lying 1—states in even-even nuclei. *Physical Review*, 96:1568, December 1954.

[34] F. Asaro, F. Stephens, Jr., and I. Periman. Radiations from 1—states in even-even nuclei. *Physical Review*, 100:1543, December 1955.

[35] V. M. Strutinsky. Strutinsky. *At. Energ., 4*, page 150, 1956.

[36] D. R. Inglis. Particle Derivation of Nuclear Rotation Properties Associated with a Surface Wave. *Phys. Rev.*, 96:1059–1065, 1954.

[37] S. Frauendorf, Y. Gu, and J. Sun. Tidal waves a non-adiabatic microscopic description of the yrast states in near-spherical nuclei. *International Journal of Modern Physics E*, 20:465–473, September 2011.

[38] S. Zhu, R.V.F. Janssens, G.J. Laneb, I. Wiedenhöver, M.P. Carpenter, I. Ahmad, A.P. Byrne, P. Chowdhury, D. Clinef, A.N. Deacon, G.D. Dracoulis, S.J. Freeman, N.J. Hammond, G.D. Jones, T.L. Khoo, F.G. Kondev, T. Lauritsen, C.J. Lister, A.O. Macchiavelli, D. Seweryniak E.F. Moorea, J.F. Smith, and C.Y. Wuf. Strength of octupole correlations in the actinides: contrasting behavior in the isotones $^{237}$u and $^{239}$pu. *Physics Letters B*, 618:51–59, May 2005.

[39] W. Reviol, C. J. Chiara, M. Montero, D. G. Sarantites, O. L. Pechenaya, M. P. Carpenter, R. V. F. Janssens, T. L. Khoo, T. Lauritsen, C. J. Lister, D. Seweryniak, S. Zhu, and S. G. Frauendorf. Multiple octupole-type band structures in $^{220}\mathrm{Th}$: Reflection-asymmetric tidal waves? *Phys. Rev. C*, 74:044305, Oct 2006.

[40] R. V. Jolos and P. von Brentano. Rotational spectra and parity splitting in nuclei with strong octupole correlations. *Nuclear Physics A*, 587:377–389, May 1995.

[41] R.R. Chasman. Incipient octupole deformation and parity doublets in the odd mass light actinides. *Physics Letters B*, 96:7–10, October 1980.

[42] R.R. Chasman and I. Ahmad. Triaxiality and reflection asymmetry in the mass region a $\sim$220. *Physics Letters B*, 182:261–264, December 1986.

[43] R.R. Chasman. Odd-multipole correlations in the light actinides. *Physics Letters B*, 219:232–236, March 1989.

[44] L.M. Robledo, J.L. Egido, B. Nerlo-Pomorska, and K. Pomorski. A quantum parity-conserving study on octupole deformation in the light-actinide region. *Physics Letters B*, 201:409–414, February 1988.

[45] P. Bonche, S. J. Krieger, M. S. Weiss, J. Dobaczewski, H. Flocard, and P.-H. Heenen. Octupole softness of superdeformed $^{194}$pb. *Phys. Rev. Lett.*, 66:876, February 1991.

[46] W. Nazarewicz, P. Olanders, I. Ragnarsson, J. Dudek, and G. A. Leander. High-spin consequences of octupole shape in nuclei around $^{22}\mathrm{Th}$. *Phy.Rev.Lett*, 53:1272, April 1994.

[47] W. Nazarewicz and S. L. Tabor. Octupole shapes and shape changes at high spins in the z$\sim$58, n$\sim$88 nuclei. *Physical Review C*, 45:2226, May 1992.

[48] G. Duchêne, F.A. Beck, P.J. Twin, G. de France, D. Curien, L. Han, C.W. Beausang, M.A. Bentley, P.J. Nolan, and J. Simpson. The clover: a new generation of composite ge detectors. *Nuclear Instruments and Methods in Physics Research Section A: Accelerators, Spectrometers, Detectors and Associated Equipment*, 432(1):90 – 110, 1999.

[49] M. Saha Sarkar, Ritesh Kshetri, Rajarshi Raut, A. Mukherjee, Mandira Sinha, Maitreyi Ray, A. Goswami, Subinit Roy, P. Basu, H. Majumder, S. Bhattacharya, and B. Dasmahapatra. Characterisation of a compton suppressed clover detector for high energy gamma rays ($\leq$11mev). *Nuclear Instruments and Methods in Physics Research Section A: Accelerators, Spectrometers, Detectors and Associated Equipment*, 556(1):266 – 272, 2006.

## REFERENCES


[50] N Benczer-Koller., M Hass., , and J Sak. Transient magnetic fields at swift ions traversing ferromagnetic media and application to measurements of nuclear moments. *Annual Review of Nuclear and Particle Science*, 30(1):53–84, 1980.

[51] G.J. Kumbartzki. Transition from collectivity to single-particle degrees of freedom from magnetic moment measurements on $^{82}_{38}\mathrm{Sr}_{44}$ and $^{90}_{38}\mathrm{Sr}_{52}$. *Phys. Rev. C*, 89:064305, Jun 2014.

[52] G.J. Kumbartzki et al. Structure of the Sr-Zr isotopes near and at the magic $N = 50$ shell from $g$-factor and lifetime measurements in $^{88}_{40}$Zr and $^{84,86,88}_{38}$Sr. *Phys. Rev. C*, 85:044322, Apr 2012.

[53] J. Leske, K.-H. Speidel, S. Schielke, O. Kenn, J. Gerber, P. Maier-Komor, S. J. Q. Robinson, A. Escuderos, Y. Y. Sharon, and L. Zamick. Nuclear structure of the first $2+$ state in radioactive $^{68}$Ge based on g factor and lifetime measurements. *Phys. Rev. C*, 71(4):044316, Apr 2005.

[54] K.-H. Speidel et al. Experimental g factors and B(E2) values in Ar isotopes: Crossing the N=20 semi-magic divide. *Physics Letters B*, 632(2-3):207 – 211, 2006.

[55] D.A. Torres and F. Ramirez. Nuclear structure aspects via g-factor measurements: pushing the frontiers. *PoS Proceedings of Science, 10th Latin American Symposium on Nuclear Physics and Applications (2013)*, 2013.

[56] D.A. Torres et al. First $g$-factor measurements of the $2^+_1$ and the $4^+_1$ states of radioactive $^{100}$Pd. *Phys. Rev. C*, 84:044327, Oct 2011.

[57] D.A. Torres et al. Measurement of the $^{96}$Ru $g(4^+_1)$ factor and its nuclear structure interpretation. *Phys. Rev. C*, 85:017305, Jan 2012.

[58] Rainer M Lieder. *New generation of gamma-detector arrays*. Experimental Techniques in Nuclear Physics, Walter de Gruyter, Berlin, 1997.

[59] F. Cappellaro, J. Ljungvall, and J. Nyberg. Laboratory exercise in nuclear physics. studies of excited nuclear states in $^{166}$er using the $\gamma-\gamma$ coincidence technique. *Spring*, Frebruary 2012.

[60] E. BROWNEE and J. K. TULI. Adopted levels, gammas for $^{220}$ra, 2011.

[61] SUKHJEET SINGH and BALRAJ SINGH. Adopted levels, gammas for $^{224}$th, 2015.

[62] E. BROWNE. Adopted levels, gammas for $^{223}$th, 2001.

[63] S. Cwiok and W. Nazarewicz. Reflection-asymmetric shapes in odd-a actinide nuclei. *Nuclear Physics A*, 529(1):95 – 114, 1991.

[64] S. Frauendorf. Heart-shaped nuclei: Condensation of rotational-aligned octupole phonons. *Phys. Rev. C*, 77:021304, Feb 2008.

[65] W. Reviol, D.G. Sarantites, X. Chen, M. Montero, O.L. Pechenaya, J. Snyder, R.V.F. Janssens, M.P. Carpenter, C.J. Chiara, T.L. Khoo, T. Lauritsen, C.J. Lister, D. Seweryniak, S. Zhu, K. Hauschild, A. Lopez-Martens, D.J. Hartley, and S. Frauendorf. Tidal waves and onset of collectivity above $n = 126$. *Acta Physica Polonica B*, 42, 2011.